

Doctorate Dissertation

博士論文

Experimental and theoretical studies toward stronger
molecular orientation with an all-optical technique

(全光学的手法による気体分子の配向度向上を目指した実験的及び理論的研究)

A Dissertation Submitted for Degree of Doctor of Philosophy

December 2018

平成 30 年 12 月博士 (理学) 申請

Department of Physics, Graduate School of Science

The University of Tokyo

東京大学大学院理学系研究科物理学専攻

Md. Maruf Hossain

ホサイン・モハンマド マルフ

Abstract

A sample of aligned or oriented gaseous molecules can be used as an ideal quantum mechanical system for investigating the anisotropic dependence in many light-molecule interactions. For example, by orienting molecules to a specific direction, it is possible to control the stereodynamics of chemical reactions and selectively produce the desired product. High-harmonics generated from a sample of aligned or oriented molecules can be analyzed to probe the instantaneous structure of sample molecules. On the other hand, electromagnetic field intensity dependence of the degree of alignment or orientation can be used to estimate the anisotropies of polarizability and hyperpolarizability of sample molecules experimentally. Due to these multifaceted and compelling prospects, controlling the rotational motion of asymmetric molecules is an active area of research.

We can realize molecular alignment or orientation by utilizing the nonlinear interaction of asymmetric molecules with an intense nonresonant laser field. However, a single wavelength laser pulse can only realize molecular alignment because the interaction potential is symmetric upon the inversion of the laser electric field vector. For achieving molecular orientation, one needs to induce asymmetry in the interaction potential along the polarization axis. This asymmetric potential can be created either by introducing a weak electrostatic field or by using a phase-controlled two-color laser field. In the first approach, the permanent dipole interaction with an electrostatic field is enhanced by the anisotropic polarizability interaction with the intense nonresonant laser field. However, the presence of a weak electrostatic field may induce Stark effect in the rotationally controlled sample of asymmetric molecules, limiting their usefulness for various applications. Moreover, the orientation direction is limited by the arrangement of the electrodes used to generate the electrostatic field.

In contrast, laser fields can be rapidly turned off by using the plasma-shutter technique, and the orientation direction can be arbitrarily controlled by changing the polarization direction of the two-color laser field and the relative phase difference between the two wavelengths. Hence, all-optical molecular orientation utilizing both anisotropic polarizability and hyperpolarizability interactions with an intense nonresonant two-color laser field is the way toward the realization of completely

field-free molecular orientation. However, since the second harmonic is generated by passing the intense fundamental pulse through a second-harmonic generation crystal, the rising part of the second harmonic pulse in a two-color laser field always follows the fundamental pulse. As a result, a deep symmetric potential due to polarizability interaction is created before the relatively weak asymmetric orientation potential can be formed, resulting in an enhanced degree of alignment, but a suppressed degree of orientation. Furthermore, since the orientation directions for states with even and odd quantum number J 's are opposite, the average degree of orientation of a thermal ensemble becomes weak. Despite these challenges, the proof-of-principle experiment performed in our laboratory has confirmed the validity of the all-optical method of molecular orientation using a two-color laser field. The goal of this research is to experimentally and theoretically investigate different ways of further increasing the degree of molecular orientation with an all-optical method.

To realize stronger molecular orientation with two-color laser fields, we have adjusted the relative delay between the two wavelengths by introducing a Michelson-type delay line in the optical path. By delaying the fundamental pulse in this way, we effectively allow the asymmetric potential to be created at the same time when the dominant symmetric potential due to polarizability interaction is formed. We have also used a home-build molecular deflector to select lower-lying rotational states of OCS molecules as a sample and avoid the weakening of the average degree of orientation due to opposite contributions from even and odd numbered states. By applying the fundamental pulse and its second harmonic pulse from an injection-seeded Nd:YAG laser as the two-color laser field, we have observed stronger degrees of molecular orientation: $\langle\langle\cos\theta\rangle\rangle \sim \pm 0.3$. The observed degree of orientation is an order of magnitude stronger than the degree of orientation obtained in the proof-of-principle experiment. It is also the strongest molecular orientation with an all-optical method, which was observed appropriately with the Coulomb explosion imaging by keeping the probe polarization perpendicular to the detection plane.

Although the applied laser pulse (FWHM ~ 12 ns) is orders of magnitude longer than the free rotational period of the sample molecule (82.24 ps), we theoretically and experimentally prove that all-optical molecular orientation dynamics is still nonadiabatic. Due to the nonadiabaticity, merely increasing the laser intensity will not necessarily improve the degree of orientation. Since the polarizability interaction usually is orders of magnitude larger than the hyperpolarizability interaction, the asymmetry in the potential may increase by increasing the laser intensity. However, at the same time, symmetric potential due to polarizability interaction will get deeper faster, making the tunneling to a deeper potential well more difficult. Here we propose a new all-optical molecular orientation approach which combines a linearly polarized fundamental pulse and an elliptically polarized second harmonic pulse to suppress the symmetric effect created by the polarizability interaction

while accelerating the tunneling to a deeper potential well, leading to the efficient creation of molecular orientation. By solving the time-dependent Schrödinger equation numerically, we show that it is possible to increase the degree of orientation by tuning the peak intensity along the minor axis of the elliptically polarized second harmonic laser pulse. This approach is especially useful for general molecules with smaller hyperpolarizability anisotropy and larger polarizability anisotropy. Finally, numerical results are presented to prove that the same combination of linearly and elliptically polarized two-color laser field is capable of realizing three-dimensional molecular orientation, which corresponds to an all-optical method of controlling all the spatial directions of an asymmetric top molecule.

Acknowledgments

I am indebted to Professor Hirofumi Sakai for guiding me through my life as a graduate student and encouraging me to pursue this research from both experimental and theoretical perspectives. His expertise in the field of controlling the rotational dynamics of molecular systems has enabled me to assimilate knowledge quickly and focus on the key issues. Most of the experimental techniques applied in this research were patiently taught by Dr. Shinichirou Minemoto. I am indeed grateful to him. I have developed the numerical scheme applied in this research upon discussion with Professor Miyashita Seiji, who was my co-supervisor under the Leading Graduate Course for Frontiers of Mathematical Sciences and Physics (FMSP).

Xiang Zhang has assisted me to run most of the crucial experiments discussed in this dissertation. He also helped me with the Monte Carlo simulation of the deflected gas beam profile. I am also thankful to Dr. Yuan-Pin Chang, Dr. Daniel Horke and Professor Jochen Küpper regarding this simulation. Ryohei Yamada has also helped me with the experiments in the later part of this research. I had the opportunity to discuss several issues regarding the numerical simulation and experimental techniques with Dr. Jehoi Mun and learned important insights from him. During the earlier days of this research, I had the opportunity to work with UTRIP students Holly Herbert, Niccolò Bigagli, and Asmae Benhemou. From time to time, I have discussed various issues related to my research with Wataru Komatsubara, Kazma Komatsu, and Soichiro Miyake of our laboratory. Finally, I would like to thank the Leading Graduate Course for Frontiers of Mathematical Sciences and Physics (FMSP) for supporting me financially.

Contents

1	Introduction	7
1.1	Definition of alignment and orientation	7
1.2	Gaseous crystal platform	8
1.3	Theoretical and experimental studies of all-optical molecular orientation	10
1.4	Outline of the thesis	13
2	Theory of molecular orientation with two-color laser fields	15
2.1	Definition of coordinate systems	15
2.2	Nonlinear interaction of molecules with laser fields	17
2.2.1	General asymmetric top molecules	18
2.2.2	linear asymmetric molecules	19
2.3	Adiabatic regime	21
2.4	Nonadiabatic regime	24
2.5	Tunneling in nonadiabatic molecular orientation dynamics	26
2.6	Numerical solution of TDSE describing molecular orientation	30
2.6.1	Higher-order Runge-Kutta method	30
2.6.2	Operator splitting method	31
2.6.3	Time evolution with the field-dressed Hamiltonian eigenstates	32
2.6.4	Higher-order Crank-Nicolson method	32
2.6.5	Implementation of higher-order Crank-Nicolson method	33
3	Experimental observation of stronger molecular orientation	37
3.1	Overview of the experiment	37
3.1.1	Even-Lavie valve	38
3.1.2	Supersonic expansion of sample molecules	38
3.1.3	Velocity map imaging	39
3.1.4	Time-of-flight	40
3.1.5	Molecular deflector	42
3.2	Optical setup	44
3.2.1	Michelson-type delay line	46
3.2.2	Real-time measurement of the relative phase difference	47
3.2.3	Fused silica plate to control the relative phase difference between the two wavelengths	48

3.3	Observation of stronger orientation	49
3.3.1	Nonadiabaticity in molecular orientation dynamics	53
4	All-optical molecular orientation with combined linearly and elliptically polarized two-color laser fields	61
4.1	Definition of the laser field	61
4.2	Interaction potential	62
4.3	Increasing the degree of orientation	65
4.4	Intensity dependence	67
4.5	The role of nonadiabaticity	70
4.6	Three-dimensional molecular orientation	71
4.6.1	Nonlinear interaction through polarizability and hyperpolarizability anisotropies	71
4.6.2	Estimation of the degree of orientation	72
5	Conclusion	75
5.1	Summary of results	75
5.1.1	Observation of stronger all-optical molecular orientation . . .	75
5.1.2	Experimental evidence of nonadiabaticity in all-optical molecular orientation	76
5.1.3	All-optical molecular orientation with combined linearly polarized and elliptically polarized two-color laser fields	76
5.2	Future research challenges	76
A	Appendices	79
A.1	Free rotational period of linear molecules	79
A.2	Tunneling in a double-well potential	80
A.2.1	Symmetric double-well potential	80
A.2.2	Asymmetric double-well potential	82
A.3	Expressing interaction Hamiltonian terms with spherical harmonics .	83
A.4	Electric field strength of a Gaussian beam	84
A.5	Unit conversion table for molecular polarizability and hyperpolarizability	86
	Bibliography	87

List of Figures

1.1	Random, aligned and oriented molecular ensemble.	8
1.2	Outline of the experimental system for constructing a Gaseous Crystal Platform	9
2.1	Definition of space-fixed and the molecular body-fixed coordinate systems.	16
2.2	Euler angles ϕ , θ and χ relates the space-fixed and the body-fixed frames.	17
2.3	(a) Interaction potential of a OCS molecule under a linearly polarized two-color laser field, (b) The enlarged asymmetric part of the potential responsible for orientation.	20
2.4	$\langle\langle \cos^2 \theta \rangle\rangle$ and $\langle\langle \cos \theta \rangle\rangle$ of OCS molecules as a function of the peak intensity of the fundamental pulse, I_ω . The peak intensity of the second harmonic, $I_{2\omega} = 1.1I_\omega$	23
2.5	$\langle\langle \cos^2 \theta \rangle\rangle$ and $\langle\langle \cos \theta \rangle\rangle$ of FCN molecules as a function of the peak intensity of the fundamental pulse, I_ω . The peak intensity of the second harmonic, $I_{2\omega} = 1.1I_\omega$	23
2.6	Spatial probability density profile of the first two instantaneous eigenfunctions ($(\tilde{J}, \tilde{M}) = (0, 0)$ and $(\tilde{J}, \tilde{M}) = (1, 0)$) at the peak of the laser intensity for (a) a symmetric potential of eq. (2.40) and (b) an asymmetric potential of eq. (2.42). Blue and red colors are used for domains where $0 \leq \theta < \frac{\pi}{2}$ and $-\frac{\pi}{2} \leq \theta < 0$, respectively.	27
2.7	Characteristic time for tunneling (black curve) in a double well potential when an asymmetric potential of Eq. (2.41) is created by an electrostatic field. The red dashed curve denotes τ_{sym} , which is calculated from Eq. (A.11) by using the symmetric double-well model for the symmetric part of the potential of Eq. (A.14). The blue dashed line denotes τ_{asym} , which is derived from Eq. (A.15) by finding the shift in energy ΔV_0 from the electrostatic term μE_S	28

2.8	Characteristic time for tunneling (black curve) in a double well potential when an asymmetric potential of Eq. (2.42) is created by an all-optical method. The red dashed curve denotes τ_{sym} , which is calculated from Eq. (A.11) by using the symmetric double-well model for the symmetric part of the potential of Eq. (2.42). The blue dashed line denotes τ_{asym} , which is derived from Eq. (A.15) by considering only the asymmetric part of the total potential given by Eq. (2.42).	28
2.9	Boltzmann weights for initial states	30
2.10	$\langle\langle\cos^2\theta\rangle\rangle$ and $\langle\langle\cos\theta\rangle\rangle$ of OCS molecule as a function of time. The peak intensities are, $I_\omega = 7.2 \times 10^{11}$ W/cm ² and $I_{2\omega} = 3.5 \times 10^{11}$ W/cm ² . The HWHM of the fundamental pulse and the second harmonics are 6.32 ns and 4.65 ns, respectively. The fundamental wave is delayed by 1.75 ns with respect to the second harmonic which has its peak at 0 ns.	34
2.11	$\langle\langle\cos^2\theta\rangle\rangle$ and $\langle\langle\cos\theta\rangle\rangle$ of FCN molecule as a function of time. The peak intensities are, $I_\omega = 7.2 \times 10^{11}$ W/cm ² and $I_{2\omega} = 3.5 \times 10^{11}$ W/cm ² . The HWHM of the fundamental pulse and the second harmonics are 6.32 ns and 4.65 ns, respectively. The fundamental wave is delayed by 1.75 ns with respect to the second harmonic which has its peak at 0 ns.	34
3.1	Overview of the experiment for observing molecular orientation	38
3.2	Time-of-flight spectrum observed for identifying fragment ions. . . .	40
3.3	Covariance mapping of ion population at different times of flight. . . .	41
3.4	Stark energies W (left panel) and effective dipole moments μ_{eff} (right panel) for different states $ JM\rangle$ of an OCS molecule. These energy curves are calculated using the Python package “CMIstark” [206]. . .	43
3.5	Distribution of the electric field generated between the deflector electrodes.	43
3.6	Vertical profiles of OCS molecular beams.	43
3.7	simulated deflected profile of OCS molecular beam.	44
3.8	Optical setup	45
3.9	Adjusting the rising parts of the two wavelengths with a Michelson-type delay line.	46
3.10	Interference intensity (red dots) corresponding to the relative phase difference Φ as a function of time. The black line is the low pass filtered signal.	47
3.11	Derivation of the relation between $\Delta\Phi$ and the angle of the fused silica plate.	48
3.12	Distribution of the observed degree of orientation.	50
3.13	The mean squared error (MSE) between the fitted Gaussian distribution and the histogram of $\langle\langle\cos\theta\rangle\rangle$ is plotted after removing several points from the upper and lower tails of the histogram. The horizontal axis shows the number of points that are removed.	51

3.14	Observation of strong upward and downward orientation. The S^+ fragment ions are used in this observation.	52
3.15	Degrees of alignment and orientation for OCS molecules as a function of the fundamental pulse intensity (adiabatic approximation). The second harmonic pulse peak intensity is $I_{2\omega} = 3.5 \times 10^{11}$ W/cm ²	54
3.16	Degrees of alignment and orientation for OCS molecules as a function of the fundamental pulse intensity (TDSE). The second harmonic pulse peak intensity is $I_{2\omega} = 3.5 \times 10^{11}$ W/cm ²	54
3.17	Observed molecular alignment with S^+ fragment ion produced from OCS molecules as a function of the fundamental pulse intensity. The second harmonic pulse peak intensity is $I_{2\omega} = 3.5 \times 10^{11}$ W/cm ²	55
3.18	Observed molecular orientation with S^+ fragment ion produced from OCS molecules as a function of the fundamental pulse intensity. The second harmonic pulse peak intensity is $I_{2\omega} = 3.5 \times 10^{11}$ W/cm ²	55
3.19	Observed molecular alignment with CO^+ fragment ion produced from OCS molecules as a function of the fundamental pulse intensity. The second harmonic pulse peak intensity is $I_{2\omega} = 3.5 \times 10^{11}$ W/cm ²	56
3.20	Observed molecular orientation with CO^+ fragment ion produced from OCS molecules as a function of the fundamental pulse intensity. The second harmonic pulse peak intensity is $I_{2\omega} = 3.5 \times 10^{11}$ W/cm ²	56
3.21	Time profile of the characteristic time for tunneling τ_{tun} for fundamental pulses with different peak intensities. The intensity of the second harmonic pulse is 3.5×10^{11} W/cm ²	57
3.22	Temporal evolution of the field-free eigenstate $ J, M\rangle = 0, 0\rangle$ under laser field. The spatial probability density profile of the wave function is plotted for both the adiabatic and the nonadiabatic processes. Blue and red colors are used for domains where $0 \leq \theta < \frac{\pi}{2}$ and $-\frac{\pi}{2} \leq \theta < 0$, respectively.	58
4.1	Interaction potential as a function of θ and ϕ when a combined linearly and elliptically polarized two-color laser field defined by Eq. (4.1) is used to orient OCS molecules. The asymmetry between the two minima along the θ axis is exaggerated.	64
4.2	Interaction potential as a function of θ and ϕ when a conventional linearly polarized two-color laser field defined by Eq. (2.13) is used to orient OCS molecules. The asymmetry between the two minima along the θ axis is exaggerated.	64
4.3	Degrees of alignment $\langle\langle \cos^2 \theta \rangle\rangle$ and orientation $\langle\langle \cos \theta \rangle\rangle$ as a function of time for an all-optical method with a linearly polarized two-color laser field.	66

4.4	Degrees of alignment $\langle\langle\cos^2\theta\rangle\rangle$ and orientation $\langle\langle\cos\theta\rangle\rangle$ as a function of time for an all-optical method with a combined linearly and elliptically polarized two-color laser field. The peak intensities are $I_\omega = 3.6 \times 10^{11}$ W/cm ² , $I_{2\omega} = 3.9 \times 10^{11}$ W/cm ² , and $I'_{2\omega} = 3.5 \times 10^{11}$ W/cm ²	66
4.5	Degrees of alignment $\langle\langle\cos^2\theta\rangle\rangle$ (dots) and orientation $\langle\langle\cos\theta\rangle\rangle$ (crosses) as a function of the peak laser intensity. The panels in the left column is for OCS molecules and those in the right column represents the results for FCN molecules. Blue color is used to denote the case of a linearly polarized two-color laser field, whereas red is used to denote an all-optical technique with a combined linearly and elliptically polarized laser field.	68
4.6	Degrees of alignment $\langle\langle\cos^2\theta\rangle\rangle$ (dots) and orientation $\langle\langle\cos\theta\rangle\rangle$ (crosses) of OCS molecules as a function of the peak laser intensity where the horizontal component $I'_{2\omega}$ of the elliptically polarized second harmonic pulse is (a) lower or (b) higher than that of figure 4.5a. The initial rotational temperature is $T_{\text{rot}} = 0.6$ K.	68
4.7	Degrees of alignment $\langle\langle\cos^2\theta\rangle\rangle$ (dots) and orientation $\langle\langle\cos\theta\rangle\rangle$ (crosses) of OCS molecules as a function of peak laser intensity when the initial rotational temperatures are (a) $T_{\text{rot}} = 0.6$ K and (b) $T_{\text{rot}} = 2$ K. The results are computed under the assumption of adiabatic approximation.	70
4.8	Degrees of alignment $\langle\langle\cos^2\theta\rangle\rangle$ of iodobenzene molecules as a function of the peak intensity of the fundamental pulse.	73
4.9	Degrees of orientation $\langle\langle\cos\theta\rangle\rangle$ of iodobenzene molecules as a function of the peak intensity of the fundamental pulse.	73
A.1	Tunneling in a double well potential: (a) impenetrable potential with infinite barrier, (b) symmetric potential with transition passage, (c) asymmetric potential with transition passage	81

List of Tables

2.1	Polarizability and hyperpolarizability parameters of OCS and FCN . .	21
2.2	Rotational constants and asymmetry in potentials for OCS and FCN .	21
3.1	Relative populations of individual quantum states in the deflected re- gion of the molecular beam profile.	44
3.2	Details of the laser pulses used in this experiment.	45
3.3	Comparison of experimentally observed degree of orientation $\langle\langle\cos\theta\rangle\rangle$.	52
4.1	Rotational constants, polarizability and hyperpolarizability components of an iodobenzene molecule.	74
A.1	Unit conversion table for molecular polarizability and hyper polariz- ability. Reproduced from [231]. [a.u.: atomic units, SI: international system units, esu: electrostatic units.]	86

Introduction

Generally, gaseous molecules are randomly oriented. To investigate various interesting phenomena originating from the anisotropy in molecular structure, we need to prepare a sample of aligned or oriented molecules.

Using samples of aligned and oriented molecules paves the way of observing the deformation in molecular orbitals on the timescale of chemical reactions, revealing the formation and breaking of chemical bonds [1–3]. For example, X-ray photoelectron diffraction (XPD) patterns from laser-aligned molecules have been used to detect molecular structure at femtosecond time scales [4–7]. High-harmonics generated from a sample of aligned or oriented molecules can also be observed together with the ion yields in the ionization process to create a tomographic reconstruction of the instantaneous structure of molecular systems [8–10]. The possibilities are not limited to observation only, we can realize coherent control of chemical reactions and ionization process by controlling the rotational dynamics of gaseous molecules with shaped laser pulses [11, 12].

Manipulation of the rotational dynamics of gaseous molecules with laser pulses has been a very active area of research. The polarizability anisotropy of gaseous molecules can be measured by evaluating the change in the degree of molecular alignment with respect to the laser pulse intensity and the initial rotational temperature [13]. On the other hand, alignment of surface-absorbed molecules with laser pulses can control electron transport through junctions, which may realize ultrafast nanoscale current switches [14]. Recently, an all-optical method for enantioselective orientation of gaseous chiral molecules by using laser pulses with twisted polarization has been proposed [15]. Such all-optical methods of manipulating molecular enantiomers in the gas phase with laser pulses may create novel experimental methods to investigate fundamental questions such as the selection of chiral enantiomers for molecules (amino acids and sugars) in early molecular networks [16]. Due to these compelling and diversified prospects, research outcomes pertaining to molecular alignment and orientation have indeed been getting ardent attention from a wide range of audiences.

1.1 Definition of alignment and orientation

As shown in figure 1.1, we want to trap the molecules along the z axis, which is normally defined by the electric field vector in the laboratory-fixed frame. The elec-

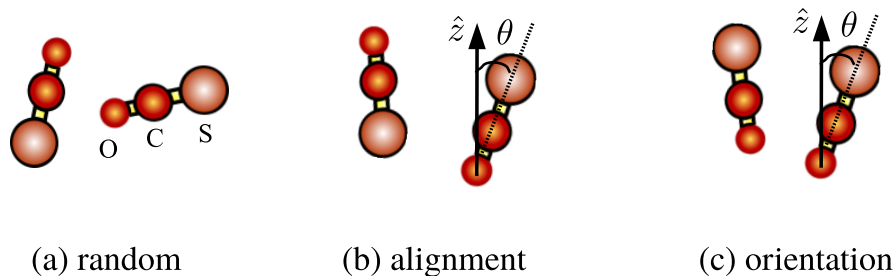


Fig. 1.1: Random, aligned and oriented molecular ensemble.

tronic field is generally the source of energy that is required to reduce the randomness in the rotational directions of the molecules. Alignment is explained with carbonyl sulfide (OCS) molecules in figure 1.1 (b), where the trapped molecules face both upward and downward. The angular distribution of the molecules is symmetric upon the inversion of the z axis. On the other hand, orientation is shown in figure 1.1 (c), where all the molecules (strictly speaking, more than half of the molecules) face upward. The angular distribution of the molecules is *not* symmetric upon the inversion of the z axis. To quantitatively estimate the degree of alignment or orientation, we measure the angle θ between the laboratory-fixed z axis and the rotational direction of sample molecules. Since the sample molecules are a so-called thermal ensemble, we use the statistical average value $\langle\langle \cos^2 \theta \rangle\rangle$ as a measure of the degree of alignment. On the other hand, the average quantity $\langle\langle \cos \theta \rangle\rangle$ is used to define the degree of molecular orientation.

1.2 Gaseous crystal platform

In gaseous molecules, the intermolecular distance is much longer than that in solid materials. As a result, the interaction potential with a neighbouring molecule is weaker compared to that in solid state crystals. This makes isolated gas phase molecules good candidates for approximating independent quantum mechanical systems. Moreover, a sample of asymmetric gaseous molecules, when oriented toward a single direction, can reveal various properties related to the anisotropy of the molecules. However, spectroscopic properties related to the asymmetry of the molecules are not revealed when the rotational directions of the molecules are random. When an average is taken, the isotropic distribution of randomly oriented asymmetric molecules cancels these properties. As a result, the formation of an oriented sample of gaseous molecules is useful in various applications to reveal the anisotropic properties. Experiments regarding the formation of a sample of aligned or oriented gas phase molecules can be regarded as “Gaseous Crystal Platform.”

Construction of Gaseous Crystal Platform

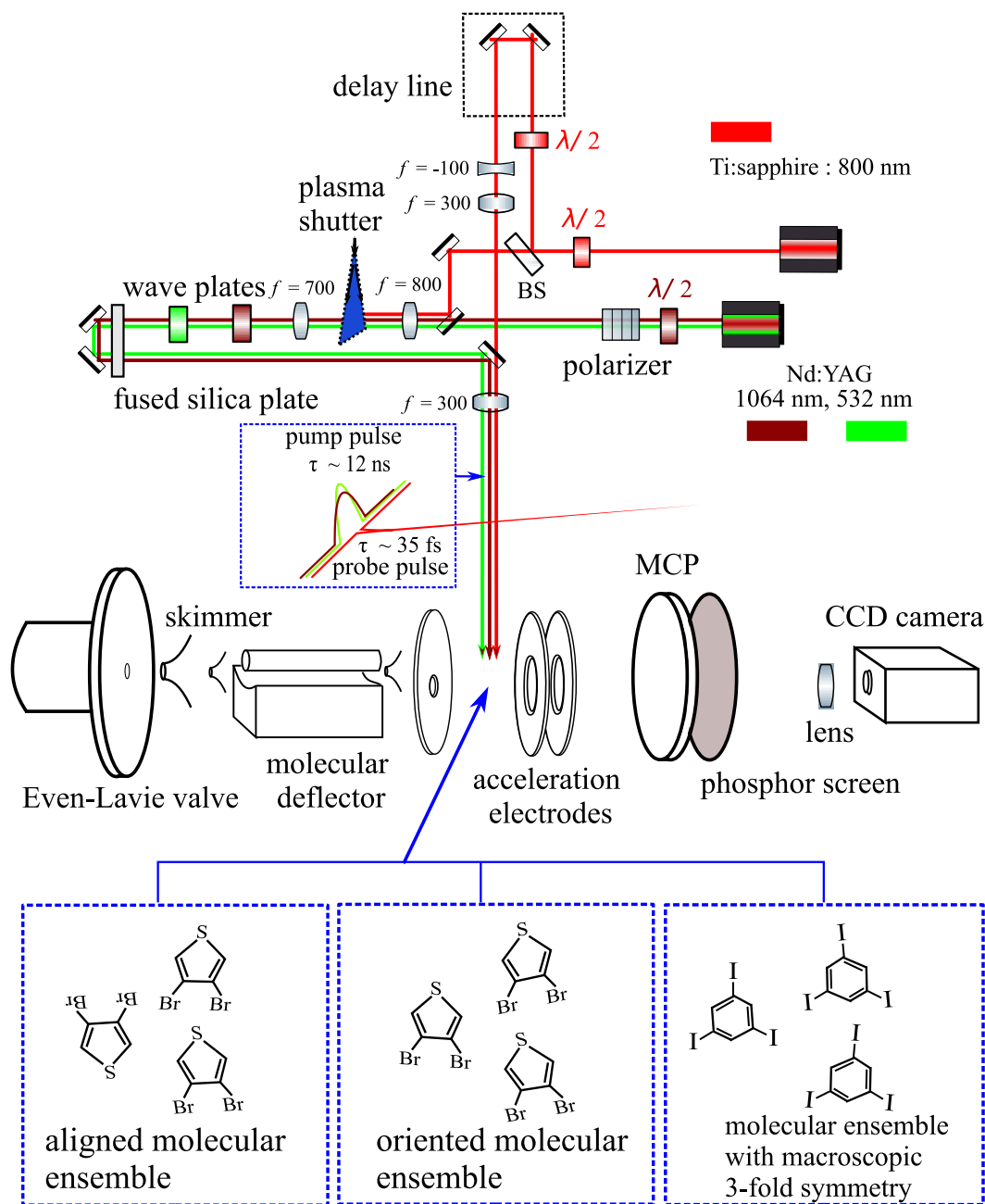


Fig. 1.2: Outline of the experimental system for constructing a Gaseous Crystal Platform

As presented in figure 1.2, the broader aim of our research is to create such an experimental platform.

1.3 Theoretical and experimental studies of all-optical molecular orientation

Molecular orientation can be achieved by applying a very strong electrostatic field where the asymmetric molecules interact with the applied electrostatic field through their dipole moment [17]. However, the required electric field is often too high for practical implementation and the Stark effect induced in the sample molecules limits their usefulness for subsequent experiments. On the contrary, as will be discussed in the following paragraphs, the application of intense nonresonant laser fields proved to be more useful and efficient in realizing molecular orientation.

There are two general categories of molecular orientation with laser pulses: the adiabatic regime and the nonadiabatic regime. In the adiabatic orientation, laser pulses much longer than the free rotational period of the sample asymmetric molecules are used. Typically, the FWHM of the laser pulse is on the order of a few nanoseconds and the rotational period is on the order of a few tens of picoseconds in these experiments. On the other hand, in nonadiabatic techniques, femtosecond laser pulses are adopted, and the pulse duration is much shorter than the free rotational period of the sample molecule.

In the nonadiabatic molecular orientation, a femtosecond laser pulse acts like an impulse which initiates the orientation dynamics by forming a rotational wave packet. Since the phase of the rotational wave packet changes over time and periodically interferes constructively, the degree of molecular orientation also revives periodically even after the application of the femtosecond laser pulse. The revival period is defined by the free rotational constant of the sample molecule [18, 19]. These repeated occurrences of molecular orientation are achieved under a completely field-free condition.

However, whether adiabatic or nonadiabatic, a single color laser field alone can never realize molecular orientation. The single color laser field only aligns the molecules because the interaction potential due to polarizability anisotropy is symmetric upon the inversion of the polarization axis of the applied laser field [20–25]. Nonadiabatic one-dimensional alignment with femtosecond laser pulses have been experimentally observed [22, 25–27]. Experiments confirming one-dimensional alignment in the adiabatic regime with an intense nonresonant nanosecond laser field have also been performed [23, 28]. Three-dimensional alignment with elliptically or circularly polarized laser fields has also been theoretically proposed and experimentally demonstrated [28–34].

One of the techniques of realizing molecular orientation with intense nonresonant laser fields is to introduce an additional weak electrostatic field to create an asym-

metric potential along the polarization axis of the laser field. The dipole moment interaction induced by a weak electrostatic field can be enhanced with a high-intensity laser field. The high-intensity laser field interacts with the polarizability anisotropy of sample molecules and enhances the the degree of orientation [25, 35–40]. Experimental studies confirming the molecular orientation with combined electrostatic and intense nonresonant laser fields have been successful [40–44]. Several theoretical studies regarding time-dependent dynamics of one-dimensional and three-dimensional molecular orientation using this method have been recently performed as well [45, 46]. Nevertheless, even though the electrostatic field is weak in this method, the problem of an existing electrostatic field interfering with further experimental procedures still exists. Furthermore, the direction of molecular orientation is defined by the electrostatic field vector. As a result, to change the direction of molecular orientation, one needs to rotate the electrodes that apply high voltages to create the electrostatic field.

Another technique of introducing an asymmetric potential along the polarization axis of an oscillating laser field is to use a phase-locked two-color laser field. Generally, the fundamental pulse and the second harmonic pulse of the pump laser are used as the two-color laser field [18, 47–51]. Since only the laser pulses are used for molecular orientation without the help of an electrostatic field, this method is labeled as the all-optical method. The direction of molecular orientation is completely controlled by the polarization axis of the two-color laser field and the relative phase difference between the two wavelengths.

However, the achievable degree of orientation with a two-color laser field is not so high [50–54]. The direction of molecular orientation with a two-color laser field is opposite for even and odd quantum number J 's. As a result, the averaged degree of orientation of a thermal ensemble does not increase efficiently.

To get around this issue, nonadiabatic molecular orientation with a preceding alignment pulse followed by a delay-adjusted two-color laser field has been proposed [55–57]. The alignment pulse first nonadiabatically aligns the molecules. The rotational wave packets with odd and even J 's exhibit opposite behavior around the half rotational periods. For example, rotational states with odd J 's align themselves along the laser polarization plane and rotational states with even J 's anti-align them toward a perpendicular direction. Although the total degree of alignment is reduced due to this opposite behavior, the relative population of odd and even rotational wave packets in the aligned molecules is manipulated. By carefully delaying a two-color laser field to fall on the half rotational periods, one can manipulate the relative excitation between the odd and even rotational wave-packet contributions and selectively enhance the averaged degree of molecular orientation. This technique has also been verified experimentally [58–60]. However, these techniques do not directly observe molecular orientation with a radially symmetric Coulomb explosion imaging

and Velocity Map spectroscopy, where the polarization direction is appropriately kept perpendicular to the detection plane [24, 61, 62]. Several other approaches of increasing the degree of orientation with femtosecond laser pulses have been actively proposed. For example, using a time-delayed THz pulse after the two-color femtosecond laser pulses [63, 64], adjusting the relative intensities of a three-color laser field [65], tuning the relative delay between the two pulses [66], using a few-cycle phase-jump pulses [67], changing the shape of the laser pulse to ramp, Gaussian or square functions [68], etc. A theoretical study on three-dimensional molecular orientation with two-color laser fields where the polarization axes of the fundamental pulse and the second harmonic pulse are crossed has been pursued [69], and an experimental demonstration of such a method has recently been reported [70].

In molecular orientation with nanosecond laser pulses, the laser intensity can be kept relatively moderate for a much longer period of time compared to the impulsive methods using femtosecond pulses. Since the laser pulse width is long enough compared to the free rotational period of the sample molecules, the technique is expected to adiabatically achieve higher degrees of alignment and orientation. However, the highest degrees of alignment and orientation is realized at the peak of the laser pulse and it gradually falls with the decrease in intensity after the peak. Hence, to realize completely field-free molecular orientation, we need to turn off the laser field within a few hundred femtoseconds. By using the plasma shutter technique, it is possible to turn the intense laser field off with a falling time of ~ 150 fs [71–75]. A femtosecond laser pulse is focused onto a $50\text{-}\mu\text{m}$ -thick ethylene glycol jet sheet with a peak intensity higher than the plasma formation threshold to turn off the nanosecond laser pulse at its peak intensity. After the rapid turn off, the degrees of alignment and orientation revive with a period of half rotational period and full rotational period of the sample molecule, respectively [76–79]. By using this technique, both one-dimensional and three-dimensional laser-field-free molecular orientation with the help of a weak electrostatic field have been achieved experimentally [72–75, 80]. Recently, spectrally truncated chirped laser pulses have been reported to produce similar laser pulses with a slow turn on and a rapid turn off [81].

All-optical Molecular orientation with a nonresonant two-color nanosecond laser field has been observed experimentally [50, 51], proving the validity of the scheme [48]. The current purpose of our research is to further increase the degree of orientation. One of the main problems regarding the all-optical molecular orientation with a two-color nanosecond laser field lies in the relative rising time of the fundamental pulse and the second harmonic. A recent theoretical study has shown that this effect can be optimized by adjusting the relative delay and the relative intensities of the two-color laser fields [82, 83]. The scope of this thesis is to further investigate these issues, both theoretically and experimentally, and to find out novel approaches for increasing the degree of molecular orientation with an all-optical technique.

1.4 Outline of the thesis

The purpose of this research is to theoretically and experimentally investigate novel methods for realizing stronger degrees of molecular orientation with an all-optical method. In an all-optical method, the degree of orientation does not improve even if we increase the laser intensity. Asymmetric molecules interact with the high-intensity laser field through their polarizability and hyperpolarizability anisotropies. The interaction due to polarizability anisotropy creates a symmetric potential upon the inversion of the polarization axis of the laser field. Hence, this potential is responsible for molecular alignment. The hyperpolarizability interaction introduces the asymmetry to the alignment potential, realizing molecular orientation. However, the symmetric alignment potential formed by the polarizability interaction is orders of magnitude deeper than the asymmetric potential created by the hyperpolarizability anisotropy. Moreover, the direction of orientation is opposite for states with odd and even J 's. Naturally, since the degree of orientation is an average of the even and odd numbered states for a thermal ensemble, the realized molecular orientation is weak. We have studied these phenomena and their solutions both theoretically and experimentally. In this thesis, we are going to discuss our findings on these issues in details.

In chapter 2 of this thesis, the general theory of molecular alignment and orientation is outlined. Although the fundamental theory of controlling the rotational dynamics of gas phase molecules is well-developed, implementing numerical simulations of molecular alignment and orientation dynamics is difficult. In this chapter, we have discussed various methods of numerically solving the time-dependent Schrödinger equation to simulate molecular orientation with nanosecond laser pulses. After pointing out the advantages and disadvantages of each method, we have finally opted for the higher-order Crank-Nicolson approach. The detailed derivation of the method is given and numerical results obtained by applying this method to simulate the degrees of alignment and orientation are demonstrated.

Chapter 3 is about experimental studies performed toward observing stronger molecular orientation with a two-color laser field. Since the second harmonic pulse of the two-color laser field is generated from the fundamental pulse, there is a delay between the rising parts of the two pulses. As a result, the symmetric alignment potential is formed before the second harmonic can introduce the asymmetry in the potential. Moreover, since the polarizability interaction is a few orders of magnitude stronger than the hyperpolarizability interaction, the relative delay between the fundamental pulse and the second harmonic pulse plays a crucial role. By introducing a Michelson-type delay line in the laser path, we have adjusted the relative delay between the two wavelengths. On the other hand, we have used a home-built molecular deflector to select rotationally cold sample molecules. By se-

lecting the lower-lying rotational states, we can alleviate the averaging out of the degree of orientation for states with even and odd J 's. These techniques allowed us to observe stronger degrees of molecular orientation with an all-optical method. Furthermore, we have shown in this chapter, both numerically and experimentally, that the degree of orientation is not a monotonically increasing function of the laser peak intensity, which proves that molecular orientation dynamics with two-color ~ 10 ns laser pulses is inherently nonadiabatic.

A novel all-optical approach to molecular orientation with combined linearly polarized and elliptically polarized laser fields has been proposed in chapter 4. In the case of linear asymmetric molecules, we show that an elliptically polarized second harmonic pulse can suppress the strong alignment potential while keeping the asymmetry in the total potential unperturbed. Through numerically solving the time-dependent Schrödinger equation, we have demonstrated that the degree of orientation improves substantially by this method compared to the approach where a linearly polarized two-color laser field is used.

Finally, in chapter 5, we have summarized the core insights obtained in this research about all-optical molecular orientation with a nonresonant two-color laser field. Some suggestions related to experimental and theoretical studies based on the understanding developed during this research are detailed to facilitate further advancements on this topic.

Theory of molecular orientation with two-color laser fields

In this chapter, the fundamental theory of molecular alignment and orientation is discussed. Although the theory itself is well documented, numerical implementation of the underlying dynamics is not. First, different frames of reference required to describe the dynamics are defined. Then, the nonlinear interaction of the molecules with a high-intensity laser field is described using the Schrödinger equation. Different algorithms for numerically solving the angular wave functions are introduced, discussing the advantages and disadvantages of each algorithm. Finally, higher-order Crank-Nicolson method is detailed and simulation results are discussed using this method.

2.1 Definition of coordinate systems

To describe the dynamics of molecular alignment and orientation, we use two coordinate systems. The space-fixed or the laboratory coordinate system is defined by the polarization and the propagation direction of the laser field. Another coordinate system is fixed to the body of the sample molecule. In figure 2.1 (a), the capital letters X, Y , and Z show the space-fixed frame. The body-fixed coordinates are shown as x, y , and z in figure 2.1 (c). The laser pulse is linearly polarized along the Z direction and propagating toward the $-Y$ direction. Euler angles ϕ , θ , and χ as defined in figure 2.2 are used to describe the rotations needed to coincide the space-fixed frame with the body-fixed frame [84, 85].

In our calculations, we use the following three rotations [85]:

1. A counterclockwise rotation ϕ about Z . The Y axis is carried to the line of nodes denoted by N . which is also labeled as y' :

$$\begin{bmatrix} x' \\ y' \\ z' \end{bmatrix} = \mathbf{R}_Z(\phi) \begin{bmatrix} X \\ Y \\ Z \end{bmatrix} = \begin{pmatrix} \cos \phi & \sin \phi & 0 \\ -\sin \phi & \cos \phi & 0 \\ 0 & 0 & 1 \end{pmatrix} \begin{bmatrix} X \\ Y \\ Z \end{bmatrix}. \quad (2.1)$$

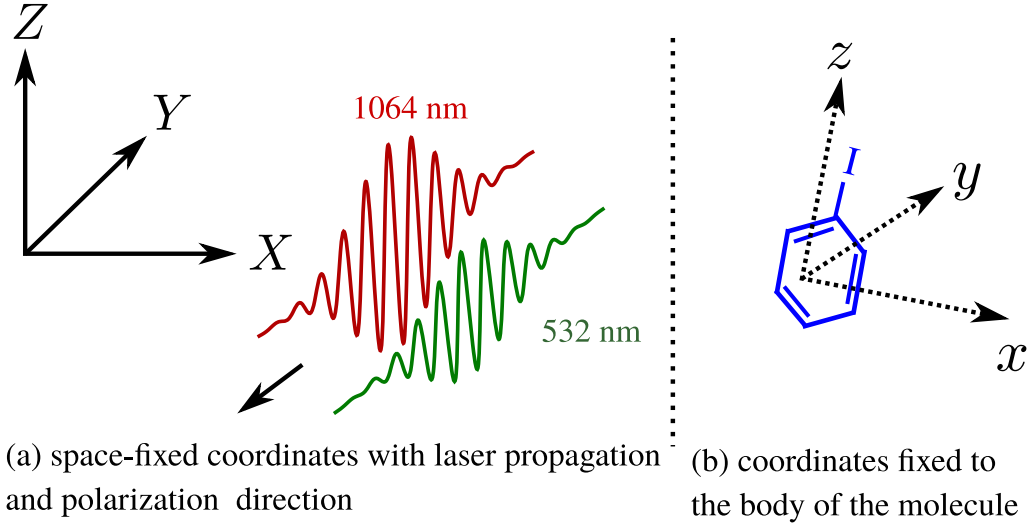


Fig. 2.1: Definition of space-fixed and the molecular body-fixed coordinate systems.

2. A counterclockwise rotation θ about the line of nodes N . The Z axis is now carried to the body-fixed $z'' = z$ axis:

$$\begin{bmatrix} x'' \\ y'' \\ z'' \end{bmatrix} = \mathbf{R}_{y'}(\theta) \begin{bmatrix} x' \\ y' \\ z' \end{bmatrix} = \begin{pmatrix} \cos \theta & 0 & -\sin \theta \\ 0 & 1 & 0 \\ \sin \theta & 0 & \cos \theta \end{pmatrix} \begin{bmatrix} x' \\ y' \\ z' \end{bmatrix}. \quad (2.2)$$

3. A counterclockwise rotation χ about $z'' = z$, the line of nodes y' is carried to the body-fixed y axis:

$$\begin{bmatrix} x \\ y \\ z \end{bmatrix} = \mathbf{R}_z(\chi) \begin{bmatrix} x'' \\ y'' \\ z'' \end{bmatrix} = \begin{pmatrix} \cos \chi & \sin \chi & 0 \\ -\sin \chi & \cos \chi & 0 \\ 0 & 0 & 1 \end{pmatrix} \begin{bmatrix} x'' \\ y'' \\ z'' \end{bmatrix}. \quad (2.3)$$

As a result, the total rotational matrix that transforms a quantity from the space-fixed frame to the body-fixed frame is given by,

$$\begin{aligned} \begin{bmatrix} x \\ y \\ z \end{bmatrix} &= R_z(\chi) R_{y'}(\theta) R_Z(\phi) \begin{bmatrix} X \\ Y \\ Z \end{bmatrix} \\ &= \begin{bmatrix} c\phi c\theta c\chi - s\phi s\chi & s\phi c\theta c\chi + c\phi s\chi & -s\theta c\chi \\ -c\phi c\theta s\chi - s\phi c\chi & -s\phi c\theta s\chi + c\phi c\chi & s\theta s\chi \\ c\phi s\theta & s\phi s\theta & c\theta \end{bmatrix} \begin{bmatrix} X \\ Y \\ Z \end{bmatrix}. \end{aligned} \quad (2.4)$$

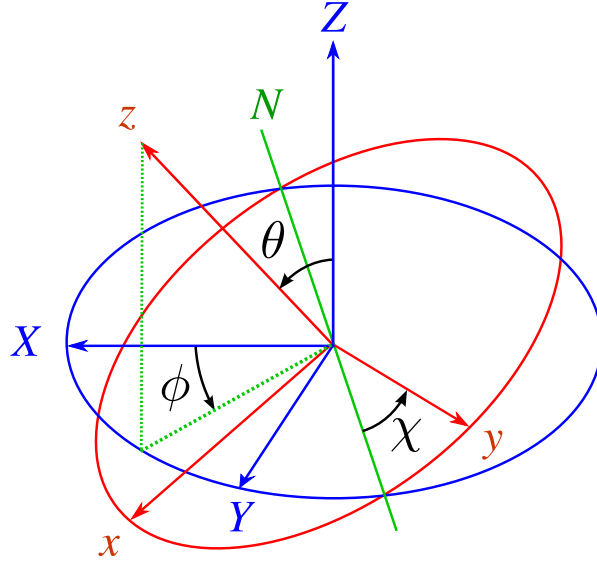


Fig. 2.2: Euler angles ϕ , θ and χ relates the space-fixed and the body-fixed frames.

Here, “c” is used to denote “cos” and “s” is used to denote “sin” in Eq. (2.4). We use Eq. (2.4) to transform the laser electric fields defined in the space-fixed frame to the body-fixed frame of the sample molecule. Molecular orientation means trapping the sample molecules along the polarization direction of the laser field. The angle between the space-fixed Z axis and the body-fixed z axis is given by θ . The average value of $\cos \theta$ is used to characterize the degree of orientation, and the average value of $\cos^2 \theta$ is used to characterize the degree of alignment.

2.2 Nonlinear interaction of molecules with laser fields

Since we are interested mainly in the rotational dynamics of molecules, we treat the molecules as rigid rotors. This is under the assumption that the molecules are not deformed under a high-intensity laser field. Moreover, the moment of inertia is assumed to be independent of the quantum numbers J, K , and M , because we have ignored the quantum mechanical effects of the centrifugal force. After diagonalizing the moment of inertia tensor \mathbf{I} , we get three principal moments of inertia I_a, I_b and I_c [85–87]. In this thesis, we will discuss two types of molecules:

1. Asymmetric top molecules
 - a) Principal moments of inertia: $I_a < I_b < I_c$.
 - b) Sample molecule: iodobenzene ($\text{C}_6\text{H}_5\text{I}$) [88, 89].

c) type of orientation: three-dimensional orientation.

2. linear molecules

a) Principal moments of inertia: $I_a = 0, I_b = I_c$.

b) Sample molecules: carbonyl sulfide (OCS) [76, 90, 91] and cyanogen fluoride (FCN) [77, 92].

c) type of orientation: one-dimensional orientation.

2.2.1 General asymmetric top molecules

The Hamiltonian for the free rotational motion of a general asymmetric top molecule is given by the following expression [85–87, 93, 94]:

$$\hat{H}_0 = A\hat{J}_a^2 + B\hat{J}_b^2 + C\hat{J}_c^2, \quad (2.5)$$

here, A, B and C are rotational constants, related to the principal moments of inertia:

$$A = \frac{\hbar}{4\pi I_a} [\text{Hz}], \quad B = \frac{\hbar}{4\pi I_b} [\text{Hz}], \quad C = \frac{\hbar}{4\pi I_c} [\text{Hz}]. \quad (2.6)$$

The interaction potential with the laser field is given by, [17, 20–23, 28–30, 32–37, 55, 56, 76, 77, 95–100],

$$\hat{H}_i = -\sum_i \mu_i E_i - \frac{1}{2!} \sum_{ij} \alpha_{ij} E_i E_j - \frac{1}{3!} \sum_{ijk} \beta_{ijk} E_i E_j E_k - \dots + \text{H.O.T.} \quad (2.7)$$

To estimate the degrees of alignment and orientation, we want to numerically solve the following Schrödinger equation [49, 82, 94, 101–107]:

$$i\hbar \frac{\partial}{\partial t} |\Psi(t)\rangle = (\hat{H}_0 + \hat{H}_i) |\Psi(t)\rangle. \quad (2.8)$$

The free rotational Hamiltonian \hat{H}_0 can be written with the squared angular momentum operator \mathbf{J}^2 in the following form [86, 100]:

$$\hat{H}_0 = \frac{B+C}{2} \mathbf{J}^2 + \left(A - \frac{B+C}{2} \right) \hat{J}_a^2 + \frac{B-C}{4} [(\hat{J}^+)^2 - (\hat{J}^-)^2], \quad (2.9)$$

here, $\hat{J}^\pm = \hat{J}_b \pm i\hat{J}_c$. To perform numerical simulations, $|\Psi(t)\rangle$ is expanded by a suitable system of basis functions. In our calculation, we use the symmetric top wave functions [85, 86]:

$$|JKM\rangle = \left[\frac{2J+1}{8\pi^2} \right]^{\frac{1}{2}} D_{MK}^{J*}(\phi, \theta, \chi), \quad (2.10)$$

where, $D_{MK}^{J*}(\phi, \theta, \chi)$ is the rotation matrix or the Wigner D-matrix. The Wigner D-matrix elements form a complete orthogonal basis functions for the Euler angles ϕ, θ , and χ [108–115].

2.2.2 linear asymmetric molecules

For linear molecules, $I_a = 0, I_b = I_c$ and $K = 0$ [94]. Hence, Eq. (2.9) reduces to the following field-free Hamiltonian:

$$\hat{H}_0 = B\mathbf{J}^2, \quad (2.11)$$

where, B is the rotational constant of the linear molecule. In this case, the wave function $|\Psi\rangle$ is expressed with spherical harmonics [85]:

$$|JM\rangle = Y_{JM}(\theta, \phi) = \left(\frac{2J+1}{4\pi}\right)^{\frac{1}{2}} D_{M0}^{J*}(\phi, \theta, \chi). \quad (2.12)$$

The spherical harmonics form a complete orthonormal basis set of functions for the angles θ and ϕ [113, 116–119]. Eq. (2.12) can be derived from Eq. (2.10) considering the fact that a linear rigid rotor belongs to the point group $C_{\infty v}$ or $D_{\infty v}$ [94, 115], making the values of the angle χ indistinguishable. Hence, $K = 0$. The integration with respect to χ becomes redundant, corresponding to the extra 2π term in Eq. (2.10).

The interaction potential in Eq. (2.7) depends on the definition of the laser electric field. The traditional method of orientating asymmetric molecules with a two-color laser field contains the following electric field:

$$\begin{bmatrix} E_X(t) \\ E_Y(t) \\ E_Z(t) \end{bmatrix} = \begin{bmatrix} 0 \\ 0 \\ E_\omega(t) \cos \omega t + E_{2\omega}(t) \cos(2\omega t + \Phi) \end{bmatrix}, \quad (2.13)$$

here, the envelopes $E_\omega(t)$ and $E_{2\omega}(t)$ are defined as Gaussian pulses:

$$E_\omega(t) = E_\omega e^{-\frac{(t-\Delta t)^2}{2\tau_\omega^2}}, \quad E_{2\omega}(t) = E_{2\omega} e^{-\frac{t^2}{2\tau_{2\omega}^2}}, \quad (2.14)$$

where ω and 2ω are the angular frequencies, τ_ω and $\tau_{2\omega}$ are the widths of the Gaussian envelopes, E_ω and $E_{2\omega}$ are the peak electric field strengths, and Δt is the delay between the peaks of the fundamental pulse and the second harmonic pulse of the laser electric field. The relative phase difference Φ between the two waves is of particular interest here. Note that the pulse widths τ_ω and $\tau_{2\omega}$ are not the same as the pulse width τ (FWHM) as described in Eq. (A.30), because, according to

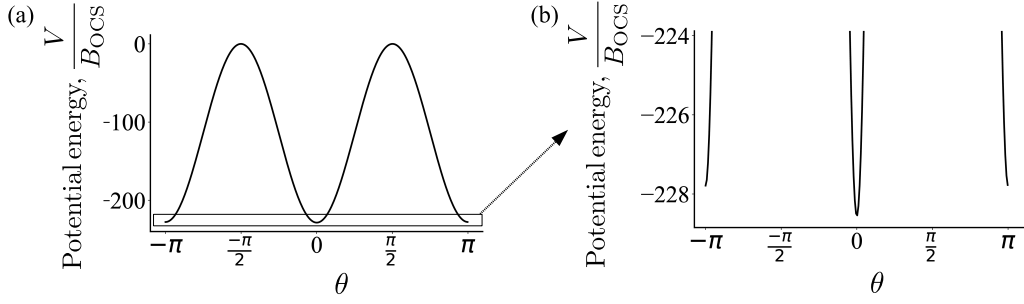


Fig. 2.3: (a) Interaction potential of a OCS molecule under a linearly polarized two-color laser field, (b) The enlarged asymmetric part of the potential responsible for orientation.

Eq. (A.33), the electric field strength E and the intensity I of a laser field have the relation $E \propto \sqrt{I}$. Generally, when we refer to the pulse width, we mean the FWHM of the intensity profile as given by Eq. (A.30).

We assume that the laser frequencies are far removed from any molecular resonance and much higher than τ_ω^{-1} , $\tau_{2\omega}^{-1}$, and the inverse of free rotational period of the sample molecule. As a result, the interaction Hamiltonian \hat{H}_i is averaged over the rapid oscillations of ω and 2ω [38, 49, 97, 120–122]. After taking the average over $\frac{2\pi}{\omega}$, the total Hamiltonian for a linear asymmetric molecule reduces to the following equation [18, 48, 49, 55, 56, 98, 122, 123]:

$$\begin{aligned} \hat{H}(t) = & B\mathbf{J}^2 - \frac{1}{4} [(\alpha_{\parallel} - \alpha_{\perp}) \cos^2 \theta] (E_{\omega}^2(t) + E_{2\omega}^2(t)) \\ & - \frac{1}{8} ((\beta_{\parallel} - 3\beta_{\perp}) \cos^2 \theta + 3\beta_{\perp}) \cos \theta \cos \Phi E_{\omega}^2(t) E_{2\omega}(t), \end{aligned} \quad (2.15)$$

where α_{\parallel} , α_{\perp} and β_{\parallel} , β_{\perp} are the polarizability and hyperpolarizability components parallel and perpendicular to the molecular axis, respectively. For OCS molecules, the potential part in Eq. (2.15) is plotted in Fig.2.3 (a). The asymmetric part of the total potential is shown in Fig. 2.3 (b). The double-well potential is responsible for aligning the molecules by trapping them around $\theta = 0$ and $\theta = \pi$. The asymmetry in the potential at these two points is responsible for orientation. The direction of this asymmetry (the direction of orientation) is controlled by the relative phase difference Φ . This asymmetry in the potential is orders of magnitude smaller than the total potential, making it difficult to orient general molecules like OCS. On the other hand, some molecules such as FCN have larger hyperpolarizability anisotropy to the total potential ratio compared to that of ordinary molecules such as OCS, allowing higher degrees of orientation. Different parameters required to calculate the potential for OCS and FCN molecules are summarized in table 2.1 and 2.2 [76, 77, 90–92]. For calculating the potential in table 2.2, we have used the values $E_{\omega} \sim 23.3 \text{ MV/cm}$ and $E_{2\omega} \sim 16.2 \text{ MV/cm}$, corresponding to the laser peak intensities, $I_{\omega} = 7.2 \times 10^{11} \text{ W/cm}^2$ and $I_{2\omega} = 3.5 \times 10^{11} \text{ W/cm}^2$, respectively.

Tab. 2.1: Polarizability and hyperpolarizability parameters of OCS and FCN

Molecule	$\Delta\alpha$ [C ² m ² J ⁻¹]	$\Delta\beta = \beta_{\parallel} - 3\beta_{\perp}$ [C ³ m ³ J ⁻²]	β_{\perp} [C ³ m ³ J ⁻²]
OCS	4.56×10^{-40}	4.39×10^{-51}	-1.93×10^{-51}
FCN	1.58×10^{-40}	9.52×10^{-52}	1.06×10^{-52}

Tab. 2.2: Rotational constants and asymmetry in potentials for OCS and FCN

Molecule	Rotational constant B [J]	Rotational period τ_{rot} [ps]	Depth of potential $\min(\frac{V}{B})$	Asymmetry in potential $\frac{ V(\theta=\pi)-V(\theta=0) }{B}$
OCS	4.03×10^{-24}	82.24	-228.5	0.76
FCN	6.99×10^{-24}	47.38	-45.7	0.45

We can now numerically solve Eq. (2.8) to quantitatively estimate the degrees of alignment and orientation. There are two cases to consider when solving Eq. (2.8):

1. Adiabatic Regime: When the change in the laser intensity is very slow compared to the free rotational period τ_{rot} of the sample molecules, i.e., $\tau_{\text{rot}} \ll \tau_{\omega}, \tau_{2\omega}$.
2. Nonadiabatic Regime: When the laser pulse width is comparable to or shorter than the rotational period τ_{rot} of the sample molecules, i.e., $\tau_{\text{rot}} \gtrsim \tau_{\omega}, \tau_{2\omega}$.

2.3 Adiabatic regime

The adiabatic approximation is applicable when the interaction potential H_i slowly changes with time, which means that the laser pulse width τ is much greater than the free rotational period τ_{rot} of the sample molecule. If we have the initial Hamiltonian H_{init} and the final Hamiltonian H_{fin} , the adiabatic theory states that the n -th eigenstate of H_{init} will be carried to the n -th eigenstate of H_{fin} under the Schrödinger equation, provided that the change happens sufficiently slowly [101, 102, 124–129], so that the following condition is met [128–132]:

$$\frac{|\langle E_m(t) | \dot{H}(t) | E_n(t) \rangle|}{|E_m(t) - E_n(t)|^2} \ll 1, \quad m \neq n, \quad t \in [0, T], \quad (2.16)$$

where $E_m(t)$ and $|E_m(t)\rangle$ are the nondegenerate eigenvalues and eigenstates of $H(t)$ and T is the total evolution time. This argument requires that the rate of change

in the Hamiltonian $H(t)$ is small, i.e., $\dot{H}(t) \sim 0$. Since the laser pulse width $\tau \sim 12$ ns is much longer than the free rotational period $\tau_{\text{rot}} \sim 82.24$ ps of the sample molecule (OCS) in our experiment, we usually assume that the condition in Eq. (2.16) is met. Under this assumption, the instantaneous Hamiltonian of Eq. (2.15) is eigendecomposed:

$$\sum_{JM} \langle J'M' | \hat{H}(t) | JM \rangle \langle JM | E_n \rangle = E_n \langle J'M' | E_n \rangle, \quad (2.17)$$

where $|E_n\rangle$ is the instantaneous eigenvector of $\hat{H}(t)$ corresponding to the eigenvalue E_n at time t . We normalize the Schrödinger equation with the rotational constant B before numerically performing the eigendecomposition. The matrix values for the squared angular momentum operator \mathbf{J}^2 are given by the following relation:

$$\langle J'M' | \mathbf{J}^2 | JM \rangle = J(J+1) \delta_{JJ'} \delta_{MM'}. \quad (2.18)$$

Other terms of Eq. (2.15) such as $\cos \theta$, $\cos^2 \theta$, $\cos^3 \theta$, etc. are first expressed in terms of the spherical harmonics basis functions $Y_{J_0 M_0}$ (see appendix). The matrix elements are then calculated by using the Clebsch-Gordan coefficients [85, 133]:

$$\langle J'M' | Y_{J_0 M_0} | JM \rangle = \left[\frac{(2J+1)(2J_0+1)}{4\pi(2J'+1)} \right]^{\frac{1}{2}} \langle JM, J_0 M_0 | J'M' \rangle \langle J_0, J_0 0 | J' 0 \rangle. \quad (2.19)$$

We have used the “`sympy.physics.quantum.cg`” package in Python 3.6 to numerically compute the Clebsch-Gordan coefficients [134]. Depending on whether J and M are good quantum numbers or not under the interaction potential, the eigenvector $|E_n\rangle$ can be labeled with quantum numbers \tilde{J} and \tilde{M} :

$$|E_n\rangle = |\tilde{J}\tilde{M}\rangle = \sum_{JM} d_{\tilde{J}\tilde{M}, JM} |JM\rangle. \quad (2.20)$$

This labelling scheme means that $|\tilde{J}\tilde{M}\rangle \rightarrow |JM\rangle$ when the laser electric field magnitudes $E_\omega, E_{2\omega} \rightarrow 0$ [41, 99]. One way of implementing this labeling scheme is to identify the eigenstates with their eigenvalue ordering [135]. Another strategy is to gradually increase the laser electric field E_ω and $E_{2\omega}$ while keeping track of each quantum state $|\tilde{J}\tilde{M}\rangle$. We can achieve this by assigning the labels \tilde{J} and \tilde{M} to the state $|E_n\rangle$ for which the product $\langle \tilde{J}\tilde{M} | E_n \rangle$ is the most dominant. Here, $|E_n\rangle$ is the eigenstate at each step while we gradually increase the laser field strength.

The expectation values $\langle \cos \theta \rangle$ and $\langle \cos^2 \theta \rangle$ for the eigenstate $|E_n\rangle$ are calculated as follows:

$$\langle \cos^2 \theta \rangle_{\tilde{J}\tilde{M}} = \langle E_n | \cos^2 \theta | E_n \rangle = \sum_{J'M'} \sum_{JM} d_{\tilde{J}\tilde{M}, J'M'}^* d_{\tilde{J}\tilde{M}, JM} \langle J'M' | \cos^2 \theta | JM \rangle, \quad (2.21)$$

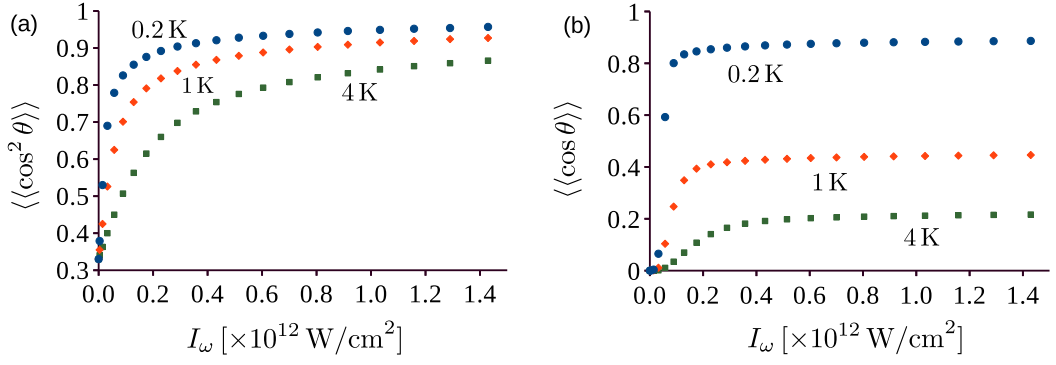


Fig. 2.4: $\langle\langle \cos^2 \theta \rangle\rangle$ and $\langle\langle \cos \theta \rangle\rangle$ of OCS molecules as a function of the peak intensity of the fundamental pulse, I_ω . The peak intensity of the second harmonic, $I_{2\omega} = 1.1I_\omega$.

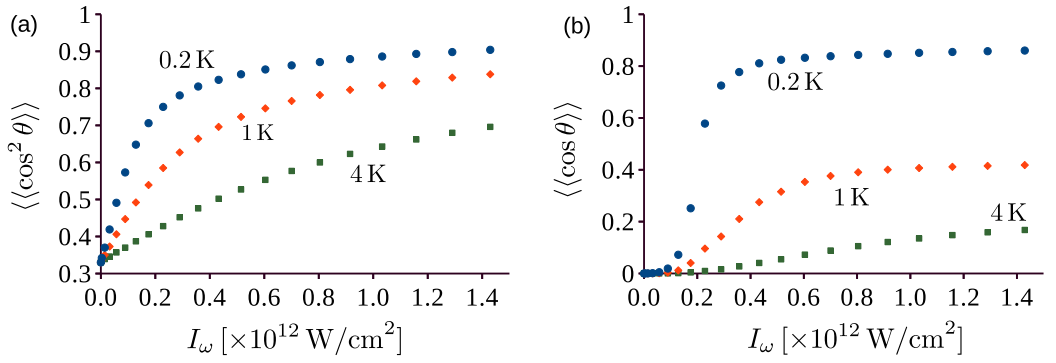


Fig. 2.5: $\langle\langle \cos^2 \theta \rangle\rangle$ and $\langle\langle \cos \theta \rangle\rangle$ of FCN molecules as a function of the peak intensity of the fundamental pulse, I_ω . The peak intensity of the second harmonic, $I_{2\omega} = 1.1I_\omega$.

and,

$$\langle \cos \theta \rangle_{\tilde{J}\tilde{M}} = \langle E_n | \cos \theta | E_n \rangle = \sum_{J'M'} \sum_{JM} d_{\tilde{J}\tilde{M}, J'M'}^* d_{\tilde{J}\tilde{M}, JM} \langle J'M' | \cos \theta | JM \rangle. \quad (2.22)$$

Finally, the ensemble averages of the expectation values for the degree of orientation and the degree of alignment are calculated assuming a Boltzmann distribution with the initial rotational temperature T_0 [48, 49, 71, 78, 79].

$$\langle\langle \cos^2 \theta \rangle\rangle = \sum_{\tilde{J}} w_{\tilde{J}} \sum_{\tilde{M}=-\tilde{J}}^{\tilde{M}=\tilde{J}} \langle \cos^2 \theta \rangle_{\tilde{J}\tilde{M}}, \quad (2.23)$$

$$\langle\langle \cos \theta \rangle\rangle = \sum_{\tilde{J}} w_{\tilde{J}} \sum_{\tilde{M}=-\tilde{J}}^{\tilde{M}=\tilde{J}} \langle \cos \theta \rangle_{\tilde{J}\tilde{M}}, \quad (2.24)$$

$$w_{\tilde{J}} = \frac{e^{-\frac{B\tilde{J}(\tilde{J}+1)}{k_B T_0}}}{\sum_{\tilde{J}} \tilde{J}(\tilde{J}+1) e^{-\frac{B\tilde{J}(\tilde{J}+1)}{k_B T_0}}}, \quad (2.25)$$

here, k_B is the Boltzmann constant. The estimated $\langle\langle\cos^2\theta\rangle\rangle$ and $\langle\langle\cos\theta\rangle\rangle$ of OCS molecules when $\Phi = \pi$ are shown in figure 2.4. We have used a linearly polarized two-color laser field as defined in Eq. (2.13). The horizontal axis shows the peak intensity of the fundamental laser pulse, I_ω . The peak intensity of the second harmonic is given by $I_{2\omega} = 1.1I_\omega$. Similar results for FCN molecules ($\Phi = 0$) are shown in figure 2.5. Comparing the figures 2.4 and 2.5, we see that the degree of molecular orientation depends sensitively to the initial rotational temperature T_0 of the sample molecules. Therefore, to achieve higher values of $\langle\langle\cos\theta\rangle\rangle$, it is required to decrease the initial rotational temperature as much as possible. On the other hand, both the degrees of alignment and orientation seem to be better for OCS molecules, for which the polarizability and hyperpolarizability parameters are higher than that of an FCN molecule. However, this happens as long as the adiabatic approximation is valid, which means that the laser pulse intensity changes very slowly. This requires the laser pulse width to be much longer than the free rotational period of the sample molecules. In reality, laser pulses are of finite width. In our experiment, the FWHM is around 12 ns. The relative asymmetry, which is defined as the ratio of the asymmetry in potential to the depth of the potential (table 2.2), plays an important role in determining the degrees of alignment and orientation in these cases. To fully understand this mechanism, we need to see the time evolution of the parameters $\langle\langle\cos^2\theta\rangle\rangle$ and $\langle\langle\cos\theta\rangle\rangle$ by solving the time-dependent version of the Schrödinger equation (Eq. (2.8)).

2.4 Nonadiabatic regime

In the nonadiabatic regime, the laser intensity changes fast compared to the free rotational period of molecules, i.e., $\tau_\omega, \tau_{2\omega} \sim \tau_{\text{rot}}$ or $\tau_\omega, \tau_{2\omega} \leq \tau_{\text{rot}}$. In these cases, we need to rigorously solve the following time-dependent Schrödinger equation:

$$i\hbar\frac{\partial}{\partial t}|\Psi(t)\rangle = \hat{H}(t)|\Psi(t)\rangle, \quad (2.26)$$

where the field-dressed Hamiltonian $\hat{H}(t)$ is given by Eq. (2.15). We can express any time dependent wave function by using spherical harmonics of Eq. (2.12) as basis functions and introducing time-dependent coefficients $d_{JM}(t)$,

$$|\Psi_{\tilde{J}\tilde{M}}(t)\rangle = \sum_{JM} d_{\tilde{J}\tilde{M},JM}(t)|JM\rangle. \quad (2.27)$$

The spherical harmonics are the eigenstates of the squared angular momentum operator \mathbf{J}^2 , and form a complete orthonormal basis set of functions for the angles θ and ϕ [85, 86, 113, 117–119]. The labels \tilde{J} and \tilde{M} are used to denote the initial pure state:

$$|\Psi_{\tilde{J}\tilde{M}}(t=0)\rangle = |\tilde{J}\tilde{M}\rangle. \quad (2.28)$$

Eq. (2.26) can be written as the following system of linear differential equations [22, 38, 77–79]:

$$\begin{aligned}
i \frac{\partial}{\partial t'} d_{\tilde{J}\tilde{M}, JM}^{\sim}(t') &= \sum_{J'M'} d_{\tilde{J}\tilde{M}, JM}^{\sim}(t') \langle JM | \mathbf{J}^2 | J'M' \rangle \\
&\quad - \frac{1}{4} \frac{\alpha_{\parallel} - \alpha_{\perp}}{B} (E_{\omega}^2(t') + E_{2\omega}^2(t')) \sum_{J'M'} d_{\tilde{J}\tilde{M}, JM}^{\sim}(t') \langle JM | \cos^2 \theta | J'M' \rangle \\
&\quad - \frac{1}{8} \frac{\beta_{\parallel} - 3\beta_{\perp}}{B} \cos \Phi E_{\omega}^2(t') E_{2\omega}(t') \sum_{J'M'} d_{\tilde{J}\tilde{M}, JM}^{\sim}(t') \langle JM | \cos^3 \theta | J'M' \rangle \\
&\quad - \frac{3}{8} \frac{\beta_{\perp}}{B} \cos \Phi E_{\omega}^2(t') E_{2\omega}(t') \sum_{J'M'} d_{\tilde{J}\tilde{M}, JM}^{\sim}(t') \langle JM | \cos \theta | J'M' \rangle,
\end{aligned} \tag{2.29}$$

where, t' is the rescaled time, $t' = \frac{Bt}{\hbar}$. the matrix element $\langle JM | \mathbf{J}^2 | J'M' \rangle$ is given by Eq. (2.18). Other matrix elements such as $\langle JM | \cos \theta | J'M' \rangle$, $\langle JM | \cos^2 \theta | J'M' \rangle$, and $\langle JM | \cos^3 \theta | J'M' \rangle$ are found from Eq. (2.19) and appendix A.3. Then, the expectation values $\langle \cos^2 \theta \rangle(t')$ and $\langle \cos \theta \rangle(t)$ for the initial pure state $|\tilde{J}\tilde{M}\rangle$ are calculated:

$$\langle \cos^2 \theta \rangle_{\tilde{J}\tilde{M}}^{\sim}(t) = \sum_{J'M'} \sum_{JM} d_{\tilde{J}\tilde{M}, J'M'}^* (t) d_{\tilde{J}\tilde{M}, JM}^{\sim}(t) \langle J'M' | \cos^2 \theta | JM \rangle, \tag{2.30}$$

$$\langle \cos \theta \rangle_{\tilde{J}\tilde{M}}^{\sim}(t) = \sum_{J'M'} \sum_{JM} d_{\tilde{J}\tilde{M}, J'M'}^* (t) d_{\tilde{J}\tilde{M}, JM}^{\sim}(t) \langle J'M' | \cos \theta | JM \rangle. \tag{2.31}$$

The initial molecular ensemble is not in a pure state, but in a mixed state. Hence, ensemble averages of the expectation values for the degree of orientation and the degree of alignment are calculated assuming a Boltzmann distribution with the initial rotational temperature T_0 [22, 56, 78, 79, 105]:

$$\langle \langle \cos^2 \theta \rangle \rangle(t) = \sum_{\tilde{J}} w_{\tilde{J}} \sum_{\tilde{M}=-\tilde{J}}^{\tilde{M}=\tilde{J}} \langle \cos^2 \theta \rangle_{\tilde{J}\tilde{M}}^{\sim}(t), \tag{2.32}$$

$$\langle \langle \cos \theta \rangle \rangle(t) = \sum_{\tilde{J}} w_{\tilde{J}} \sum_{\tilde{M}=-\tilde{J}}^{\tilde{M}=\tilde{J}} \langle \cos \theta \rangle_{\tilde{J}\tilde{M}}^{\sim}(t), \tag{2.33}$$

$$w_{\tilde{J}} = \frac{e^{-\frac{B\tilde{J}(\tilde{J}+1)}{k_B T_0}}}{\sum_{\tilde{J}} \tilde{J}(\tilde{J}+1) e^{-\frac{B\tilde{J}(\tilde{J}+1)}{k_B T_0}}}, \tag{2.34}$$

where k_B is the Boltzmann constant. Alternatively, we can define the initial mixed state using the following density matrix operator:

$$\hat{\rho}(t=0) = \sum_{\tilde{J}} \sum_{\tilde{M}=-\tilde{J}}^{\tilde{M}=\tilde{J}} w_{\tilde{J}\tilde{M}} |\tilde{J}\tilde{M}\rangle \langle \tilde{J}\tilde{M}|, \tag{2.35}$$

where,

$$w_{\tilde{J}\tilde{M}} = \frac{e^{-\frac{B\tilde{J}(\tilde{J}+1)}{k_B T_0}}}{\sum_{\tilde{J}\tilde{M}} e^{-\frac{B\tilde{J}(\tilde{J}+1)}{k_B T_0}}}. \quad (2.36)$$

The time evolution of the density matrix operator is described by the von Neumann equation [98, 105]:

$$i \frac{\partial \hat{\rho}(t)}{\partial t} = [\hat{H}(t), \hat{\rho}(t)]. \quad (2.37)$$

The time evolution of the degrees of alignment and orientation are described by the expectation values,

$$\langle \langle \cos^2 \theta \rangle \rangle (t) = \text{Tr} [\hat{\rho}(t) \cos^2 \theta], \quad (2.38)$$

$$\langle \langle \cos \theta \rangle \rangle (t) = \text{Tr} [\hat{\rho}(t) \cos \theta]. \quad (2.39)$$

2.5 Tunneling in nonadiabatic molecular orientation dynamics

The dynamics of molecular orientation with laser fields is a competition of the following two processes:

1. Alignment due to the symmetric double-well potential
2. Orientation induced by the asymmetric double-well potential

To explain the dynamics of molecular alignment and orientation, let us start from an alignment potential created by a single-color laser field [20, 22–24, 36]:

$$\hat{H}(t) = B\mathbf{J}^2 - \frac{1}{4}(\alpha_{\parallel} - \alpha_{\perp}) \cos^2 \theta E_{\omega}^2(t), \quad (2.40)$$

where, $E_{\omega}(t) = E_{\omega} e^{-\frac{t^2}{2\tau_{\omega}^2}}$ is the Gaussian profile of the fundamental pulse. Since the potential term is invariant under the parity operator $P : \theta \mapsto -\theta$, the dynamics, in this case, is explained by the symmetric well double well potential. The first two eigenstates, which are the symmetric and antisymmetric eigenstates of the parity operator P , are depicted in figure 2.6 (a). To induce orientation, we need to introduce an asymmetry in the double-well potential. To do this, we can either use an electrostatic field [35, 37, 38, 73, 75]:

$$\hat{H}(t) = B\mathbf{J}^2 - \mu E_S \cos \theta - \frac{1}{4}(\alpha_{\parallel} - \alpha_{\perp}) \cos^2 \theta E_{\omega}^2(t), \quad (2.41)$$

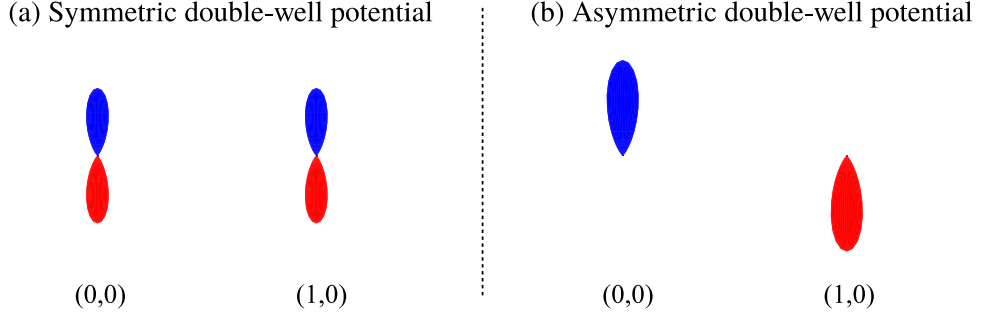


Fig. 2.6: Spatial probability density profile of the first two instantaneous eigenfunctions $((\tilde{J}, \tilde{M}) = (0, 0)$ and $((\tilde{J}, \tilde{M}) = (1, 0))$ at the peak of the laser intensity for (a) a symmetric potential of eq. (2.40) and (b) an asymmetric potential of eq. (2.42). Blue and red colors are used for domains where $0 \leq \theta < \frac{\pi}{2}$ and $-\frac{\pi}{2} \leq \theta < 0$, respectively.

where μ is the permanent dipole moment of the sample molecule and E_S is an electrostatic field along the laboratory-fixed z axis, or we can use the all-optical method with a two color laser field:

$$\hat{H}(t) = B\mathbf{J}^2 - \frac{1}{4} [(\alpha_{\parallel} - \alpha_{\perp}) \cos^2 \theta] (E_{\omega}^2(t) + E_{2\omega}^2(t)) \quad (2.42)$$

$$- \frac{1}{8} ((\beta_{\parallel} - 3\beta_{\perp}) \cos^2 \theta + 3\beta_{\perp}) \cos \theta \cos \Phi E_{\omega}^2(t) E_{2\omega}(t),$$

where, $E_{2\omega}(t) = E_{2\omega} e^{-\frac{t^2}{2\tau_{2\omega}^2}}$ is the Gaussian profile of the second harmonic pulse. The first two eigenstates in this case are shown in figure 2.6. Comparing with the symmetric potential of Eq. (2.40), we see that the wave functions in this case are localized in regions where either $0 \leq \theta < \frac{\pi}{2}$ ($((\tilde{J}, \tilde{M}) = (0, 0))$ or $-\frac{\pi}{2} \leq \theta < 0$ ($((\tilde{J}, \tilde{M}) = (1, 0))$). In adiabatic molecular orientation, the ground state and the first excited states of a free molecule slowly transform to the wave functions given in figure 2.6 (b). In nonadiabatic molecular orientation, the ground state and other eigenstates of the initial freely rotating molecule evolve to a linear combination of the instantaneous eigenstates of the field-dressed Hamiltonian. Since the field-dressed eigenstates orient themselves to opposite directions for even and odd numbered J 's, the achieved degree of orientation decreases in nonadiabatic molecular orientation compared to that of the adiabatic orientation.

We can understand why the nonadiabatic effects, where an initial eigenstate of the freely rotating molecule does not evolve to a single eigenstate of the field-dressed Hamiltonian, happen with a nanosecond laser pulse by considering the characteristic time for tunneling in a double-well potential. First, we numerically compute the first two eigenenergies E_1 and E_2 of the field-dressed Hamiltonian given by either Eq. (2.41) or Eq. (2.42) while slowly increasing the laser intensity. Then, we find

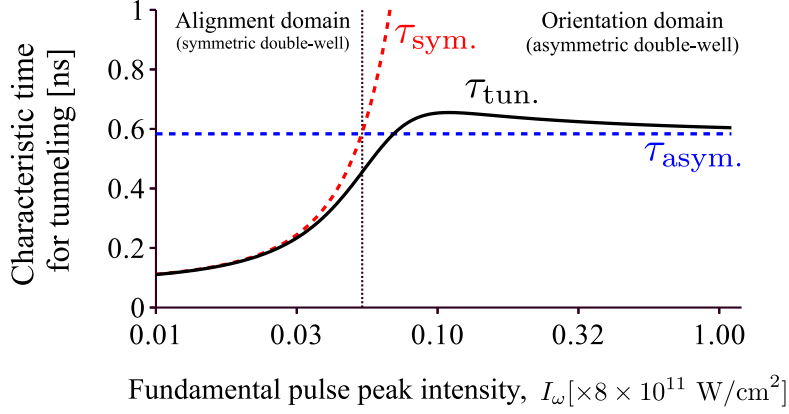


Fig. 2.7: Characteristic time for tunneling (black curve) in a double well potential when an asymmetric potential of Eq. (2.41) is created by an electrostatic field. The red dashed curve denotes $\tau_{\text{sym.}}$, which is calculated from Eq. (A.11) by using the symmetric double-well model for the symmetric part of the potential of Eq. (A.14). The blue dashed line denotes $\tau_{\text{asym.}}$, which is derived from Eq. (A.15) by finding the shift in energy ΔV_0 from the electrostatic term μE_S .

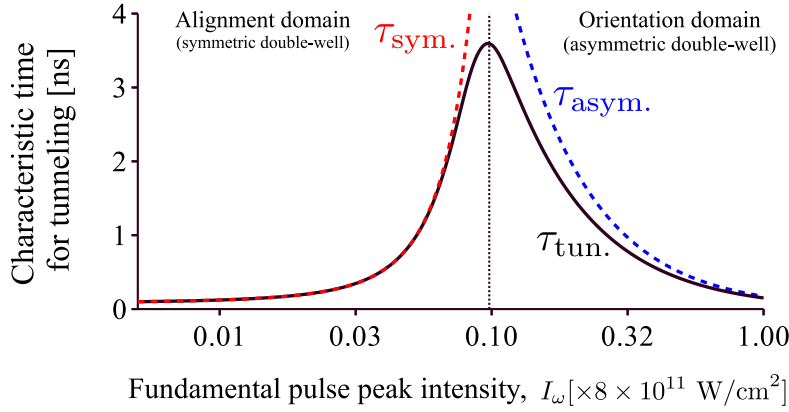


Fig. 2.8: Characteristic time for tunneling (black curve) in a double well potential when an asymmetric potential of Eq. (2.42) is created by an all-optical method. The red dashed curve denotes $\tau_{\text{sym.}}$, which is calculated from Eq. (A.11) by using the symmetric double-well model for the symmetric part of the potential of Eq. (2.42). The blue dashed line denotes $\tau_{\text{asym.}}$, which is derived from Eq. (A.15) by considering only the asymmetric part of the total potential given by Eq. (2.42).

the characteristic time required for tunneling from the following expression [72, 97, 102]:

$$\tau_{\text{tun.}} = \frac{2\pi\hbar}{|E_2 - E_1|} \quad (2.43)$$

For the electrostatic field, $\tau_{\text{tun.}}$ is plotted in figure 2.7 as a function of the intensity of the fundamental pulse I_ω . Here, we have used OCS molecules as samples. The permanent dipole moment for OCS molecule is $\mu = 2.36 \times 10^{-30}$ Cm. The electrostatic field used in the simulation is $E_S = 2.4$ kV/cm. All other parameters are summarized in the tables 2.1 ad 2.2. From this figure, we can see that the creation

of the symmetric double-well potential is initially dominant as given by the dashed red curve. This curve represents $\tau_{\text{sym.}}$, which is calculated from the difference in the eigenenergy $|E_2 - E_1|$ for the first two eigenstates when the symmetric Hamiltonian given by Eq. (2.40) is considered and the asymmetry created by the electrostatic field is ignored. However, from the point when $|E_2 - E_1| \sim \Delta V_0$ (denoted by the black dotted line), the characteristic time for tunneling $\tau_{\text{tun.}}$ is explained by the term ΔV_0 only, where $\Delta V_0 = 2\mu E_S$ is the asymmetry in the total potential created by the electrostatic field.

For an all-optical method, similar graph is plotted in figure 2.8 as a function of the intensity of the fundamental pulse I_ω . The intensity of the second harmonic pulse is also increased with the ratio of $I_{2\omega} = 0.44I_\omega$ in this case. From this figure, we understand that the effect of the symmetric double-well potential is initially dominant in the all-optical method as well. The asymmetric part of the potential becomes dominant when the condition $|E_2 - E_1| \sim \Delta V_0$ is met (black dotted line), where $|E_2 - E_1|$ is the difference in eigenenergies of the first two eigenstates of a symmetric Hamiltonian ignoring the asymmetric part of the potential in Eq. (2.42) and ΔV_0 is the asymmetric part of the same potential.

In both figures 2.7 and 2.8, the criteria $|E_2 - E_1| > \Delta V_0$ and $|E_2 - E_1| < \Delta V_0$ can be used to denote an initially dominant alignment dynamics domain which is governed by the formation of a symmetric double-well potential and the final orientation dynamics domain which is mostly controlled by the asymmetric part of the total potential, respectively.

For the electrostatic field, as shown in figure 2.7, the characteristic time for tunneling is around 0.6 ns. However, for the all-optical method, it is around 3.5 ns, almost an order of magnitude higher than that of the electrostatic field method. This means that nonadiabatic characteristics are relatively more likely to be induced in the all-optical method. For an all-optical method to be adiabatic, the laser pulses have to be steady for as long as 4 ns. Although this estimate is for OCS molecules, since the relative hyperpolarizability and polarizability anisotropies would not change drastically in other general molecules, the order of this characteristic time for tunneling in an all-optical method will not vary that much. If the laser pulse is not steady for as long as 4 ns, the initial eigenstates of the freely rotating molecule will not adiabatically connect to the instantaneous eigenstates of the field-dressed Hamiltonian, and the degree of molecular orientation will decrease. However, once we manage to cross the peak of the $\tau_{\text{tun.}}$ adiabatically, we come to the Orientation domain where the transition is governed by the asymmetry in the potential. While the characteristic time for tunneling $\tau_{\text{tun.}}$ converges to a steady value as shown in figure 2.7, $\tau_{\text{tun.}}$ keeps decreasing and becomes very low at the peak of the laser pulses in the all-optical method (figure 2.8). This is an indication that higher degrees of molecular

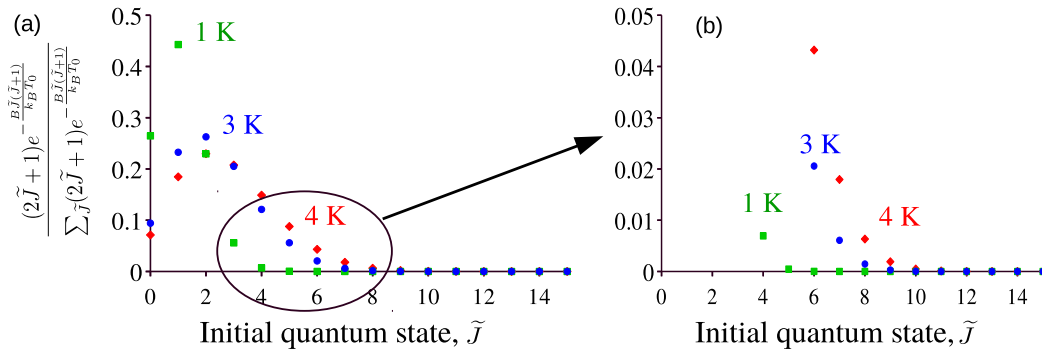


Fig. 2.9: Boltzmann weights for initial states

orientation are realized in an all-optical method provided that the change in laser pulse is slow enough to allow an adiabatic dynamics.

2.6 Numerical solution of TDSE describing molecular orientation

Implementing Eq. (2.37) requires one to solve a system of linear differential equations as shown in Eq. (2.29). Since the time-dependent Schrödinger equation Eq. (2.29) is more straightforward, will solve this equation. The difficulty in seeking such a numerical solution is in the enormous number of iterations required to simulate the experimental conditions. We need to simulate for around 24 ns ($2 \times \text{FWHM} = 24 \text{ ns}$) with a time step of $\sim 10 \text{ fs}$, which means that we require around 2,500,000 iterations for simulating a single initial state. If each step requires 1 ms, which is very optimistic, a single run requires a whopping 40 hours to complete. Moreover, we need to repeat this for all the initial states for which the Boltzmann weight, $w_{\tilde{J}} = \frac{(2\tilde{J}+1)e^{-\frac{B\tilde{J}(\tilde{J}+1)}{k_B T_0}}}{\sum_{\tilde{J}}(2\tilde{J}+1)e^{-\frac{B\tilde{J}(\tilde{J}+1)}{k_B T_0}}}$ is not negligible. From figure 2.9, we see that for

an initial temperature $T_0 = 4 \text{ K}$, we need to calculate all the states up to $\tilde{J} \sim 11$. As each \tilde{J} has $2\tilde{J} + 1$ degenerate states, at least $(\tilde{J} + 1)^2 = 144$ initial states have to be considered for estimating $\langle\langle \cos^2 \theta \rangle\rangle(t)$ and $\langle\langle \cos \theta \rangle\rangle(t)$ at $T_0 = 4 \text{ K}$. Many approaches have been tried to tackle this huge computational task, each with some specific advantages and disadvantages.

2.6.1 Higher-order Runge-Kutta method

The Higher-order Runge-Kutta method is fast enough for most problems [136–139] and advanced techniques such as adaptive step size control [140], embedded Runge-Kutta formulae [141], and Bulirsch-Stoer extrapolation [142] etc. can be implemented. However, the Runge-Kutta method does not ensure that the wave function

is normalized at every step. Hence, one needs to ensure that $\langle \Psi(t) | \Psi(t) \rangle = 1$ at each step separately. Since the total number of iterations required to simulate our experimental conditions is huge, normalizing the wave function at each iteration severely limits the usefulness of applying the Runge-Kutta method to our problem.

2.6.2 Operator splitting method

For one-dimensional Schrödinger equation given by,

$$i \frac{\partial}{\partial t} |\Psi(x, t)\rangle = (\hat{p}^2 + V(x)) \cdot |\Psi(x, t)\rangle. \quad (2.44)$$

The Eq. (2.44) is nondimensionalized by replacing the energy E , time t , and displacement x by $\frac{E}{E_0}$, $\frac{tE_0}{\hbar}$, and $\frac{x\sqrt{2mE_0}}{\hbar}$, respectively, where E_0 is the normalization energy specific to the system. The solution can be written with a unitary time evolution operator [137, 143]:

$$|\Psi(x, t)\rangle = U(t - t_0) |\Psi(x, t_0)\rangle = e^{-i\{\hat{p}^2 + V(x)\}(t-t_0)} |\Psi(x, t_0)\rangle. \quad (2.45)$$

Using the Baker-Campbell-Hausdorff formula, the time evolution operator can be approximated by two separate operators \hat{p}^2 and $V(x)$ [117, 137, 139, 144, 145]:

$$e^{-i\{\hat{p}^2 + V(x)\}\delta t} = e^{-iV(x)\frac{\delta t}{2}} e^{-i\hat{p}^2\delta t} e^{-iV(x)\frac{\delta t}{2}} + \mathcal{O}(\delta t^2). \quad (2.46)$$

The method of operator decomposition is sometimes referred to as the Lie-Trotter-Suzuki decomposition [146–150]. By using a Fourier Transformation at each step, this formulation can reduce the nondiagonal matrix-vector multiplication to a diagonal matrix-vector multiplication. For a Fourier pair $|\Psi(x, t)\rangle$ and $|\tilde{\Psi}(k, t)\rangle$, the operations $e^{-iV(x)\frac{\delta t}{2}} |\Psi(x, t)\rangle$ and $e^{-i\hat{p}^2\delta t} |\tilde{\Psi}(k, t)\rangle$ are multiplications of the exponential of a diagonal matrix and a vector. On the other hand, $e^{-iV(x)\frac{\delta t}{2}} |\tilde{\Psi}(k, t)\rangle$ and $e^{-i\hat{p}^2\delta t} |\Psi(x, t)\rangle$ are multiplications of the exponential of a nondiagonal matrix and a vector. To avoid a multiplication with the exponential of a nondiagonal matrix, we go back and forth from $|\Psi(x, t)\rangle$ to $|\tilde{\Psi}(k, t)\rangle$ at each step. For spatial coordinate system \mathbf{x} - and the reciprocal \mathbf{k} -space, this can be performed efficiently by the well developed Fast Fourier Transformation algorithm. However, while simulating molecular orientation, we deal with the space (ϕ, θ, χ) and the reciprocal space defined by the Wigner D-matrices or the spherical harmonics. The spherical harmonics are eigenstates of the operator $B\mathbf{J}^2$ in Eq. (2.15), so this operation is a diagonal matrix-vector computation. On the other hand, the interaction potential matrix elements in Eq. (2.15) are nondiagonal when spherical harmonics basis functions are used. So we need an efficient algorithm which can transform the wave function from the spatial (ϕ, θ, χ) system to the spherical harmonics basis

functions. However, there are some modules which implement the Trotter-Suzuki decomposition scheme on cluster computer CPUs and GPUs using OpenMP and CUDA, without performing the Fourier Transformation [151–153].

2.6.3 Time evolution with the field-dressed Hamiltonian

eigenstates

If the potential in Eq. (2.44) varies slowly with time, we can approximate it with a series of step functions. The exponential of a nondiagonal Hamiltonian is computed by finding the eigenvalues and eigenvectors in this method. At step i , we can express the time evolution operator with the eigenstates $|E_{n,i}\rangle$ of the field-dressed Hamiltonian.

$$|\Psi(x, t_{i+1})\rangle = U(\delta t) |\Psi(x, t_i)\rangle = \sum_n e^{-iE_{n,i}t} \langle \Psi(x, t_i) | E_{n,i} \rangle | E_{n,i} \rangle. \quad (2.47)$$

To use this method for simulating molecular rotational dynamics, we need to eigendecompose the total Hamiltonian given by Eq. (2.15) at each step i . The width of these step functions depends on the parameters such as the laser pulse widths τ_1 and τ_2 , the free rotational constant τ_{rot} , the electric field strengths of laser fields $E_\omega(t)$ and $E_{2\omega}(t)$, etc. Generally, using Eq. (2.47) is meaningful when the laser intensity changes very slowly compared to the free rotational constant τ_{rot} , requiring fewer but relatively wider steps to approximate the original potential. However, eigendecomposition of the total Hamiltonian at each simulation step is not a trivial calculation. As general algorithms for finding eigenvalues and eigenvectors are of the order $\mathcal{O}(n^3)$, this method works well when the required number of basis states is relatively small. Molecular orientation with a linearly polarized two-color laser field has a potential which does not interact with states with a different M 's. The required number of states for simulating such an interaction is determined by J only. In this case, implementing Eq. (2.47) when the laser intensity changes slowly over a long time scale is useful. However, when elliptically polarized laser fields are used, the quantum number M does not remain a good quantum number, i.e., states with different M 's interact with each other. To simulate such cases, the required number of basis sets increases by an order of magnitude. Similarly, simulating three-dimensional orientation with an asymmetric top molecule further increases the matrix size by another order of magnitude. In such situations, the eigendecomposition of matrices at each simulation step is not efficient anymore.

2.6.4 Higher-order Crank-Nicolson method

We have used the higher-order Crank-Nicolson method [154, 155] to simulate all the results presented in this thesis. In this method, the unitary operator composed

of the exponential of a nondiagonal Hamiltonian as given by Eq. (2.45) is Taylor expanded:

$$\Psi\left(t + \frac{\delta t}{2}\right) = \left(1 - iH\frac{\delta t}{2} + i^2\frac{H^2\left(\frac{\delta t}{2}\right)^2}{2!} - i^3\frac{H^3\left(\frac{\delta t}{2}\right)^3}{3!} + i^4\frac{H^4\left(\frac{\delta t}{2}\right)^4}{4!} - \dots \right) \Psi(t), \quad (2.48)$$

$$\Psi\left(t + \frac{\delta t}{2}\right) = \left(1 + iH\frac{\delta t}{2} + i^2\frac{H^2\left(\frac{\delta t}{2}\right)^2}{2!} + i^3\frac{H^3\left(\frac{\delta t}{2}\right)^3}{3!} + i^4\frac{H^4\left(\frac{\delta t}{2}\right)^4}{4!} + \dots \right) \Psi(t + \delta t), \quad (2.49)$$

where $H = \hat{p}^2 + V(x)$. Solving for $\Psi(t + \delta t)$ as a function of $\Psi(x, t)$ from Eq. (2.48) and Eq. (2.49),

$$(H_{\mathcal{E}} + H_{\mathcal{O}}) \Psi(t + \delta t) = (H_{\mathcal{E}} - H_{\mathcal{O}}) \Psi(t), \quad (2.50)$$

where,

$$H_{\mathcal{E}} = 1 + i^2\frac{H^2\left(\frac{\delta t}{2}\right)^2}{2!} + i^4\frac{H^4\left(\frac{\delta t}{2}\right)^4}{4!} + \dots, \quad (2.51)$$

$$H_{\mathcal{O}} = iH\frac{\delta t}{2} + i^3\frac{H^3\left(\frac{\delta t}{2}\right)^3}{3!} + i^5\frac{H^5\left(\frac{\delta t}{2}\right)^5}{5!} + \dots. \quad (2.52)$$

In other words, the unitary time evolution operator of Eq. (2.45) can be written as the following expression:

$$\Psi(t + \delta t) = U(\delta t)\Psi(t) = \frac{H_{\mathcal{E}} - H_{\mathcal{O}}}{H_{\mathcal{E}} + H_{\mathcal{O}}}\Psi(t). \quad (2.53)$$

The operator $\frac{H_{\mathcal{E}} - H_{\mathcal{O}}}{H_{\mathcal{E}} + H_{\mathcal{O}}}$ is unitary. This ensures that the wave function is normalized after each propagation. Since finding the inverse of a matrix is an inefficient algorithm, the inverse matrix $(H_{\mathcal{E}} + H_{\mathcal{O}})^{-1}$ is never computed in practice to solve Eq. (2.53). Instead, $\Psi(t + \delta t)$ is directly solved from Eq. (2.50) using the well developed and efficient LAPACK and BLAS routines [156–158]. Decomposing in $H_{\mathcal{E}}$ and $H_{\mathcal{O}}$ is important because they save us from numerically computing the terms H^2, H^3, H^4, \dots twice for the left and right sides of Eq. (2.50). Moreover, implementing the k -th power of H as $H \cdot H^{k-1}$ reduces the number of matrix multiplication rather than separately computing H^k for each k .

2.6.5 Implementation of higher-order Crank-Nicolson method

To estimate the ensemble average of the degrees of alignment or orientation, we have to start our simulation for each initial pure state $|JM\rangle$ separately. From figure 2.9, this means that states at least up to $J = 11$ have to be computed for

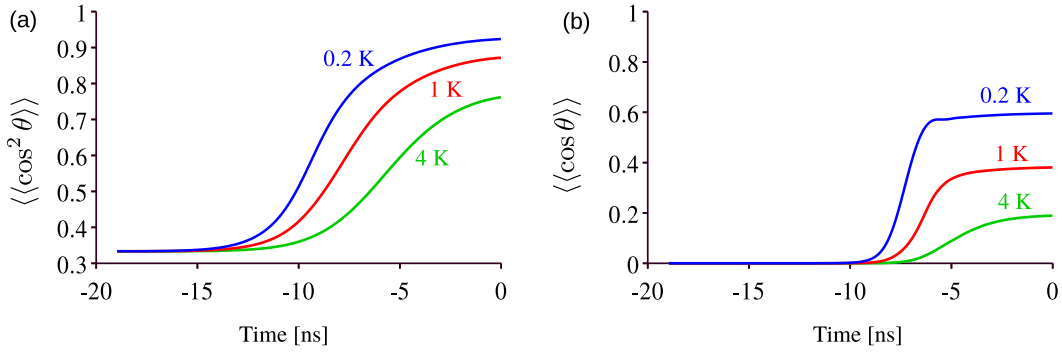


Fig. 2.10: $\langle\langle \cos^2 \theta \rangle\rangle$ and $\langle\langle \cos \theta \rangle\rangle$ of OCS molecule as a function of time. The peak intensities are, $I_\omega = 7.2 \times 10^{11}$ W/cm² and $I_{2\omega} = 3.5 \times 10^{11}$ W/cm². The HWHM of the fundamental pulse and the second harmonics are 6.32 ns and 4.65 ns, respectively. The fundamental wave is delayed by 1.75 ns with respect to the second harmonic which has its peak at 0 ns.

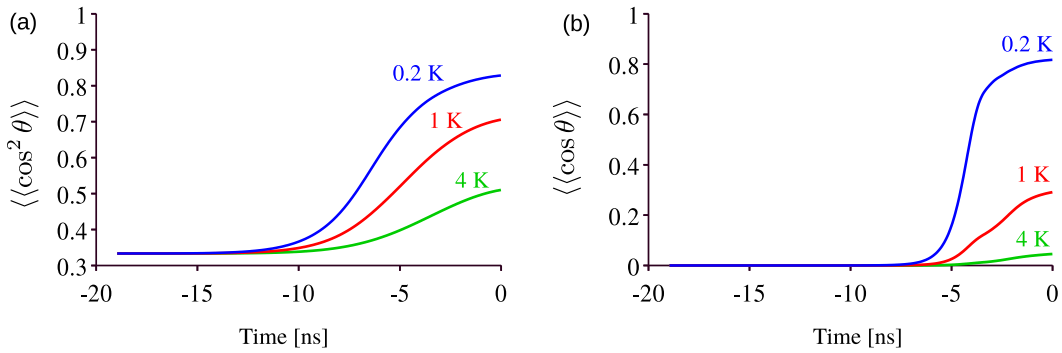


Fig. 2.11: $\langle\langle \cos^2 \theta \rangle\rangle$ and $\langle\langle \cos \theta \rangle\rangle$ of FCN molecule as a function of time. The peak intensities are, $I_\omega = 7.2 \times 10^{11}$ W/cm² and $I_{2\omega} = 3.5 \times 10^{11}$ W/cm². The HWHM of the fundamental pulse and the second harmonics are 6.32 ns and 4.65 ns, respectively. The fundamental wave is delayed by 1.75 ns with respect to the second harmonic which has its peak at 0 ns.

an initial temperature $T_0 \leq 4$ K, which makes the total number of initial states 144. Numerical simulations have been run in parallel for all these different initial conditions using the Reedbush-U supercomputer at the University of Tokyo [159, 160].

The codes are written in Python 3.6 using the packages “NumPy” and “SciPy” to solve Eq. (2.29) [161–168]. Reedbush-U has the “Intel Distribution for Python” and the “Intel Math Kernel Library” which implement the LAPACK and BLAS routines for matrix algebra by default [169]. These compilers are also optimized for the Intel based processors (Intel Xeon E5-2695v4: Broadwell-EP) that are implemented in the Reedbush system [159, 160, 170]. The parallelization is handled by the package “Mpi4Py” [171, 172]. The package “Pandas” is used to organize the simulated data, and plotting is performed using “Matplotlib” [168, 173, 174]. According to Eq. (2.29), when molecular orientation is achieved with a linearly polarized two-color

laser field, the quantum number M remains a good quantum number. States with a different M 's do not interact with each other. This makes the interaction potential matrix in Eq. (2.29) sparse [175–180]. Therefore, sparse linear algebra algorithms implemented in the “`scipy.sparse.linalg`” package significantly increase the calculation speed. However, when an elliptically polarized laser field is used, states with different M 's interact with each other, making the interaction potential matrix dense. In this situation, using the sparse matrix representation rather slows down the computation. The preferred solution, in this case, is to use the normal linear algebra algorithms implemented in the “`scipy.linalg`” module.

The simulated degrees of alignment and orientation for OCS molecules are presented in figure 2.10. The similar results for FCN molecules are shown in figure 2.11. Although OCS molecules have higher polarizability than that of FCN molecules, the ratio of the asymmetric potential compared to the total depth of the interaction potential is higher for FCN. As a result, the degree of orientation at a low initial rotational temperature (0.2 K) is higher for FCN molecules. However, the alignment is high for OCS molecule, so is the degree of orientation at a higher temperature such as 4 K. This trend is not understood by looking at the results in figures 2.4 or 2.5 where adiabatic approximation is applied. Both the degrees of alignment and orientation are high for OCS molecules when the adiabatic approximation is applied. But when nonadiabaticity in the process is not ignored and the TDSE of the dynamics is numerically solved, we see that the higher ratio of the asymmetric potential compared to the total interaction potential indeed plays an important role in the dynamics of all-optical molecular orientation.

Experimental observation of stronger molecular orientation

All-optical molecular orientation with a two-color nonresonant laser field has been observed experimentally [50–52, 54]. These were “proof of principle” experiments, proving the validity of the interaction potential given by Eq. (2.15). In [50], the reported degree of orientation is around $\langle\langle\cos\theta\rangle\rangle\sim\pm 0.04$. The direction of molecular orientation is opposite for states with even and odd quantum number J 's. Since the degree of orientation cancels each other, the molecular orientation is weakened when an average is taken for a thermal ensemble. Besides, in all-optical molecular orientation, a second harmonic generator is used to create the second harmonic pulse from the fundamental pulse. As a result, the rising part of the second harmonic pulse follows that of the fundamental pulse, creating the dominant symmetric potential through polarizability interaction before the weaker asymmetric potential through hyperpolarizability interaction can be formed. Due to these problems, the experimentally observed degree of orientation does not increase.

The purpose of the current study is to explore the ways of increasing the degree of orientation with an all-optical method. In our experiment, we applied two strategies to increase the degree of orientation: (1) select the lower-lying rotational states of OCS molecules as a sample by using a home-built molecular deflector and (2) adjust the rising parts of the two wavelengths of the pump pulse by introducing a Michelson-type delay line. By employing these two strategies, we have observed stronger degrees of molecular orientation with an all-optical method. In this chapter, the experimental methods and key results are discussed in details.

3.1 Overview of the experiment

We use the pump-probe technique to orient sample molecules and subsequently observe their angular distributions with the Velocity Map Imaging technique. For the two-color pump laser pulse, the fundamental pulse (1064 nm) and the second harmonic pulse (532 nm) from an injection-seeded Nd:YAG laser are used. The pump laser field has an FWHM of ~ 12 ns. A Ti:sapphire probe pulse of ~ 35 fs (FWHM) is used as the probe laser pulse. As shown in figure 3.1, both the pump and the probe laser pulses are focused using an achromatic lens into the sample gas. We use carbonyl sulfide (OCS) molecules diluted with He buffer gas as sample molecules. After the Coulomb explosion, the fragment ions are observed with the

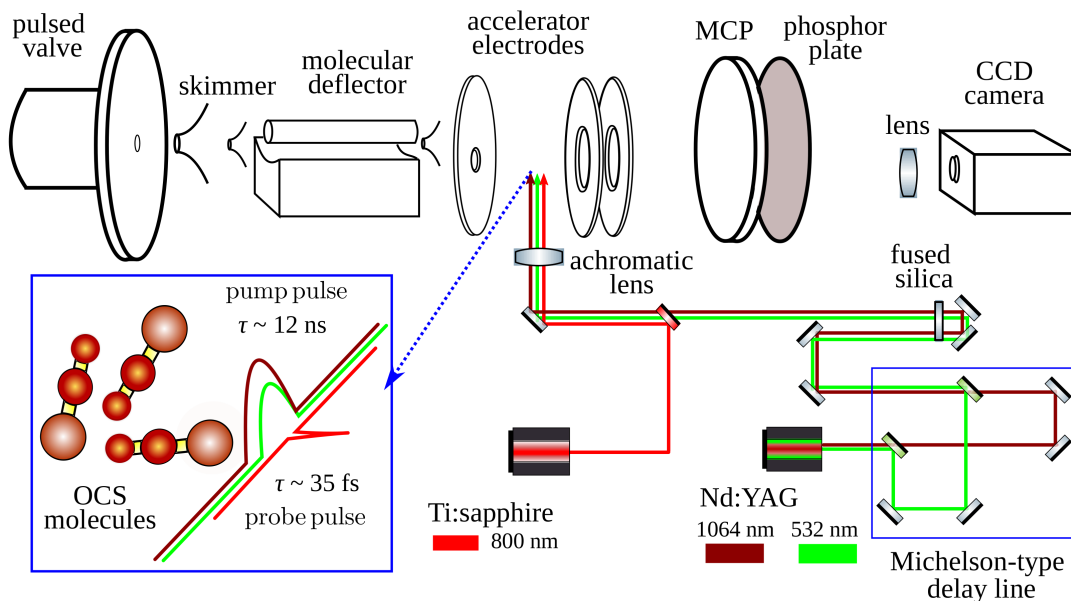


Fig. 3.1: Overview of the experiment for observing molecular orientation

Velocity Map Imaging (VMI) technique [24, 181]. These procedures are described in details in this chapter.

3.1.1 Even-Lavie valve

An Even-Lavie valve is a pulsed valve, which releases a relatively small amount of gas at each pulse. We use this pulsed valve as the source of rotationally cooled sample molecules. The characteristics of the Even-Lavie valve make it possible to achieve lower pressure inside the vacuum chamber. The valve is controlled by a current flowing from a 2000 μF condenser. This condenser is charged with 25 V, creating a 7-20 A current when discharged. This current passes through a solenoid, which induces a magnetic field to pull a moving plunger to open the valve. The plunger is attached to a spring. After the discharged current passes through the solenoid, the plunger is moved back to its original position by the spring, closing the valve. This mechanism happens with a repetition rate of 10 Hz. An Even-Lavie valve can produce gas pulses with FWHM as short as 15 μs [182, 183].

3.1.2 Supersonic expansion of sample molecules

A supersonic gas beam is used to generate collision-free sample molecules with a very narrow velocity distribution and extremely low rotational and vibrational energy [72, 183–186]. The translational, rotational, and vibrational energies of the sample OCS molecules inside the Even-Lavie valve are characterized by the temperature inside the valve. The molecules have a broad and slow velocity distribution, which is called the stagnation state (Mach number $\ll 1$). The gas molecules are

ejected into the source chamber which contains the skimmers as shown in figure 3.1. When the pressure difference between the Even-Lavie valve and the source chamber is adequately high, the thermal energy of the gas molecules is transferred to translational energy. The molecules collide with each other at the exit of the valve nozzle, and the rotational and vibrational temperatures are reduced. The degree of cooling of the internal rotational degree of freedom depends on the heat capacity ratio $\gamma = \frac{C_P}{C_V}$. To achieve a higher degree of cooling, monoatomic and neutral diluent gas such as He is used. This also minimizes the unwanted effect of condensation [184, 187, 188]. At the exit of the nozzle, the velocities of the molecules approximately approach the velocity of sound ($M \sim 1$). After the nozzle, the speed of the gas sample keeps increasing as they become freely flowing molecules. This increase in velocity happens up to an area defined by the Mach disk, and a skimmer is placed to collect the supersonic gas beam ($M > 1$) just before it reaches the boundary of the Mach disk. We use the Nd:YAG laser field to control the rotational dynamics of the molecules contained in this gas beam.

3.1.3 Velocity map imaging

The velocity map imaging (VMI) technique is used to directly measure the degree of orientation from observed angular distribution of the fragment ions produced after the ionization with the probe pulse. The accelerator electrodes, microchannel plate (MCP), and a phosphor plate are the components used in this technique. The vacuum chamber where these components are housed is called the detection chamber. The accelerator electrodes consist of three electrodes: the repeller, the extractor, and the ground. Fragment ions after the Coulomb explosion are accelerated toward the MCP due to this voltage drop across the electrodes. By tuning the voltage ratio between the repeller and the extractor, it is possible to focus the accelerated fragment ions in such a way that all the fragment ions with the same velocity vector arrive at the same point on the detector plane. The resolution of the point that represents a certain velocity component is not infinite. By tuning the voltages, this resolution can be made small enough to distinguish individual velocity vectors of the fragment ions [61, 62, 189]. The number of electrodes, the distance between them can be increased to further improve the resolution [190–193]. In this experiment, we use the conventional three-electrode system [61]. The MCP is placed at this focal plane with a high voltage potential between the two boundaries. The collected ion signal is exponentially amplified through repeated collisions and subsequent productions of electrons inside the channels of the MCP. These electrons are then accelerated toward the phosphor plate by the potential applied to the MCP. The phosphor plate produces fluorescence where the electrons hit it, and these signals are then recorded by a Charged Coupled Device (CCD) camera.

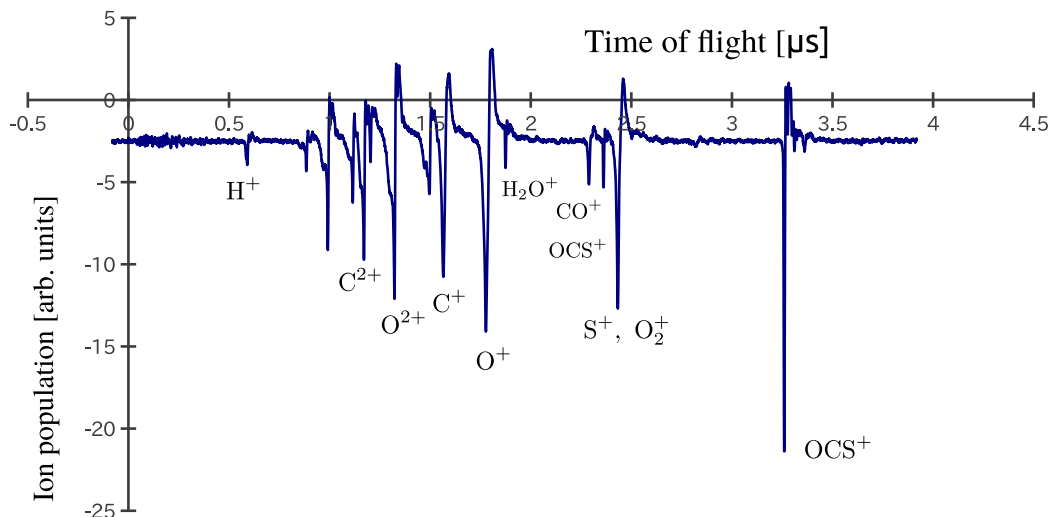


Fig. 3.2: Time-of-flight spectrum observed for identifying fragment ions.

3.1.4 Time-of-flight

The high voltage pulse applied to the MCP is adjusted to select fragment ions related to the sample molecules. When OCS molecules diluted with He gas are used, we observe either the S^+ or the CO^+ fragment. To select these fragments, we use the time-of-flight information. The time-of-flight is defined as the time required for a fragment ion to reach the MCP after ionization by the probe pulse. If the fragment ions are accelerated with a voltage V_R created by the accelerator electrodes, the energy given transferred to the fragment ion by the electric field is qV_R , where q is the charge of the accelerated ion. This energy is converted to kinetic energy $\frac{1}{2}mv^2$, where m is the mass and v is the velocity of the fragment ion. If the distance from the ionization point to the MCP is denoted as l , then $v = \frac{l}{t_{\text{TOF}}}$, where t_{TOF} is the time of flight of the ion. Finally, t_{TOF} is calculated from the following equation [189, 194–196],

$$t_{\text{TOF}} = \frac{l}{\sqrt{2V_R}} \sqrt{\frac{m}{q}}. \quad (3.1)$$

Since the parameters l and V_R are constants, t_{TOF} changes linearly with respect to $\sqrt{\frac{m}{q}}$. The time-of-flight spectrum as observed by an oscilloscope is shown in figure 3.2. When the flight times denoted by the negative peaks in figure 3.2 are plotted as a function of $\sqrt{\frac{m}{q}}$ for different fragment ions, a good linear fit is obtained, which is used to label the negative peaks with fragment ions as labeled in figure 3.2. This information can later be used to tune the timing of the high voltage pulse applied to the MCP, which makes it possible to amplify the signals related to some specific fragment ions such as S^+ , CO^+ , or OCS^+ , etc. In figure 3.2, the average values of a lot of measurements are taken. However, the relation between the different fragment ions can be visualized by plotting the covariance mapping as shown in

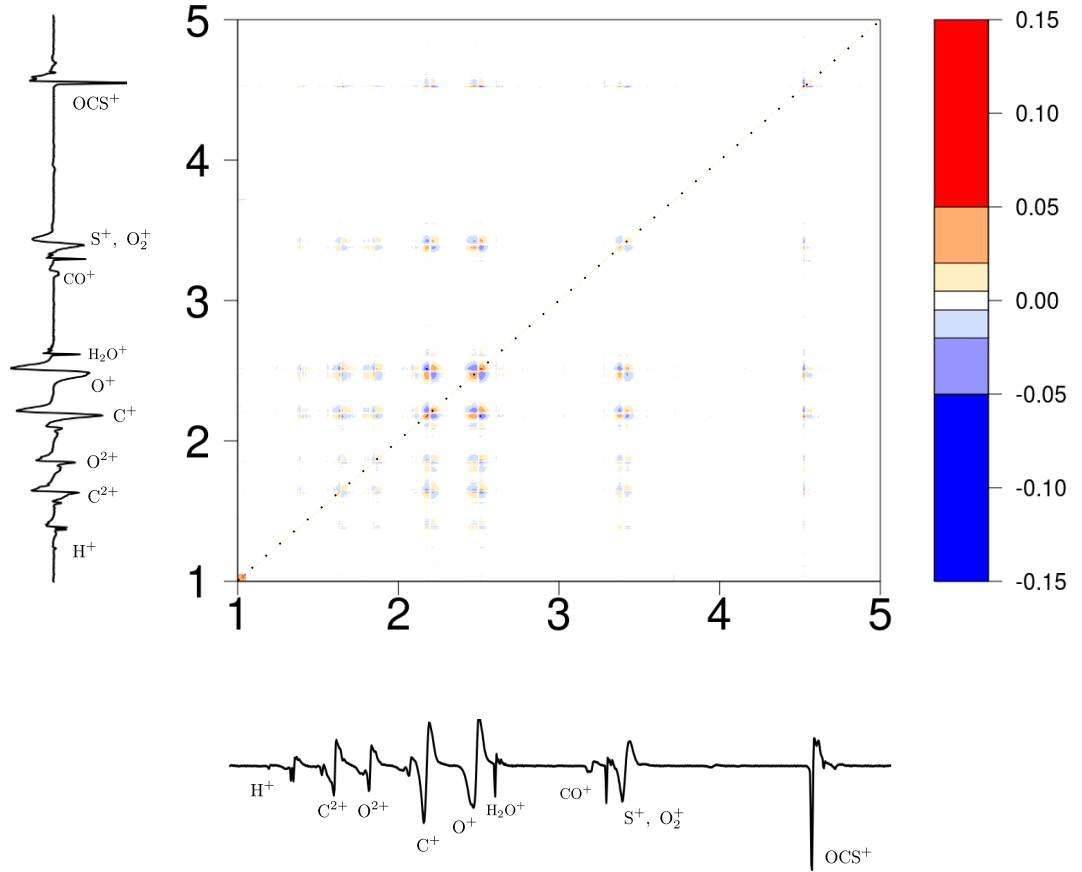


Fig. 3.3: Covariance mapping of ion population at different times of flight.

figure 3.3 [197–199]. For two ion population data $X(t)$ and $Y(t')$, the covariance mapping between the flight times of two ions at t and t' is given by,

$$C(t, t') = \frac{1}{N} \sum_{i=1}^N X_i(t) Y_i(t') - \left[\frac{1}{N} \sum_{i=1}^N X_i(t) \right] \left[\frac{1}{N} \sum_{i=1}^N Y_i(t') \right]. \quad (3.2)$$

From figure 3.3, we can see that the C^+ , O^+ , and S^+ ions are strongly correlated. The strong correlation among these three fragment ions is a signature that they come from the same parent OCS molecules. Moreover, the intermediate CO^+ ion intensity is very low compared to the C^+ , O^+ , and S^+ ion population. On the other hand, although the H_2O^+ ion has a pronounced peak, its correlation with other fragment ions produced from the parent OCS molecule is almost zero. The correlation of CO^+ is almost zero as well, but its original signal is also very weak. The OCS molecule mostly ionizes to C^+ , O^+ , and S^+ because of the high intensity of the probe laser pulse. However, since the availability of background gases such as CO_2 is extremely low inside the vacuum chamber, it can be assumed that the

CO⁺ fragment originates from OCS molecules. After considering all these facts, we observe the S⁺ and the CO⁺ fragment ions in our experiments.

3.1.5 Molecular deflector

Molecular orientation is strongly dependent on the initial rotational temperature of the sample molecules. Moreover, unlike alignment, the direction of orientation is opposite for odd and even J 's. Hence, a thermal ensemble of the sample molecules cancels out the degree of orientation achieved for states with even and odd J 's. This makes it harder to achieve higher degrees of orientation. By using a molecular deflector, we can select sample molecules lying in the lower rotational states by exploiting the Stark effect. The Stark effect happens when an external electric field interacts with polar molecules through the dipole moment resulting in an energy shift,

$$W = -\boldsymbol{\mu} \cdot \boldsymbol{\epsilon} = -\mu\epsilon\langle\cos\theta\rangle = -\mu_{\text{eff}}\epsilon, \quad (3.3)$$

where $\boldsymbol{\mu}$ is the dipole moment vector and $\boldsymbol{\epsilon}$ is the applied electric field vector [25, 40, 44, 200–208]. The Stark energy shifts for different states of an OCS molecule, together with the effective dipole moment $\mu_{\text{eff}} = -\frac{\partial W}{\partial \epsilon}$, are plotted in figure 3.4 [207]. This figure shows that the Stark energies can either decrease or increase depending on the state. This makes the effective dipole moment either positive or negative. Depending on the sign of the effective dipole moment, the molecules either orient or anti-orient their dipole moments with the electric fields. The orienting states are the high-field-seeking states as they are attracted toward the higher electric field. The anti-orienting states are low-field-seeking because they are attracted toward the lower electric field. To separate lower-lying rotational states, a molecular deflector exploits the state-specific effective dipole moment by creating a constant electric field *gradient* in one direction and a constant electric field in other perpendicular directions [203–205, 209, 210]. Although perfectly creating such a field is practically impossible, one can approximate such a field with a two-wire setting [211]. The force exerted on the molecule is given by,

$$\mathbf{F} = -\nabla W = \mu_{\text{eff}}(\epsilon) \cdot \nabla \epsilon. \quad (3.4)$$

The electric field distribution inside the molecular deflector used in this experiment is shown in figure 3.5 [183]. The molecular deflector is positioned between the source chamber and the (VMI) accelerator electrodes. This chamber is called as the deflector chamber. The OCS molecular beam profiles are measured twice by recording the signal intensities of the OCS⁺ ion: first without applying any voltage (0 kV) between the rod and the base of the molecular deflector, and then applying a high voltage of ~ 7 kV to deflect the lower-lying rotational states. The change in the measured OCS molecular beam profiles is compared in figure 3.6. The percentage

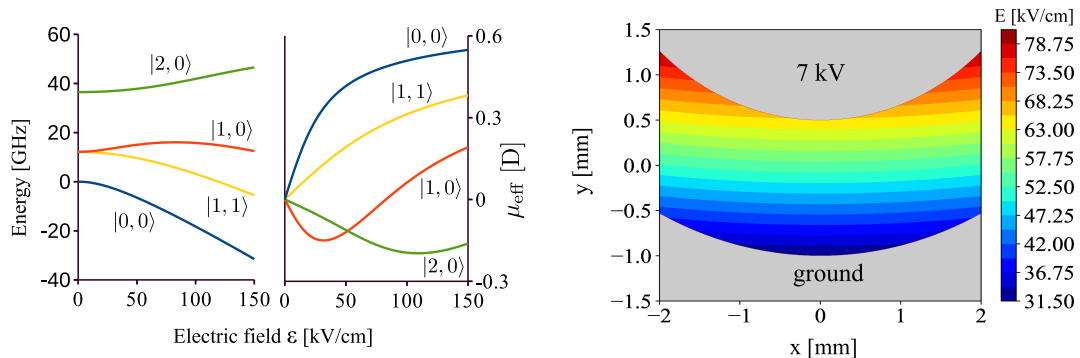


Fig. 3.4: Stark energies W (left panel) and effective dipole moments μ_{eff} (right panel) for different states $|JM\rangle$ of an OCS molecule. These energy curves are calculated using the Python package “CMIstark” [206].

Fig. 3.5: Distribution of the electric field generated between the deflector electrodes.

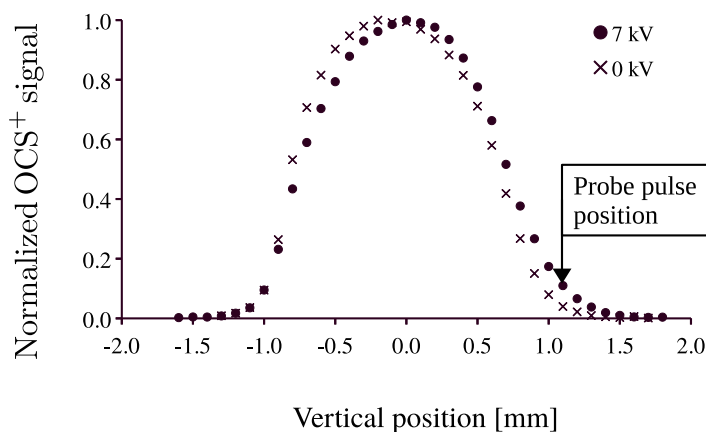


Fig. 3.6: Vertical profiles of OCS molecular beams.

of the lower-lying rotational states is higher in the upper region of the deflected profile. The probe pulse is positioned in this region as shown with an arrow in figure 3.6. We performed Monte-Carlo simulation of the deflected profile by using the technique described in [82, 204–207] to estimate the population distributions of various rotational states. The simulation result together with the measured profile of the deflected OCS molecules is shown in figure 3.7. Fitting the experimental profile is very critical because there are many independent parameters: the initial phase space distributions of the sample OCS molecules, the position and size of the skimmers, the initial rotational temperatures, and so on. The upper part is the most important area to fit because the lower-lying rotational states are abundant here. From the simulation, we can approximately estimate the relative populations of individual quantum states at different positions of the probe pulse. The estimated relative populations are shown in table 3.1. As we can see from this table, the relative population is highly sensitive to the position of the probe laser pulse. The

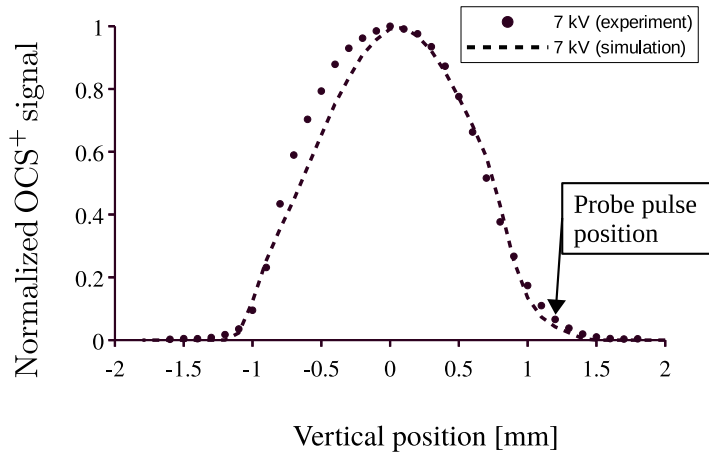


Fig. 3.7: simulated deflected profile of OCS molecular beam.

Tab. 3.1: Relative populations of individual quantum states in the deflected region of the molecular beam profile.

J	Probe pulse position		
	1.1 mm	1.2 mm	1.3 mm
0	0.16	0.5	0.88
1	0.23	0.43	0.12
2	0.14	0.06	-

ratio of the ground state is almost 90% at 1.3 mm, but the intensity of the ion population itself is very weak, making it difficult to gather sufficient data. In this experiment, the probe pulse is placed at 1.2 mm, where the ground state ration is about 50%. However, we have to remember that these estimations are highly sensitive to several parameters such as the rotational temperature before deflection, the initial uncertainty in the velocity and position of the sample molecules, etc. The number of parameters is too many compared to the available data points for fitting. As a result, the relative ratio as shown in table 3.1 is not precise beyond doubt. Nevertheless, it gives us a quantitative idea about the possible distribution of the states at the deflected region of the molecular beam.

3.2 Optical setup

The optical setup of our experiment is shown in figure 3.8. We use an injection-seeded Nd:YAG laser for the pump pulse and a Ti:sapphire laser for the probe

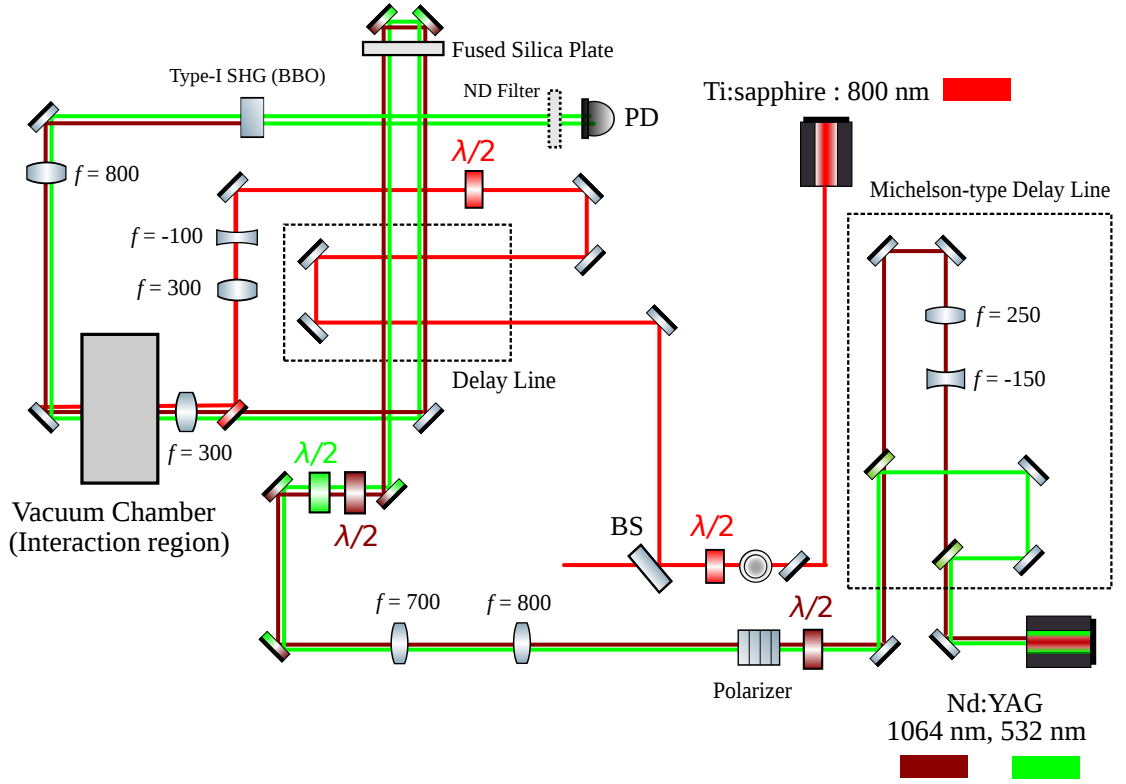


Fig. 3.8: Optical setup

pulse. The pump pulse is composed of two wavelengths: 1064 nm (fundamental pulse) and 532 nm (second harmonic pulse). The specifications of these laser pulses are summarized in table 3.2. The second harmonic pulse of the Nd:YAG laser is

Tab. 3.2: Details of the laser pulses used in this experiment.

Laser type	wavelength	FWHM	Peak intensity	Polarization
Pump pulse: fundamental pulse	1064 nm	12.64 ns	7.2×10^{11} W/cm ²	vertical
Pump pulse: second harmonic pulse	532 nm	9.3 ns	3.5×10^{11} W/cm ²	vertical
Probe pulse	800 nm	50 fs	5×10^{14} W/cm ²	horizontal

generated from the fundamental pulse using a KD*P crystal. From figure 3.8, three major optical arrangements can be identified:

1. Michelson-type delay line to adjust the relative delay between the rising parts of the fundamental pulse and the second harmonic pulse.

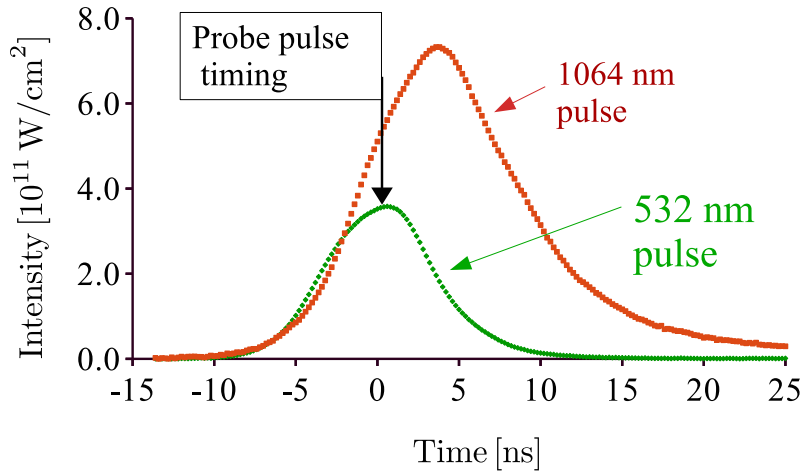


Fig. 3.9: Adjusting the rising parts of the two wavelengths with a Michelson-type delay line.

2. Real-time measurement of the relative phase difference using a type-I BBO crystal which generates a second harmonic pulse from the fundamental pulse of the Nd:YAG laser.
3. Fused silica plate to control the relative phase difference between the fundamental pulse and the second harmonic pulse.

Other components depicted in figure 3.8 are mainly used to guide and focus the laser pulses into the vacuum chamber where they interact with the molecular gas beam. Detailed discussions on the main optical components as listed above are given in the following paragraphs.

3.2.1 Michelson-type delay line

Since the second harmonic pulse is generated by nonlinear interaction of the fundamental pulse in the KD*P crystal, the rising part of the second harmonic pulse always follows that of the fundamental pulse. From the interaction potential term responsible for orientation in Eq. (2.15), a time lag between the two wavelengths will first align the asymmetric molecules, without orienting them to a single direction. In this situation, only the degree of alignment increases while the degree of orientation gets saturated [77–79, 82, 83]. Our strategy to avoid the saturation of the degree of orientation is to adjust the relative delay of the two wavelengths [79, 82]. By introducing a Michelson-type delay line as shown in figure 3.8, the fundamental pulse is delayed by 1.75 ns. The delayed fundamental pulse, together with the second harmonic pulse is measured and shown in figure 3.9. However, the

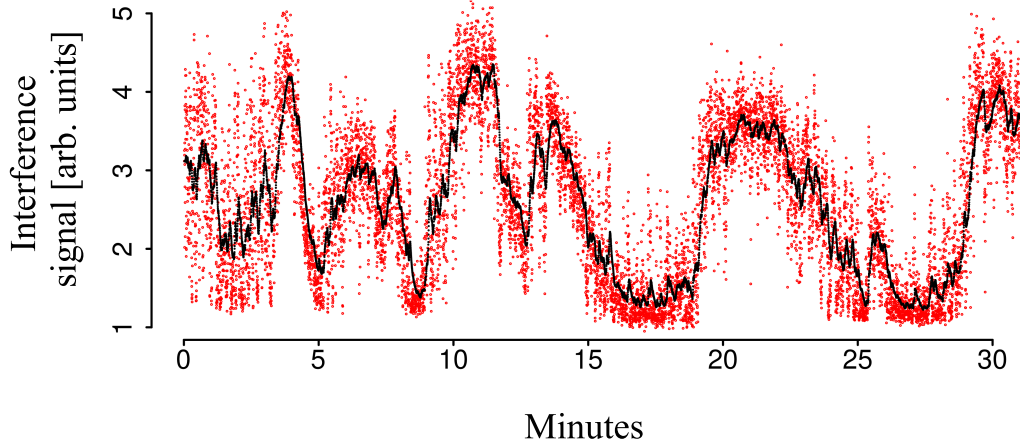


Fig. 3.10: Interference intensity (red dots) corresponding to the relative phase difference Φ as a function of time. The black line is the low pass filtered signal.

introduction of an interferometer with such a long arm length difference (52.5 cm) makes the relative phase difference between the two wavelengths unstable.

3.2.2 Real-time measurement of the relative phase difference

The pump laser pulses are collected after the vacuum chamber to measure the relative phase difference Φ . These waves are guided through a Type-I BBO crystal to generate a second harmonic pulse from the fundamental pulse. Part of the fundamental pulse is converted to the second harmonic, which interferes with the original second harmonic pulse. The interference signal is filtered and measured by a fast photodiode. For two waves given by $E_1 = A_1 \cos \frac{2\pi}{\lambda/2}(x + ct)$ and $E_2 = A_2 \cos \frac{2\pi}{\lambda/2}(x + ct + \Phi)$, the measured interference signal at the fast photodiode is given by,

$$I \propto A_1^2 + A_2^2 + A_3^2 + 2A_1A_2 \cos \frac{2\pi}{\lambda/2} \Phi, \quad (3.5)$$

where $\lambda = 1064$ nm and $E_3 = A_3 \cos \frac{2\pi}{\lambda}(x + ct)$ is the unconverted portion of the fundamental pulse. The existence of a strong background fundamental pulse seriously decreases the visibility of the interference signal. Neutral-density (ND) filters are used to scale the interference signal down to the sensitivity range of the detector fast photodiodes. Some of the filters are sensitive to the wavelength $\lambda = 1064$ nm, which are used to suppress the background signal and increase the visibility. An example of the measured interference signal is presented in figure 3.10. As shown in this figure, the relative phase difference Φ is unstable. This is due to all kinds of thermal noise, mechanical vibration, and constant noisy sound from nearby cooling and pumping apparatus, slight temperature variation in the laboratory, etc [212, 213]. Since these sources are random in nature and the interferometer is sensitive to these factors, the fluctuation in Φ is also random.

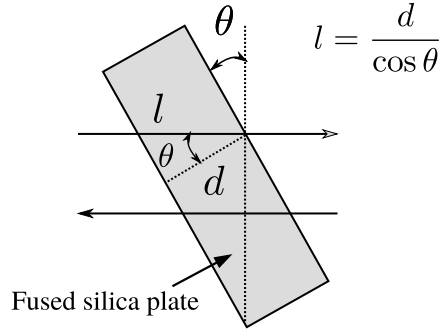


Fig. 3.11: Derivation of the relation between $\Delta\Phi$ and the angle of the fused silica plate.

3.2.3 Fused silica plate to control the relative phase difference between the two wavelengths

The fused silica plate is used to adjust the relative phase difference Φ between the fundamental pulse and the second harmonic pulse of the pump pulse. According to Eq. (2.15), the degree of orientation is modulated by the relative phase difference Φ . For a glass plate of width d , the change in the phase difference is given by,

$$\Delta\Phi = \frac{4\pi d}{\lambda} (n_\omega - 2n_{2\omega}) \left(\frac{1}{\cos \theta_f} - \frac{1}{\cos \theta_i} \right), \quad (3.6)$$

where $\lambda = 1064$ nm, θ_i, θ_f are the initial and final angular positions of the glass plate, and $n_\omega, n_{2\omega}$ are the refractive indices of the glass plate for the fundamental pulse and the second harmonic pulse, respectively. Eq. (3.6) is derived by replacing θ in figure 3.11 with θ_f and θ_i and taking the difference between the corresponding optical path lengths. By using Eq. (3.6), we can estimate the glass plate angular movement required to adjust Φ . The glass plate can be slowly rotated, changing θ_f to control Φ . There are some techniques which measure the fluctuation in the relative phase with photo diodes or CCD cameras with high sampling rates and feed the signal back to a piezoelectric transducer [213, 214]. In some other experiments, an extra CW laser pulse is used to lock the relative delays along the two arms of an interferometer [215, 216]. However, the interferometer used in our case is more complex, and the fluctuation in Φ as demonstrated in figure 3.10 is inherently random. Hence, due to the following distinctive characteristics of the Michelson-type delay line used in our experiment, stabilizing the relative phase difference Φ to a constant value is rather difficult. The main sources of difficulties are:

1. **Low sampling rate:** The highest possible sampling rate in our optical setup is 10 Hz, which is limited by the repetition rate of the Nd:YAG laser. Since the Nyquist frequency is 5 Hz, only the slowly varying component of the

phase fluctuation can be detected. Although there are some low-frequency fluctuations in Φ mainly stemming from the slowly and periodically changing room temperature or humidity, other sources such as noisy sounds from chillers and pumps, mechanical vibrations, etc. are of much higher frequency.

2. **Long arm-length difference:** The arm-length difference in an interferometer has to be shorter than the coherence length of the laser source to get a visibility greater than $1/e$ times the visibility at zero arm-length difference [217]. The two arms of the interferometer used in [214, 216] are of the same length, whereas the arm length difference in our experiment is 52.5 cm as shown in figure 3.8. A commercially available He-Ne laser has a coherence length of ~ 30 cm.
3. **Two-color laser field:** The interferometer used in this experiment is unique in the sense that it has two different wavelengths propagating through its two arms. The mirrors placed at the entrance of the interferometer reflect the second harmonic pulse and transmit the fundamental pulse. Besides, the mirrors at the back of the interferometer are dichroic. Because of the special characteristics of these mirrors, the intensity of the second harmonic pulse is reduced along the path of the fundamental pulse. Similarly, the intensity of the fundamental pulse is also reduced along the path of the second harmonic pulse. When another CW laser is used to stabilize the interferometer, reflections from the interferometer mirrors reduce the intensity inhomogeneously along the two arms, which decreases the visibility of the interference pattern.

The issues discussed above can be solved, but they require novel techniques and apparatus. However, the merit of implementing such a complex stabilizing system is limited as long as we are interested mainly in increasing the degree of molecular orientation. The purpose of using a Michelson-type delay line was to adjust the rising parts of the fundamental pulse and the second harmonic pulse, which was required to increase the degree of orientation achieved with an all-optical technique. We will provide experimental and theoretical evidence that the reason behind this is the fact that molecular orientation with an all-optical technique is nonadiabatic, even if the FWHM of the laser pulses is around 10 ns. We will show that the degree of orientation can be increased by tuning the relative intensities and the polarization of the two-color laser field.

3.3 Observation of stronger orientation

As demonstrated in Eq. (2.15), the observed degree of orientation is controlled by the phase difference Φ between the fundamental pulse and the second harmonic pulse. To observe higher degrees of upward or downward orientation, we have to look for the data which are taken when $\Phi \sim 0$ or $\Phi \sim \pi$. Moreover, the degree of

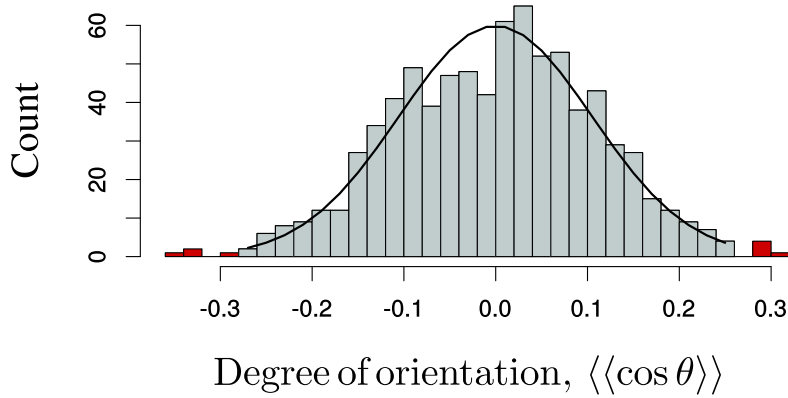


Fig. 3.12: Distribution of the observed degree of orientation.

orientation will be zero when $\Phi \sim \frac{\pi}{2}$. From figure 3.10, we know that Φ fluctuates randomly, which means that the probability of getting $\Phi \sim 0$ or $\Phi \sim \pi$ is low. Another fact to keep in mind is that the measured phase of figure 3.10 is the value of Φ observed by the fast photodiode is different from the absolute phase difference at the interaction region inside the vacuum chamber.

To be able to collect degrees of orientation data for all the possible phase differences, we have slowly moved the glass plate, scanning several full periods of Φ . Then, the degree of orientation $\langle\langle \cos \theta \rangle\rangle$ has been measured by observing the S^+ fragment ions. A two-dimensional image is taken every 10 seconds, and a single value of the degree of orientation $\langle\langle \cos \theta \rangle\rangle$ is calculated from this image. This composes one data point for $\langle\langle \cos \theta \rangle\rangle$. The laser operates with a frequency of 10 Hz, and at each shot, we get a number of fragment ions reaching the detector. A data-acquisition interval of 10 seconds for each count of $\langle\langle \cos \theta \rangle\rangle$ corresponds to 100 laser shots, each laser shot producing several fragment ions. This means we have information about the velocity vector of a few hundreds of fragment ions, which is enough to estimate statistically significant values for each count of $\langle\langle \cos \theta \rangle\rangle$. The degrees of alignment and orientation for each of these data points are estimated after proper calibration and removal of the background noise.

From figure 3.10, we see that although Φ removes randomly, sometimes faster than 10 ns, there are some moments when it is steady. By slowly removing the glass plate, we find instances when Φ is steady around the two optimal positions $\Phi \sim 0$ or $\Phi \sim \pi$. To be able to find both optimal and steady values of Φ , we need to increase the total accumulated data points. In our experiment, we have accumulated data for about 3 hours, which amounts to 1.08×10^5 laser shots.

After estimating the degree of orientation $\langle\langle \cos \theta \rangle\rangle$ from each block of data consisting of 100 laser shots, the histogram of $\langle\langle \cos \theta \rangle\rangle$ has been created and presented in figure 3.12. The distribution has long tails, where the phase difference Φ has its optimal

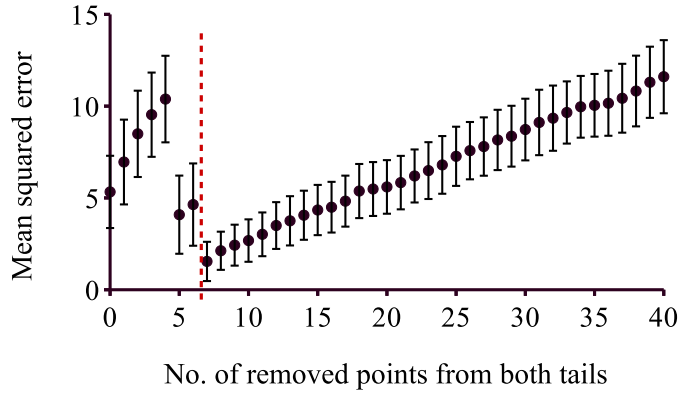


Fig. 3.13: The mean squared error (MSE) between the fitted Gaussian distribution and the histogram of $\langle\langle \cos \theta \rangle\rangle$ is plotted after removing several points from the upper and lower tails of the histogram. The horizontal axis shows the number of points that are removed.

values. After removing the data points belonging to these tails, we fit the histogram with a Gaussian distribution. The mean squared error (MSE) after the fitting is plotted in figure 3.13 as a function of the total removed points from both the higher and lower tails of the histogram. In this figure, we see that the MSE is minimum when around 6 highest and lowest data points are removed from the histogram. Moreover, the graph of the MSE can be separated into two groups, i.e., when the data points in the higher and the lower tails are (a) included in fitting, and (b) removed before fitting with a Gaussian distribution. The inclusion of data points in the tails rather increases the mean squared error of the fitting. These are data points when Φ is steady around the two optimal positions $\Phi \sim 0$ or $\Phi \sim \pi$. After collecting the data points of $\langle\langle \cos \theta \rangle\rangle$ that belong to this group, we have plotted the corresponding velocity map images in figure 3.14.

In figure 3.14 (a), an isotropic distribution is visible when only a probe pulse is used to observe the randomly oriented OCS molecules. The upward and downward orientation images are shown in figures 3.14 (b) and (c). The achieved degrees of orientation are: $\langle\langle \cos \theta \rangle\rangle \sim 0.28$ for upward orientation and $\langle\langle \cos \theta \rangle\rangle \sim -0.32$ for downward orientation. In these images, the polarization direction of the probe pulse is along the time-of-flight axis of the velocity map imaging (VMI) apparatus. We define it as the horizontal axis or the X axis in figure 2.1 (a). The polarization direction of the fundamental pulse and the second harmonic pulse of the pump Nd:YAG laser is perpendicular to the time-of-flight axis. This direction is defined as the vertical direction or the Z axis of the space-fixed frame as shown in figure 2.1 (a).

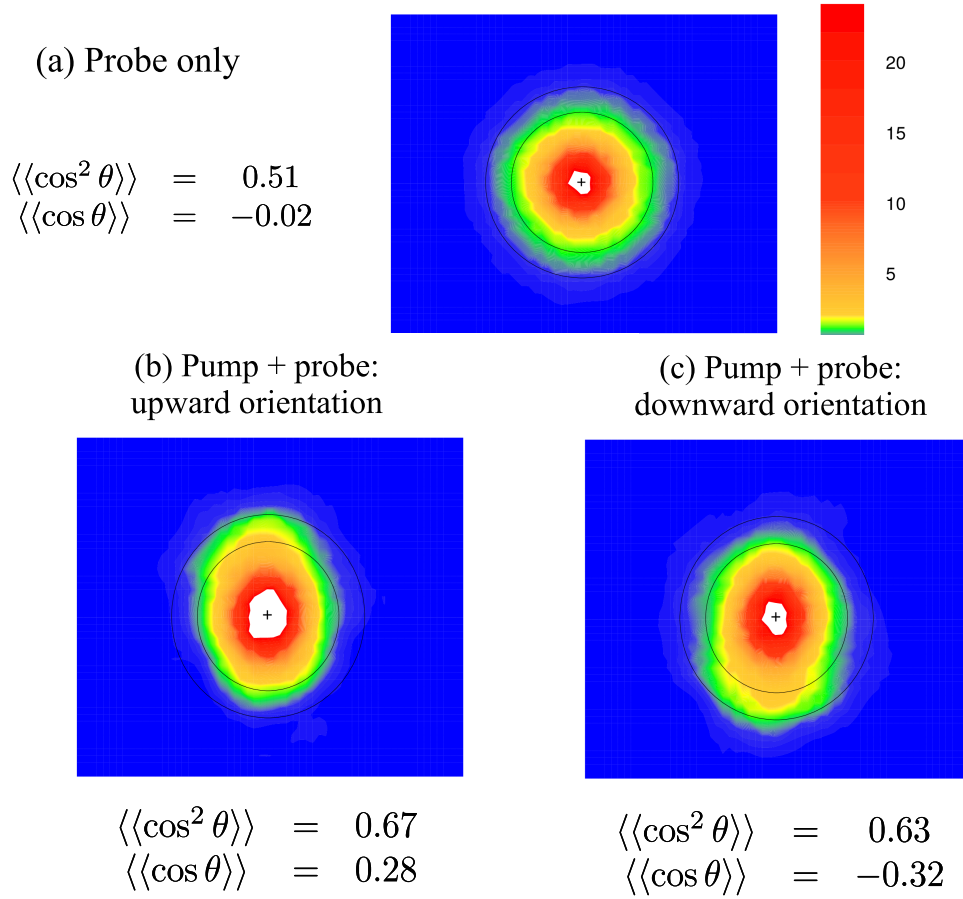


Fig. 3.14: Observation of strong upward and downward orientation. The S^+ fragment ions are used in this observation.

Tab. 3.3: Comparison of experimentally observed degree of orientation $\langle\langle \cos \theta \rangle\rangle$.

Ref.	year	Method	$\langle\langle \cos \theta \rangle\rangle$
[50]	2010	Direct observation with VMI, horizontally polarized probe pulse	0.04
[58]	2014	Estimated from observed high-harmonics	0.38
[60]	2014	Direct observation with VMI, vertically polarized probe pulse	0.2
[123]	2018	TOF mass spectrometry	0.12
This experiment	2018	Direct observation with VMI, horizontally polarized probe pulse	0.3

There are some reports on observation of strong nonadiabatic molecular orientation with a preceding alignment laser pulse followed by a two-color orienting laser pulse [58–60, 123]. The observed degrees of orientation in these experiments are summarized in table 3.3. In some experiments, the probing laser pulse is perpendicular to the time-of-flight axis. Since the probe pulse accelerates fragment ions after Coulomb explosion toward its polarization axis, aligning the polarization axes of the probe pulse and the pump pulse shows enhanced the degrees of alignment and orientation along the polarization direction of the pump laser field, even if the degree of alignment and orientation just before the Coulomb explosion is low [60]. In other experiments, the degree of orientation is not directly observed with techniques such as velocity map imaging. Rather, the degree of orientation is estimated from the high-harmonic spectra generated from the oriented CO molecules [58, 59]. In figure 3.14, the polarization of the probe pulse is vertical to the plane of the 2D image. As the probe pulse is radially symmetric, it does not enhance either the degree of alignment or the degree of orientation in this experiment. Comparing all these results, it can be said that the degrees of orientation presented in figure 3.14 are the strongest directly observed molecular orientation with the correct polarization of the probe laser pulse.

We can compare this result with the theoretical values of $\langle\langle\cos\theta\rangle\rangle$ shown in the figures 2.10 (b) and 3.16 (b). In these figures, for an initial rotational temperature $T_{\text{rot}} = 1$ K, the degree of orientation at the peak of the laser pulse is $\langle\langle\cos\theta\rangle\rangle \sim 0.38$. This estimate of the maximum degree of orientation can be increased by considering lower initial rotational temperatures. Judging from the relative populations of the initial states from the deflected profile of the molecular beam as summarized in table 3.1 and comparing it with the Boltzmann weights for initial states as shown in figure 2.9, we conclude that the initial rotational temperature is approximated by $T_{\text{rot}} = 1$ K in our experiment. As shown in figure 3.14, the observed degree of orientation in this experiment is $\langle\langle\cos\theta\rangle\rangle \sim 0.3$. In the theoretical calculation, the laser pulse is homogeneous in space. However, in practical situations, the degree of orientation is strongest at the center of the focus of the Gaussian laser beam, and laser intensity gradually falls away from here. This is called the “volume effect”. Due to these reasons, the experimentally observed degree of orientation is lower than the theoretically estimated maximum values of $\langle\langle\cos\theta\rangle\rangle$.

3.3.1 Nonadiabaticity in molecular orientation dynamics

Molecular orientation with a conventional two-color femtosecond laser pulse is weak. One way of increasing the degrees of molecular orientation is to use a preceding alignment pulse preceding the two-color orientation pulse [19, 55, 218]. The reports on observation of strong molecular orientation utilize this technique [58–60, 123]. Another way of increasing molecular orientation is to use longer laser pulses. The

higher energy of the nanosecond laser pulses is used in this technique to adiabatically orient the asymmetric molecules. Our goal in this experiment is to exploit these characteristics of nanosecond laser pulses in a two-color laser field setting.

However, a recent theoretical work has shown that even when pulses with FWHM ~ 12 ns are used, molecular orientation dynamics is still nonadiabatic [83]. To investigate this issue, we also have simulated the degrees of molecular alignment and orientation for OCS molecules using both the adiabatic approximation method and directly solving the time-dependent Schrödinger equation (TDSE). The results of the adiabatic approximation are shown in figure 3.15. By solving the TDSE directly, nonadiabatic characteristics of the orientation dynamics are correctly addressed, and the simulation results are presented in figure 3.16. In all these figures, the degrees of alignment and orientation for two initial rotational temperatures (1 K and 3 K) are plotted as a function of the intensity of the fundamental pulse I_ω . The peak intensity of the second harmonic pulse is fixed at $I_{2\omega} = 3.5 \times 10^{11}$ W/cm², and the degrees of alignment and orientation are estimated at the peak of the

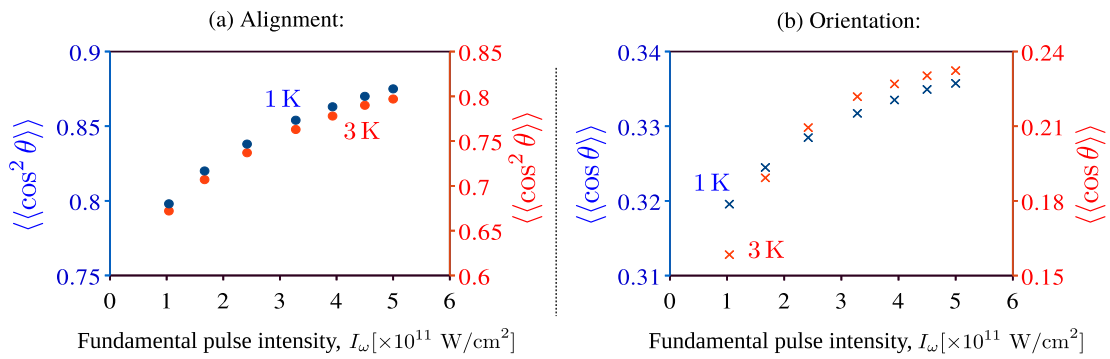


Fig. 3.15: Degrees of alignment and orientation for OCS molecules as a function of the fundamental pulse intensity (adiabatic approximation). The second harmonic pulse peak intensity is $I_{2\omega} = 3.5 \times 10^{11}$ W/cm².

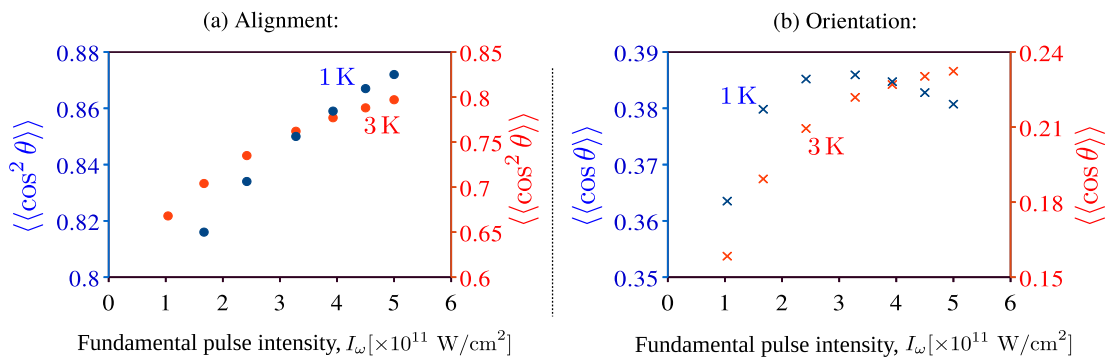


Fig. 3.16: Degrees of alignment and orientation for OCS molecules as a function of the fundamental pulse intensity (TDSE). The second harmonic pulse peak intensity is $I_{2\omega} = 3.5 \times 10^{11}$ W/cm².

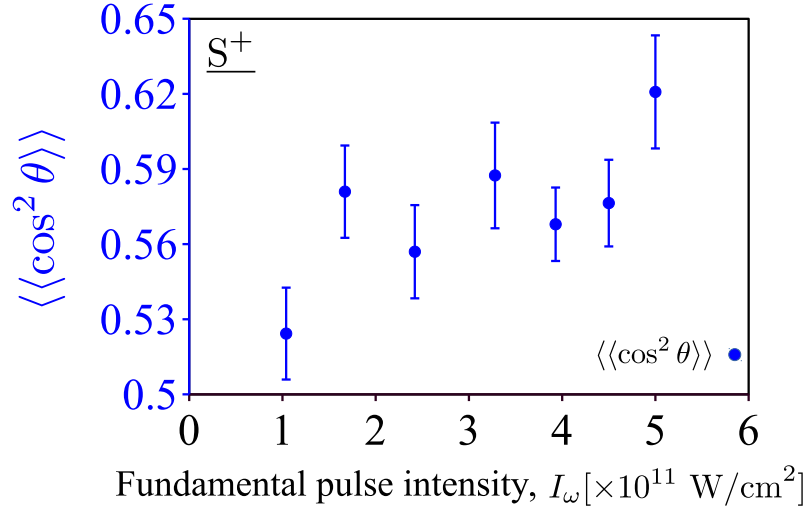


Fig. 3.17: Observed molecular alignment with S^+ fragment ion produced from OCS molecules as a function of the fundamental pulse intensity. The second harmonic pulse peak intensity is $I_{2\omega} = 3.5 \times 10^{11}$ W/cm 2 .

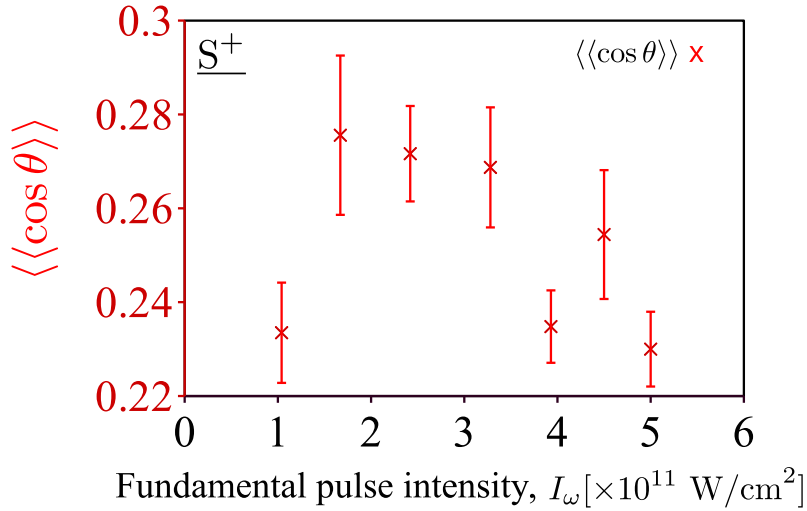


Fig. 3.18: Observed molecular orientation with S^+ fragment ion produced from OCS molecules as a function of the fundamental pulse intensity. The second harmonic pulse peak intensity is $I_{2\omega} = 3.5 \times 10^{11}$ W/cm 2 .

second harmonic pulse. The relative delay of 1.75 ns between the rising parts of the fundamental pulse and the second harmonic pulse is also duly considered in these simulations. All other parameters are kept the same as the experimental conditions as described in table 3.2.

From figure 3.15, one can see that both $\langle\langle \cos^2 \theta \rangle\rangle$ and $\langle\langle \cos \theta \rangle\rangle$ increase monotonically as a function of the fundamental pulse peak intensity under the adiabatic

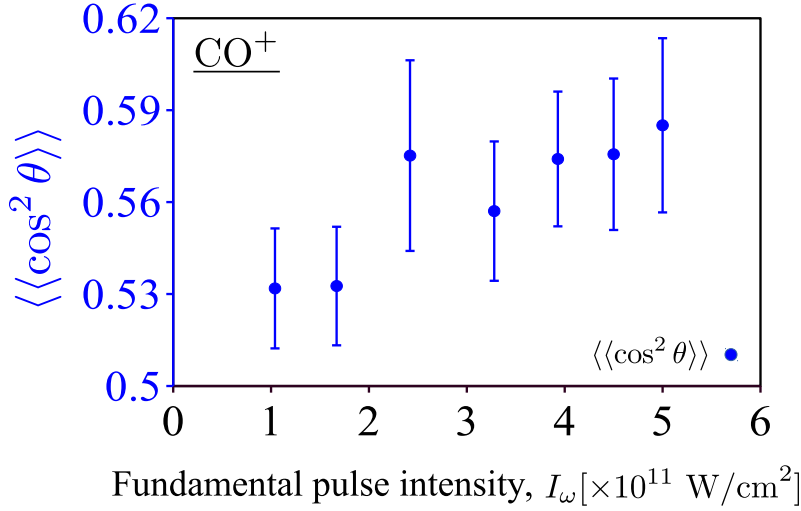


Fig. 3.19: Observed molecular alignment with CO^+ fragment ion produced from OCS molecules as a function of the fundamental pulse intensity. The second harmonic pulse peak intensity is $I_{2\omega} = 3.5 \times 10^{11} \text{ W/cm}^2$.

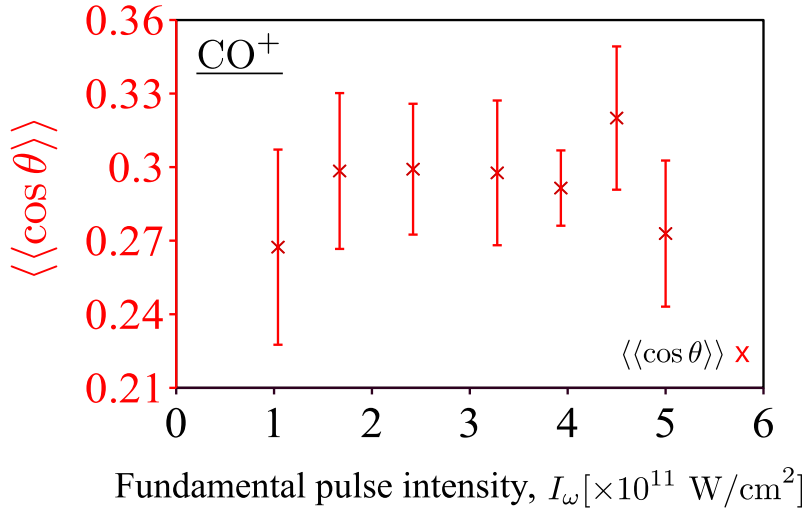


Fig. 3.20: Observed molecular orientation with CO^+ fragment ion produced from OCS molecules as a function of the fundamental pulse intensity. The second harmonic pulse peak intensity is $I_{2\omega} = 3.5 \times 10^{11} \text{ W/cm}^2$.

approximation assumption. However, as demonstrated in figure 3.16, directly solving the TDSE tells us that although the degree of alignment is a monotonically increasing function of the fundamental pulse peak intensity, the degree of orientation is not. In fact, for lower initial rotational temperature such as 1 K, $\langle\langle \cos \theta \rangle\rangle$ starts to decrease as the peak intensity of the fundamental pulse is increased. Moreover, the slope of the alignment curve in figure 3.16 is steeper for an initial rotational temperature of 1 K when compared to the same adiabatic curve in figure 3.15. This

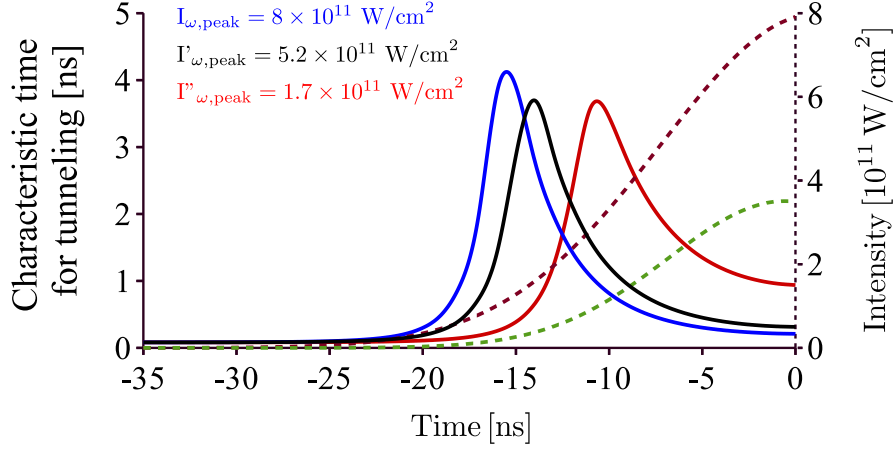


Fig. 3.21: Time profile of the characteristic time for tunneling τ_{tun} for fundamental pulses with different peak intensities. The intensity of the second harmonic pulse is $3.5 \times 10^{11} \text{ W/cm}^2$.

is an indication that the additional power used to increase the fundamental pulse intensity is preferably used to boost the degree of alignment, while the degree of orientation, although increases up to a maximum value, gradually gets saturated and then starts to decrease.

The intensity dependences of the degrees of alignment and orientation are also observed experimentally. Figures 3.17 and 3.18 show the measured alignment and orientation data when the S^+ fragment ions are used. Figures 3.19 and 3.20 present the data when the CO^+ fragment ions are observed to measure $\langle\langle \cos^2 \theta \rangle\rangle$ and $\langle\langle \cos \theta \rangle\rangle$, respectively. From both these graphs, we see that the degree of alignment $\langle\langle \cos^2 \theta \rangle\rangle$ increases with the peak intensity of the fundamental pulse, and the degree of orientation $\langle\langle \cos \theta \rangle\rangle$ starts to fall after achieving the maximum value. It is experimentally evident that the molecular orientation with a $\sim 12 \text{ ns}$ two-color laser field is inherently nonadiabatic. When we increase the intensity of the fundamental pulse, more power is used to align the molecules.

To explain this phenomena, we refer to the models of symmetric and asymmetric double-well potentials as explained in appendix A.2 and section 2.5. By finding out the instantaneous eigenenergies E_1 and E_2 of the first two states of the field-dressed Hamiltonian, we can find out the characteristic time for tunneling τ_{tun} from Eq. (2.43) [72, 97]. The time evolution of τ_{tun} , is plotted for three fundamental pulse intensities in figure 3.21. The time profiles of the two color laser fields are also shown, where the dashed red curve represents the fundamental pulse and the dashed green curve represents the second harmonic pulse. We see in figure 3.21 that τ_{tun} has a peak. This is where the system is transforming from a symmetric double-well potential to an asymmetric double-well potential. At this point, the energy difference $|E_2 - E_1|$ between the first two eigenstates of a symmetric double-well potential equals the asymmetry ΔV_0 in the total potential: $|E_2 - E_1| \sim \Delta V_0$.

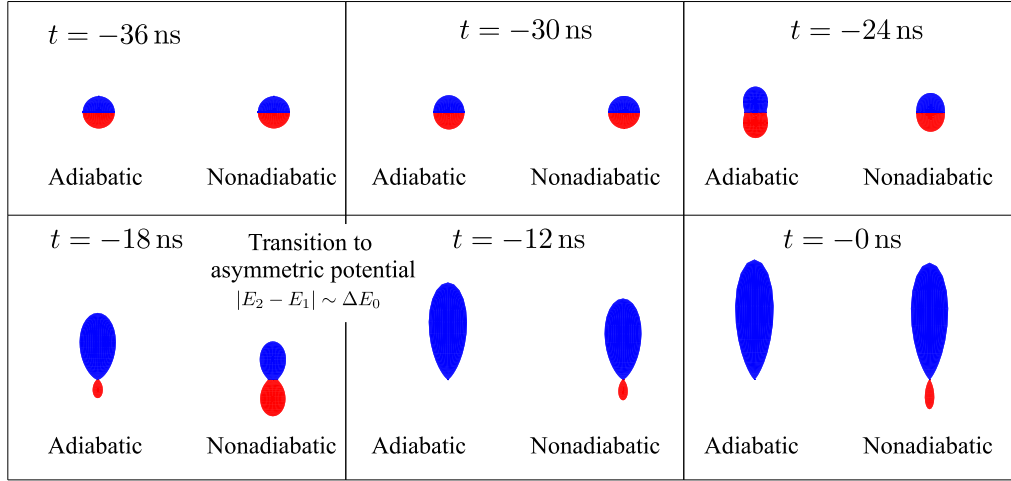


Fig. 3.22: Temporal evolution of the field-free eigenstate $|J, M\rangle = |0, 0\rangle$ under laser field. The spatial probability density profile of the wave function is plotted for both the adiabatic and the nonadiabatic processes. Blue and red colors are used for domains where $0 \leq \theta < \frac{\pi}{2}$ and $-\frac{\pi}{2} \leq \theta < 0$, respectively.

In the domain at the left of the peak, a symmetric double-well potential is gradually created, and molecular alignment is formed. As shown in figure 2.6 (a), the first two eigenstates, in this case, are the symmetric and antisymmetric eigenstates of the parity operator which inverts the θ -axis. A molecule in these wave functions stays in both the potential wells (both upwards and downwards) at the same time.

However, as time progresses, the condition $|E_2 - E_1| < \Delta V_0$ is met and we are on the right side of the peak of $\tau_{\text{tun.}}$. In this region, $\tau_{\text{tun.}}$ is governed by the the asymmetry in the total potential ΔV_0 as given by Eq. (A.15). In this domain, the phenomena is that of an asymmetric double-well, where the first two eigenstates, as shown in figure 2.6 (b) are localized in the regions defined by $0 \leq \theta < \frac{\pi}{2}$ (upward molecular orientation) and $-\frac{\pi}{2} \leq \theta < 0$ (downward molecular orientation), respectively. In essence, the nature of the eigenstates changes in this transition period. Hence, the characteristic time for tunneling $\tau_{\text{tun.}}$ has a peak here, which means that the transition here should progress very slowly to retain the ground state and ensure an adiabatic process. If the laser pulse is not changed slowly enough, the ground state evolves to a linear combination of the eigenstates of the asymmetric double-well potential. Since these eigenstates have the opposite direction of orientation, a linear combination of them will have a lower degree of orientation. This is why the degree of orientation is lower when the dynamics is nonadiabatic.

The time evolution of the ground state for both the adiabatic and nonadiabatic cases are shown in figure 3.22 for a peak fundamental pulse intensity $I_\omega = 8 \times 10^{11}$ W/cm². The intensity of the second harmonic pulse is kept constant at $I_\omega = 3.5 \times 10^{11}$ W/cm² in this case as well. The transition from a dominant symmetric double-well potential to a dominant asymmetric potential happens when $t \sim -18$ ns. This is

also where the peak of the characteristic time for tunneling $\tau_{\text{tun.}}$ exists in figure 3.21. We see in figure 3.22 that the wave function is transforming into the eigenstate of an asymmetric double-well potential at $t \sim -18$ ns when the dynamics is adiabatic. In contrast, for a nonadiabatic process, the wave function is transforming into a linear combination of the eigenstates of the asymmetric double-well potential. In this domain, the peak value of $\tau_{\text{tun.}}$ is around 4 ns, which means that the laser pulse has to be steady on the order of 5 nanoseconds for adiabatic dynamics to dominate. For a laser pulse to be steady on this scale, the HWHM of the Gaussian pulse has to be at least 50 ns. However, the longer the pulse is, the more adiabatic the dynamics will be.

Note that the degree of alignment, which is only related to the confinement of the eigenstates along the vertical direction, is increasing for both the adiabatic and the nonadiabatic processes. As a result, although a linear combination of eigenfunctions which have the opposite directions of orientation decreases the degree of molecular orientation, the degree of molecular alignment keeps increasing when the transition from the symmetric double-well potential to the asymmetric double-well potential happens.

When we decrease the intensity of the fundamental pulse to $I_\omega = 5.2 \times 10^{11}$ W/cm², the peak $\tau_{\text{tun.}}$ decreases. In a nonadiabatic dynamics, although the initial field-free ground state is still a linear combination of the first two eigenfunctions of the asymmetric double-well potential, the probability amplitude of the ground state, in this case, is larger than that of the case when $I_\omega = 8 \times 10^{11}$ W/cm². A decreased $\tau_{\text{tun.}}$ means that the initial wave function has a comparatively longer time to transit toward the ground state of the asymmetric double-well potential. Hence, the degree of orientation is larger, in this case, than the degree of orientation when $I_\omega = 8 \times 10^{11}$ W/cm². However, when the fundamental pulse laser intensity is too low, for example, $I_\omega = 1.7 \times 10^{11}$ W/cm², the asymmetry in the total potential ΔV_0 is too low. As shown by the red curve in figure 3.21, the characteristic tunneling time $\tau_{\text{tun.}}$ is very high at the peak of the laser pulses. Therefore, the achievable degree of orientation is decreased. This phenomenon, where the degree of orientation in a nonadiabatic molecular orientation dynamics first increases with the increase in laser intensity but starts to decrease when the laser intensity is too strong, is correctly reproduced in the experimental results shown in the figures 3.18 and 3.20.

If the dynamics is adiabatic, the initial field-free ground state will slowly transform to the ground state of the asymmetric double-well potential. Since this eigenfunction is oriented toward a single direction (upward), a deeper asymmetric potential created by stronger laser pulses will increase both the degrees of alignment and orientation. This is also understood by looking at the values of $\tau_{\text{tun.}}$ at $t = 0$ in figure 3.21. The characteristic time for tunneling $\tau_{\text{tun.}}$ is a monotonically decreasing function of the fundamental pulse intensity at the peak of the laser pulses ($t = 0$), which

means that higher degrees of molecular orientation are achieved in an adiabatic dynamics when stronger pulses are used to create a linearly polarized two-color laser field.

In this chapter, we have explained that, due to the nonadiabaticity in the molecular orientation dynamics, the degree of orientation does not increase even if we increase the intensity of a two-color laser field. In the next chapter, we will theoretically and numerically show that this unfavorable situation can be alleviated by using combined linearly polarized and elliptically polarized two-color laser fields. By using an elliptically polarized second harmonic pulse, it is possible to use the increased power for orienting the molecules to a single direction while suppressing the alignment potential.

All-optical molecular orientation with combined linearly and elliptically polarized two-color laser fields

In all-optical molecular orientation, intense, nonresonant two-color laser pulses are used to orient asymmetric molecules without the help of an electrostatic field. When an electrostatic field is present, the asymmetric potential responsible for orientation comes from the dipole moment interaction, which is a first-order interaction. However, when only two-color laser fields are used, the asymmetry in the interaction potential is due to the hyperpolarizability of the molecules, which is a third-order interaction. The symmetric potential in both cases is due to the polarizability of the molecules, which is the most dominant part in the total interaction potential when high-intensity laser fields are used.

If the molecular orientation process with a two-color laser field is purely adiabatic, increasing the intensities of the laser fields should increase the degree of orientation. However, as we have shown experimentally and theoretically in the previous chapter, all-optical molecular orientation is nonadiabatic even if we use two-color pulses with FWHM as long as ~ 12 ns. But unlike an electrostatic field, due to the nonadiabaticity in a usual all-optical molecular orientation dynamics, the dominant symmetric potential is formed before the asymmetric potential can be effective, resulting in a situation where only the degree of alignment increases and the degree of orientation does not increase efficiently. We propose a novel approach of increasing the degree of orientation efficiently under these conditions by introducing an elliptically polarized second harmonic pulse in the two-color laser field. In this chapter, we have discussed the issue in details both theoretically and numerically.

4.1 Definition of the laser field

A linearly polarized two-color laser field is given by Eq. (2.13). In the present approach, we have replaced the linearly polarized second harmonic pulse with an elliptically polarized one:

$$\begin{bmatrix} E_X(t) \\ E_Y(t) \\ E_Z(t) \end{bmatrix} = \begin{bmatrix} E'_{2\omega}(t) \sin(2\omega t + \Phi) \\ 0 \\ E_\omega(t) \cos \omega t + E_{2\omega}(t) \cos(2\omega t + \Phi) \end{bmatrix}. \quad (4.1)$$

In Eq. (4.1), the envelopes $E_\omega(t)$, $E_{2\omega}(t)$, and $E'_{2\omega}(t)$ are defined as Gaussian pulses:

$$E_\omega(t) = E_\omega e^{-\frac{t^2}{2\tau_\omega^2}}, \quad E_{2\omega}(t) = E_{2\omega} e^{-\frac{t^2}{2\tau_{2\omega}^2}}, \quad E'_{2\omega}(t) = E'_{2\omega} e^{-\frac{t^2}{2\tau_{2\omega}^2}}, \quad (4.2)$$

where ω and 2ω are the angular frequencies, τ_ω and $\tau_{2\omega}$ are the widths of the Gaussian envelopes of the fundamental pulse and the second harmonic pulse, respectively. E_ω is the peak intensity of the fundamental pulse. $E_{2\omega}$ and $E'_{2\omega}$ are the peak intensities along the two major axes of the elliptically polarized second harmonic pulse. Φ is the relative phase difference between the two wavelengths.

In contrast, we may think of changing the polarization of the fundamental pulse instead:

$$\begin{bmatrix} E_X(t) \\ E_Y(t) \\ E_Z(t) \end{bmatrix} = \begin{bmatrix} E'_\omega(t) \sin \omega t \\ 0 \\ E_\omega(t) \cos \omega t + E_{2\omega}(t) \cos(2\omega t + \Phi) \end{bmatrix}, \quad (4.3)$$

where, $E'_\omega(t) = E'_\omega e^{-\frac{t^2}{2\tau_\omega^2}}$ and E_ω and E'_ω are the peak intensities along the two major axes of the elliptically polarized fundamental pulse. In the following section, we will discuss the interaction potentials for both the cases and will show that the laser field defined by Eq. (4.1) is the effective combination. It should be noted that there is no delay between the fundamental pulse and the second harmonic pulse in this chapter, whereas in chapter 3 it is 1.75 ns. In experiments, the creation of such a long delay between the two-wavelengths degrades the coherency of Φ , which is inherently detrimental to the all-optical molecular orientation method.

4.2 Interaction potential

The nonlinear interaction potential of a linear asymmetric molecule with combined linearly and elliptically polarized laser fields defined by Eq. (4.1), after taking the average over $\frac{2\pi}{\omega}$, is expressed as follows:

$$\begin{aligned} \hat{H}_i(t) = & -\frac{1}{4}(\alpha_{\parallel} - \alpha_{\perp}) \left[\cos^2 \theta (E_\omega^2(t) + E_{2\omega}^2(t)) + \sin^2 \theta \cos^2 \phi E_{2\omega}^{\prime 2}(t) \right] \\ & \pm \frac{1}{8}((\beta_{\parallel} - 3\beta_{\perp}) \cos^2 \theta + 3\beta_{\perp}) \cos \theta E_\omega^2(t) E_{2\omega}(t), \end{aligned} \quad (4.4)$$

where, $\Phi = \pi$ or 0 . We can compare Eq. (4.4) with the interaction potential for the conventional linearly polarized two-color laser field:

$$\begin{aligned}\hat{H}_i(t) = & -\frac{1}{4}(\alpha_{\parallel} - \alpha_{\perp}) \left[\cos^2 \theta (E_{\omega}^2(t) + E_{2\omega}^2(t)) \right] \\ & \pm \frac{1}{8}((\beta_{\parallel} - 3\beta_{\perp}) \cos^2 \theta + 3\beta_{\perp}) \cos \theta E_{\omega}^2(t) E_{2\omega}(t),\end{aligned}\quad (4.5)$$

where, $\Phi = \pi$ or 0 . This is the same expression as used in Eq. (2.15), only that the $\cos \Phi$ term is replaced by a \pm sign for the two optimal directions $\Phi = \pi$ or 0 . Φ can be tuned to an optimal value by a glass plate as shown in figure 3.8 and explained by Eq. (3.6). It is also unrelated to the independent parameters such as ϕ, θ, χ and time t required to describe the molecular orientation dynamics. Moreover, intermediate values when $\Phi \neq \pi$ or $\Phi \neq 0$ introduce an extra $\sin \Phi$ term together with the usual $\cos \Phi$ term:

$$\begin{aligned}\hat{H}_i(t) = & -\frac{1}{4}(\alpha_{\parallel} - \alpha_{\perp}) \left[\cos^2 \theta (E_{\omega}^2(t) + E_{2\omega}^2(t)) + \sin^2 \theta \cos^2 \phi E_{2\omega}'^2(t) \right] \\ & -\frac{1}{8}((\beta_{\parallel} - 3\beta_{\perp}) \cos^2 \theta + 3\beta_{\perp}) \cos \theta \cos \Phi E_{\omega}^2(t) E_{2\omega}(t) \\ & -\frac{1}{8} \cos \phi \sin \theta \left[\beta_{\perp} \sin^2 \theta + (\beta_{\parallel} - 2\beta_{\perp}) \cos^2 \theta \right] \sin \Phi E_{\omega}^2(t) E_{2\omega}'(t).\end{aligned}\quad (4.6)$$

Compared to Eq. (4.4), we see that the extra $\sin \Phi$ term is associated with $\cos \phi \sin \theta$, which reduces the degree of orientation in the polarization plane of the elliptically polarized second harmonic pulse. Hence, the most convenient and useful approach is to consider the two special cases: $\Phi = \pi$ or 0 . We can also think of using an elliptically polarized fundamental pulse instead of changing the second harmonic pulse polarization as defined in Eq. (4.3). However, in this combination, the asymmetric potential created by the interaction through molecular hyperpolarizability is suppressed as well:

$$\begin{aligned}\hat{H}_i(t) = & -\frac{1}{4}(\alpha_{\parallel} - \alpha_{\perp}) \left[\cos^2 \theta (E_{\omega}^2(t) + E_{2\omega}^2(t)) + \sin^2 \theta \cos^2 \phi E_{2\omega}'^2(t) \right] \\ & \pm \frac{1}{8}((\beta_{\parallel} - 3\beta_{\perp}) \cos^2 \theta + 3\beta_{\perp}) \cos \theta E_{\omega}^2(t) E_{2\omega}(t) \\ & \mp \frac{1}{8} \left[(\beta_{\parallel} - 3\beta_{\perp}) \cos^2 \phi \sin^2 \theta + \beta_{\perp} \right] \cos \theta E_{\omega}'^2(t) E_{2\omega}(t),\end{aligned}\quad (4.7)$$

where, $\Phi = \pi$ or 0 . In this equation, the extra term corresponding to $E_{\omega}'^2(t) E_{2\omega}(t)$ has an opposite sign than the usual term $E_{\omega}^2(t) E_{2\omega}(t)$. Since these parts of the potential are responsible for molecular orientation, we end up suppressing both the degrees of alignment and orientation by adopting an elliptically polarized fundamental pulse as defined in Eq. (4.3). Hence, the most effective combination is to introduce an elliptically polarized second harmonic pulse while keeping the fundamental pulse polarization unchanged. In the remaining sections of this chapter, we

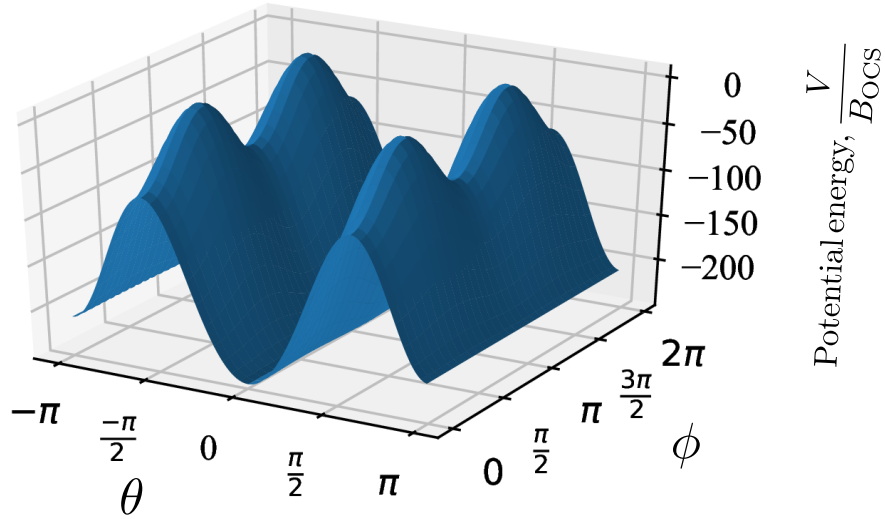


Fig. 4.1: Interaction potential as a function of θ and ϕ when a combined linearly and elliptically polarized two-color laser field defined by Eq. (4.1) is used to orient OCS molecules. The asymmetry between the two minima along the θ axis is exaggerated.

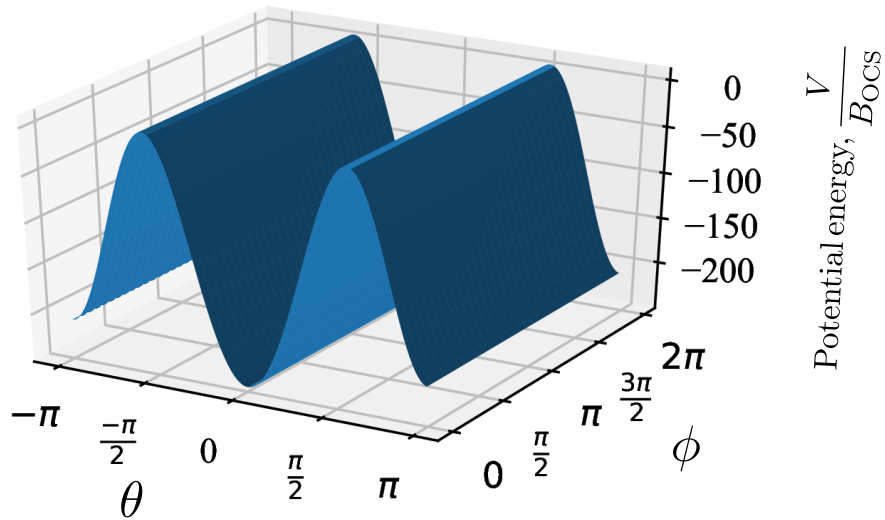


Fig. 4.2: Interaction potential as a function of θ and ϕ when a conventional linearly polarized two-color laser field defined by Eq. (2.13) is used to orient OCS molecules. The asymmetry between the two minima along the θ axis is exaggerated.

will discuss on the basis of this specific combination, where the laser field is defined by Eq. (4.1) and the interaction potential is given by Eq. (4.4).

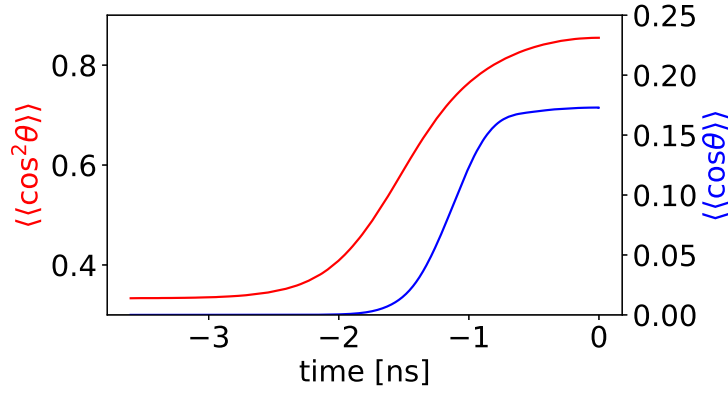
The interaction potential for OCS molecules when $\Phi = \pi$ is plotted in figure 4.1 when a combination of a linearly polarized fundamental pulse and an elliptically polarized second harmonic pulse is used in an all-optical molecular orientation tech-

nique. A similar potential is plotted in figure 4.2 when a conventional linearly polarized two-color laser field is used. The parameters θ and ϕ used as the axes are the Euler angles relating the space-fixed frame and the body-fixed frame as defined in figures 2.1 and 2.2. Although the height of the potential is suppressed in figure 4.1 at $\phi \sim 0$ and $\phi \sim \pi$, the potential is independent of ϕ in figure 4.2. The introduction of an elliptically polarized second harmonic pulse reduces the height of the potential barrier, increasing the transition probability from the shallower potential at $\theta = \pm\pi$ to the deeper potential at $\theta = 0$. This transition is most likely to take place along the directions $\phi \sim 0$ and $\phi \sim \pi$. In the case of a linearly polarized laser field as demonstrated in figure 4.2, no such path which facilitates the transition toward the deeper potential exists. When the molecules are trapped in either of the two local minima at $\theta \sim 0$ or $\theta \sim \pm\pi$, it is very unlikely that they would tunnel toward the global minimum. Increasing the laser intensity in this setting further improves the degree of alignment only, and the degree of orientation gets saturated.

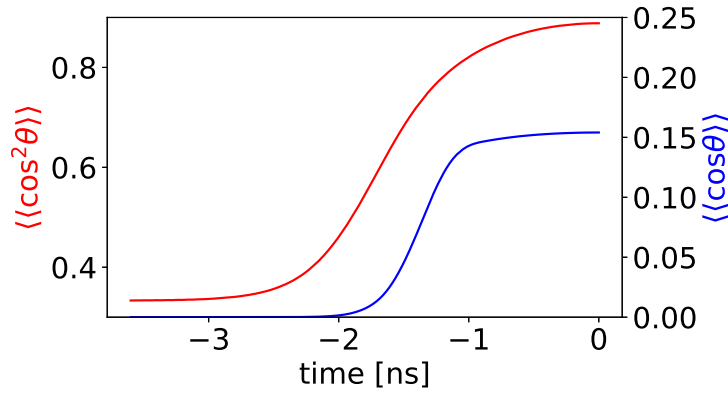
4.3 Increasing the degree of orientation

To demonstrated the advantage of using an elliptically polarized second harmonic pulse in the two-color laser field, time-dependent Schrödinger equations (TDSE) have been solved for three cases:

1. Linearly polarized two-color laser field: The peak intensities are $I_\omega = 3.6 \times 10^{11}$ W/cm² and $I_{2\omega} = 3.9 \times 10^{11}$ W/cm². The simulation result is presented in figure 4.3a.
2. Linearly polarized two-color laser field where the peak intensities are increased 1.7 times compared to those in case 1: $I_\omega = 5.8 \times 10^{11}$ W/cm² and $I_{2\omega} = 6.6 \times 10^{11}$ W/cm². The simulation result is given in figure 4.3b.
3. A combination of a linearly polarized fundamental pulse and an elliptically polarized second harmonic pulse : The intensities along the vertical direction, which is the major axis of the elliptically polarized light, are the same as case 1: $I_\omega = 3.6 \times 10^{11}$ W/cm² and $I_{2\omega} = 3.9 \times 10^{11}$ W/cm², while an extra horizontal component is added along the minor axis of the elliptically polarized second harmonic pulse : $I'_{2\omega} = 3.5 \times 10^{11}$ W/cm². The simulation result for this case is shown in figure 4.4.



(a) $I_\omega = 3.6 \times 10^{11}$ W/cm² and $I_{2\omega} = 3.9 \times 10^{11}$ W/cm².



(b) $I_\omega = 5.8 \times 10^{11}$ W/cm² and $I_{2\omega} = 6.6 \times 10^{11}$ W/cm².

Fig. 4.3: Degrees of alignment $\langle\langle \cos^2 \theta \rangle\rangle$ and orientation $\langle\langle \cos \theta \rangle\rangle$ as a function of time for an all-optical method with a linearly polarized two-color laser field.

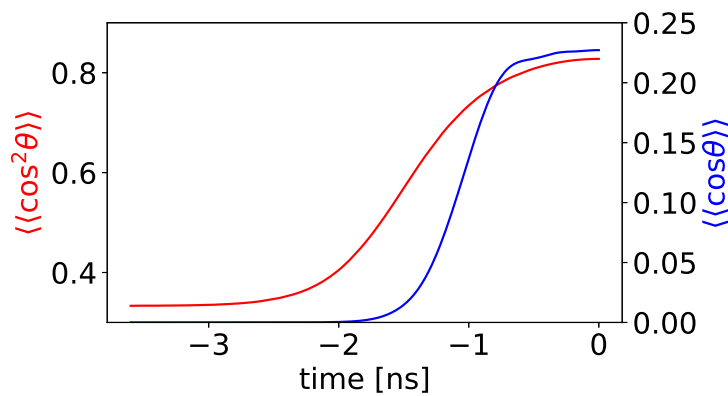


Fig. 4.4: Degrees of alignment $\langle\langle \cos^2 \theta \rangle\rangle$ and orientation $\langle\langle \cos \theta \rangle\rangle$ as a function of time for an all-optical method with a combined linearly and elliptically polarized two-color laser field. The peak intensities are $I_\omega = 3.6 \times 10^{11}$ W/cm², $I_{2\omega} = 3.9 \times 10^{11}$ W/cm², and $I'_{2\omega} = 3.5 \times 10^{11}$ W/cm².

In all three cases, the HWHMs of the fundamental pulse and the second harmonic pulse are $\tau_\omega = 1.2$ ns and $\tau_{2\omega} = 0.9$ ns, respectively. In all the simulations, a thermal average $\langle\langle\cos^2\theta\rangle\rangle$ and $\langle\langle\cos\theta\rangle\rangle$ for an initial rotational temperature $T_{\text{rot}} = 1$ K have been computed. The relative phase difference between the fundamental pulse and the second harmonic pulse is $\Phi = \pi$, which, for OCS molecules, creates a deeper potential at $\theta \sim 0$ and a relatively shallower potential at $\theta \sim \pi$ as explained in figure 4.2.

The degrees of alignment and orientation at $t = 0$ ns, which is at the peaks of the two pulses, are $\langle\langle\cos^2\theta\rangle\rangle = 0.85$ and $\langle\langle\cos\theta\rangle\rangle = 0.173$ in figure 4.3a. If we just increase the intensities of the laser fields by a factor of 1.7, we end up with the values $\langle\langle\cos^2\theta\rangle\rangle = 0.89$ and $\langle\langle\cos\theta\rangle\rangle = 0.154$. Due to the nonadiabaticity of the process, the degree of orientation is indeed getting suppressed while the degree of alignment is increased. The added power is used only to align the molecules, whereas transitions from the shallower potential at $\theta \sim \pi$ to the deeper potential at $\theta \sim 0$ have become more inefficient.

In figure 4.4, where a combined linearly and elliptically two-color laser field is used, the degree of orientation is increased to $\langle\langle\cos\theta\rangle\rangle = 0.227$ while the degree of alignment is reduced to $\langle\langle\cos^2\theta\rangle\rangle = 0.83$. The increase in the intensity compared to the linearly polarized two-color laser field demonstrated in figure 4.3a is along the horizontal direction, where the minor axis of the elliptically polarized second harmonic pulse with a peak intensity of $I'_{2\omega} = 3.3 \times 10^{11}$ W/cm² is applied. The total intensity used in this case is lower than the total intensity used in figure 4.3b. The increased intensity in 4.4 is used to increase the degree of orientation, and suppress the degree of alignment. On the contrary, when the intensity of a linearly polarized two-color laser field is increased, it only improves the degree of alignment and suppresses the degree of orientation. The introduction of an elliptically polarized second harmonic pulse indeed utilizes the increased intensity to efficiently increase the degree of orientation.

4.4 Intensity dependence

The intensity dependence of the degrees of alignment and orientation for OCS and FCN molecules are computed for two different initial rotational temperatures: $T_{\text{rot}} = 0.6$ K (figure 4.5a) and $T_{\text{rot}} = 2$ K (figure 4.5b). Nonadiabatic effects are incorporated in the results by directly solving the time-dependent Schrödinger equation (TDSE). Although the figures are plotted as a function of the intensity of the fundamental pulse I_ω , the intensities of the elliptically polarized second harmonic pulse along the major axis $I_{2\omega}$ and the minor axis $I'_{2\omega}$ are also increased with the ratios: $I_{2\omega} = 1.1I_\omega$ and $I'_{2\omega} = 0.98I_\omega$.

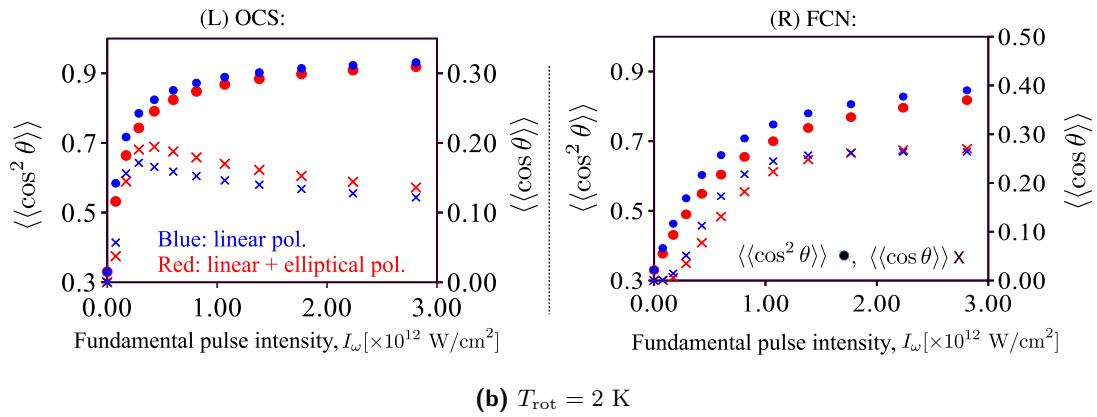
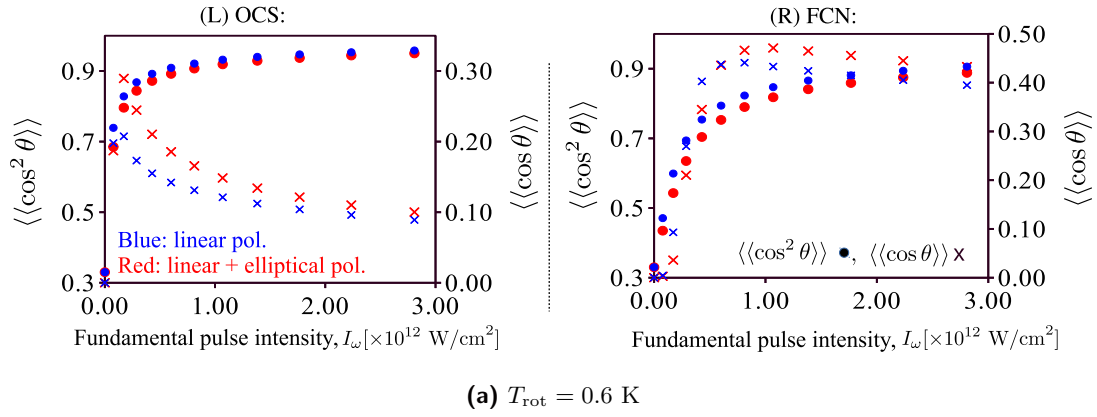


Fig. 4.5: Degrees of alignment $\langle\langle \cos^2 \theta \rangle\rangle$ (dots) and orientation $\langle\langle \cos \theta \rangle\rangle$ (crosses) as a function of the peak laser intensity. The panels in the left column is for OCS molecules and those in the right column represents the results for FCN molecules. Blue color is used to denote the case of a linearly polarized two-color laser field, whereas red is used to denote an all-optical technique with a combined linearly and elliptically polarized laser field.

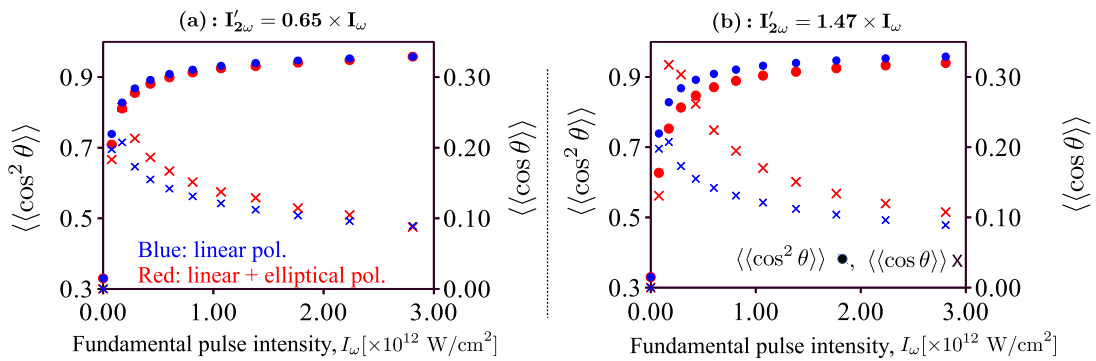


Fig. 4.6: Degrees of alignment $\langle\langle \cos^2 \theta \rangle\rangle$ (dots) and orientation $\langle\langle \cos \theta \rangle\rangle$ (crosses) of OCS molecules as a function of the peak laser intensity where the horizontal component $I'_{2\omega}$ of the elliptically polarized second harmonic pulse is (a) lower or (b) higher than that of figure 4.5a. The initial rotational temperature is $T_{\text{rot}} = 0.6$ K.

In the simulation results, blue color is used to denote results when a usual linearly polarized two-color laser field is used for molecular orientation and red color is used for a combined linearly polarized and elliptically polarized two-color laser field. In figure 4.5a, the red crosses exceed the blue crosses, showing that the introduction of an elliptically polarized second harmonic field increases the degree of orientation. At the same time, the red dots are slightly lowered than the blue dots, indicating that molecular alignment is suppressed by the introduction of the horizontal component of the elliptical polarization.

The influence of the elliptically polarized second harmonic pulse is more pronounced for OCS molecules compared to that of FCN molecules. As given in table 2.2, the ratio of the asymmetry in potential to the depth of the total interaction potential for an FCN molecule (9.8×10^{-3}) is higher than that for an OCS molecule (3.3×10^{-3}). Therefore, the effect of an elliptically polarized second harmonic pulse is limitative for molecules such as FCN for which the interaction through the hyperpolarizability anisotropy is relatively more effective. Nevertheless, molecules with a larger hyperpolarizability anisotropy such as FCN are not ordinary, and for most molecules such as OCS, the asymmetric potential is smaller by more than two orders of magnitude than the depth of the total interaction potential mainly formed due to the polarizability anisotropy. In these situations, as demonstrated in figure 4.5a, applying a combined linearly and elliptically polarized two-color laser field effectively increases the degree of orientation.

For higher initial rotational temperatures such as $T_{\text{rot}} = 2$ K as depicted in figure 4.5b, the increase in the degree of orientation for OCS molecules is limited. For FCN molecules, the elliptically polarized second harmonic pulse rather decreases the degree of orientation. However, molecules like FCN with a relatively stronger hyperpolarizability interaction are not ordinary. In general, using a combined linearly and elliptically polarized two-color laser field effectively increases the degree of orientation for most common molecules such as OCS when the initial rotational temperatures are sufficiently low.

The results presented in figure 4.6 are important. Here, we have changed the intensity $I'_{2\omega}$ of the elliptically polarized second harmonic laser pulse along the horizontal or X axis. Figure 4.6 (a) is for a slightly lower intensity ($I'_{2\omega} = 0.65I_{\omega}$) and figure 4.6 (b) is for a slightly higher intensity ($I'_{2\omega} = 1.47I_{\omega}$). The initial rotational temperature is $T_{\text{rot}} = 0.6$ K in both cases. Comparing with the left image of figure 4.5a, we see that the increase in the degree of orientation $\langle\langle\cos\theta\rangle\rangle$ is lower in figure 4.6 (a) and enhanced in figure 4.6 (b). By appropriately tuning the intensity of the laser field along the horizontal axis of the elliptically polarized second harmonic pulse, we can increase the degree of orientation $\langle\langle\cos\theta\rangle\rangle$ effectively. The response of $\langle\langle\cos\theta\rangle\rangle$ as a function of the intensity of the laser field under a linearly polarized two-color laser field is governed by the parameters unique to the molecule itself: the

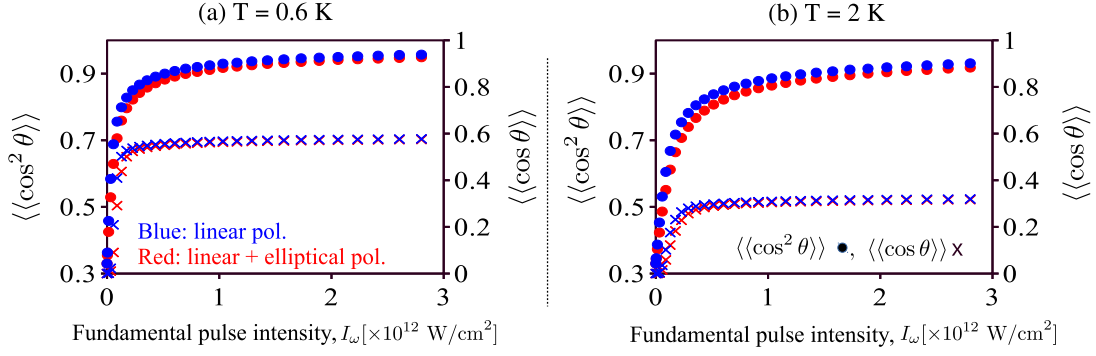


Fig. 4.7: Degrees of alignment $\langle\langle \cos^2 \theta \rangle\rangle$ (dots) and orientation $\langle\langle \cos \theta \rangle\rangle$ (crosses) of OCS molecules as a function of peak laser intensity when the initial rotational temperatures are (a) $T_{\text{rot}} = 0.6$ K and (b) $T_{\text{rot}} = 2$ K. The results are computed under the assumption of adiabatic approximation.

rotational constant B , the polarizability and the hyperpolarizability anisotropies. However, by changing the intensity along the horizontal direction of an elliptically polarized second harmonic pulse, it is possible to control the degree of orientation - laser intensity curve. By applying a stronger field along the horizontal direction, it is possible to increase $\langle\langle \cos \theta \rangle\rangle$.

4.5 The role of nonadiabaticity

So far, we have discussed the solutions of a TDSE, considering nonadiabatic effects in an all-optical molecular orientation method. What would happen if we solve similar problems using the adiabatic approximation method? Simulated results of such cases assuming the adiabatic dynamics are presented in figure 4.7. The sample molecule used in these calculations is OCS, and the initial rotational temperatures are (a) $T_{\text{rot}} = 0.6$ K and (b) $T_{\text{rot}} = 2$ K. From these figures, one can see that the introduction of an elliptically polarized second harmonic pulse does not increase the degree of orientation when the adiabatic approximation is employed. Instead, it suppresses both the degrees of alignment $\langle\langle \cos^2 \theta \rangle\rangle$ and orientation $\langle\langle \cos \theta \rangle\rangle$. This result means that a combination of linearly and elliptically polarized two-color laser fields is effective when molecular orientation dynamics is nonadiabatic. As shown in figure 3.18 and 3.20, molecular orientation with laser pulses as long as ~ 12 ns (FWHM) is nonadiabatic. Hence, the application of an elliptically polarized second harmonic pulse in all-optical molecular orientation technique is of practical importance.

All the effects presented in this chapter might also be achieved with an additional linearly polarized laser pulse with a random phase along the horizontal direction. Theoretically, this is a valid argument. But, in practice, introducing another laser

pulse into a two-color laser field will only make the experiment more complex and time-consuming. All-optical molecular orientation requires precise overlap of all the pump and probe laser pulses. Moreover, all the optical components are designed to be used under a wavelength range constraints. Under these constraints, adding another laser with a random phase into an experiment which already has three different wavelengths (800 nm for the probe pulse, 1064 nm and 532 nm for the two-color pump laser field) will only increase the complexity. Just changing the polarization of an already existing second harmonic pulse is a much simpler and more effective approach.

4.6 Three-dimensional molecular orientation

Three-dimensional alignment with an elliptically polarized laser field has been theoretically proposed and experimentally demonstrated [23, 28, 29, 32, 219, 220]. Adding an electrostatic field to an elliptically polarized pump laser field achieves three-dimensional molecular orientation [43, 45, 75, 221–223]. All optical three-dimensional molecular alignment and orientation have been experimentally observed by applying a linearly polarized two-color laser field, where the polarization directions of the fundamental pulse and the second harmonic pulse are crossed [31, 69, 70, 224]. In this section, we will explore whether a combined linearly and elliptically polarized two-color laser field can be used as an effective all-optical three-dimensional molecular orientation technique.

4.6.1 Nonlinear interaction through polarizability and hyperpolarizability anisotropies

We will consider asymmetric top molecules such as iodobenzene (C_6H_5I) which belong to the point group C_{2v} [88, 89, 225, 226]. The interaction potential of an asymmetric top molecule (iodobenzene) and a combined linearly and elliptically polarized two-color laser field as defined in Eq. (4.1) is given by the following expression:

$$\begin{aligned} \hat{H}_i = & -\frac{1}{4}\alpha_{zy} \left[\cos^2 \phi \sin^2 \theta E_{2\omega}'^2(t) + \cos^2 \theta \{E_{\omega}^2(t) + E_{2\omega}^2(t)\} \right] \\ & -\frac{1}{4}\alpha_{xy} \left[(\cos \phi \cos \theta \cos \chi - \sin \phi \sin \chi)^2 E_{2\omega}'^2(t) + \cos^2 \chi \sin^2 \theta \{E_{\omega}^2(t) + E_{2\omega}^2(t)\} \right] \\ & \pm \frac{3}{8} \{ \beta_{zxx} \cos^2 \chi + \beta_{zyy} \sin^2 \chi \} \cos \theta \sin^2 \theta E_{\omega}^2(t) E_{2\omega}(t) \\ & \pm \frac{1}{8} \beta_{zzz} \cos^3 \theta E_{\omega}^2(t) E_{2\omega}(t), \end{aligned} \quad (4.8)$$

where the phase difference between the two wavelengths is $\Phi = \pi$ or 0 , $\alpha_{zy} = \alpha_{zz} - \alpha_{yy}$ and $\alpha_{xy} = \alpha_{xx} - \alpha_{yy}$. The body-fixed coordinates x , y , and z are defined

in figure 2.1 (b). The Euler angles (ϕ, θ, χ) as defined in figure 2.2. This interaction potential is derived after taking the average over a laser oscillation period $\frac{2\pi}{\omega}$. The first two terms are due to polarizability anisotropy and the last two terms are from hyperpolarizability interactions. If we ignore the hyperpolarizability anisotropy, we will end up with an interaction potential that only aligns the asymmetric top molecules in a plane defined by the major and the minor axes of the elliptically polarized second harmonic field [32, 219]. The free rotational Hamiltonian \hat{H}_0 is given by Eq. (2.9), which is written here again for clarity:

$$\hat{H}_0 = \frac{B+C}{2} \mathbf{J}^2 + \left(A - \frac{B+C}{2} \right) \hat{J}_a^2 + \frac{B-C}{4} [(\hat{J}^+)^2 - (\hat{J}^-)^2], \quad (4.9)$$

where $\hat{J}^\pm = \hat{J}_b \pm i\hat{J}_c$. To estimate the degree of alignment $\langle\langle \cos^2 \theta \rangle\rangle$ and orientation $\langle\langle \cos \theta \rangle\rangle$, we need to solve the Schrödinger equation of Eq. (2.8). To perform numerical simulations, a wavefunction $|\Psi(t)\rangle$ is expanded in terms of the symmetric top wave functions $|JKM\rangle$ as given by Eq. (2.10). The matrix elements of the free rotational Hamiltonian is given by the following equation [85, 86, 100]:

$$\begin{aligned} & \langle J'K'M' | \hat{H}_0 | JKM \rangle & (4.10) \\ & = \left[\frac{B+C}{2} J(J+1) + \left(A - \frac{B+C}{2} \right) K^2 \right] \delta_{JJ', MM', KK'} \\ & + \frac{B-C}{4} \sqrt{\{J(J+1) - K(K+1)\} \{J(J+1) - (K+1)(K+2)\}} \delta_{JJ', MM', K+2K'} \\ & + \frac{B-C}{4} \sqrt{\{J(J+1) - K(K-1)\} \{J(J+1) - (K-1)(K-2)\}} \delta_{JJ', MM', K-2K'}. \end{aligned}$$

The matrix elements for the interaction potential of Eq. (4.8) are calculated from the following equation [85]:

$$\begin{aligned} & \langle J'K'M' | D_{M_0K_0}^{J_0} | JKM \rangle & (4.11) \\ & = (-1)^{M-K} \sqrt{(2J'+1)(2J+1)} \begin{pmatrix} J & J_0 & J' \\ -M & M_0 & M' \end{pmatrix} \begin{pmatrix} J & J_0 & J' \\ -K & K_0 & K' \end{pmatrix}. \end{aligned}$$

The trigonometric functions of ϕ, θ , and χ in Eq. (4.8) have to be expressed in terms of the rotation matrix or the Wigner D-matrix $D_{MK}^{J*}(\phi, \theta, \chi)$. The Wigner D-matrix representations of these functions are summarized in appendix A.3.

4.6.2 Estimation of the degree of orientation

The degrees of alignment and orientation for iodobenzene molecule have been calculated under the adiabatic approximation. The rotational constants, polarizability and hyperpolarizability components are listed in table 4.1. The rotational constants

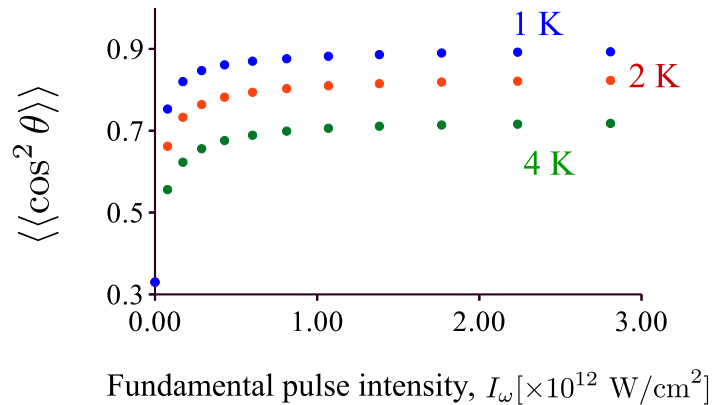


Fig. 4.8: Degrees of alignment $\langle\langle \cos^2 \theta \rangle\rangle$ of iodobenzene molecules as a function of the peak intensity of the fundamental pulse.

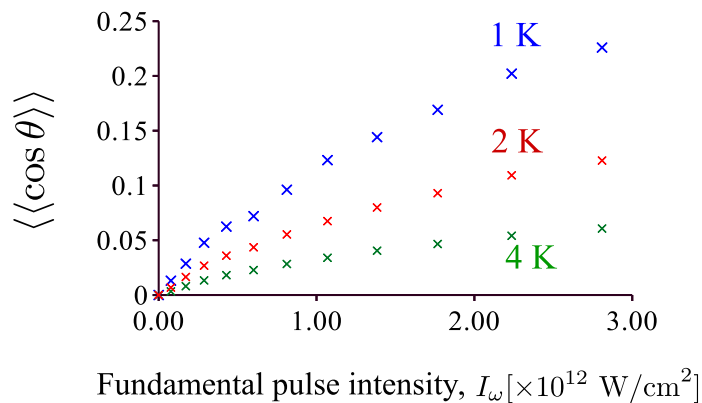


Fig. 4.9: Degrees of orientation $\langle\langle \cos \theta \rangle\rangle$ of iodobenzene molecules as a function of the peak intensity of the fundamental pulse.

meet the condition: $A > B > C$, which is equivalent to the relation $I_a < I_b < I_c$. As shown in figure 2.1 (b), iodobenzene molecules belong to the point group C_{2v} . The C_2 -rotational axis falls on the body-fixed z axis. This axis goes through the iodine atom, which is an order of magnitude heavier than carbon atoms. Hence, the principal moment of inertia axis a falls on the body-fixed z axis. According to the right-hand rule of vector multiplication, the x and y axes correspond to the rotational constants B and C , respectively.

The simulated degrees of alignment $\langle\langle \cos^2 \theta \rangle\rangle$ and orientation $\langle\langle \cos \theta \rangle\rangle$ are plotted as a function of the fundamental pulse peak intensity in figures 4.8 and 4.9 for three initial rotational temperatures: 1 K, 2 K, and 4 K. In these results, the peak intensities of the elliptically polarized second harmonic pulse are also increased as a function of the fundamental pulse peak intensity: $I_{2\omega} = 1.1I_\omega$ and $I'_{2\omega} = 0.98I_\omega$. From figure 4.9, one can see that the degree of orientation $\langle\langle \cos \theta \rangle\rangle \sim 0.2$ at $I_\omega \sim 2 \times 10^{12}$ W/cm 2 . The degree of alignment achieved in this case is $\langle\langle \cos^2 \theta \rangle\rangle \sim$

Tab. 4.1: Rotational constants, polarizability and hyperpolarizability components of an iodobenzene molecule.

	Rotational constants [89, 226] [J]	polarizability [88] [C ² m ² J ⁻¹]	hyperpolarizability [88] [C ³ m ³ J ⁻²]
A	3.76×10^{-24}	$\alpha_{zz} \quad 2.39 \times 10^{-39}$	$\beta_{zzz} \quad 1.44 \times 10^{-50}$
B	4.97×10^{-25}	$\alpha_{xx} \quad 1.63 \times 10^{-39}$	$\beta_{zxx} \quad 3.49 \times 10^{-52}$
C	4.39×10^{-25}	$\alpha_{yy} \quad 1.01 \times 10^{-39}$	$\beta_{zyy} \quad 2.2 \times 10^{-51}$

0.9. The combination of a linearly polarized fundamental pulse and an elliptically polarized second harmonic pulse of a two-color laser field can orient asymmetric top molecules.

Experimentally, three-dimensional molecular orientation with an all-optical method has been observed by applying linearly polarized two-color femtosecond laser fields where the polarization directions of the fundamental pulse and the second harmonic pulse are orthogonal [70]. However, the observed degree of orientation is low: $\langle \cos \theta \rangle \sim \pm 0.06$. In the three-dimensional orientation using linearly polarized two-color laser pulses, the hyperpolarizability interaction potential contains terms that cancel each other, reducing the asymmetry of the potential. In this case, due to the inherent nonadiabaticity of the process, increasing the intensities of the laser pulses enhances the symmetric potential faster compared to the asymmetric potential. Hence, the degree of molecular orientation does not improve.

On the contrary, when a combination of linearly and elliptically polarized laser pulses defined by Eq. 4.1 is applied, the asymmetry in the potential becomes independent of the peak intensity along the minor axis of the elliptically polarized second harmonic laser pulse. This can be understood from the interaction potential of Eq. (4.8), where the corresponding peak electric field $E'_{2\omega}$ does not appear in the hyperpolarizability interaction part. Due to the nonadiabatic nature of an all-optical molecular orientation process, it is possible to weaken the stronger symmetric potential and suppress the degree of alignment by adjusting $E'_{2\omega}$, independently of the asymmetry in the total potential. Similar characteristics are also prevalent in terms of one-dimensional all-optical orientation as given by Eq. (4.4): peak electric field $E'_{2\omega}$ along the minor axis of the elliptically polarized second harmonic pulse does not play a role in the hyperpolarizability interaction potential. Due to this phenomenon, a combination of linearly and elliptically polarized two-color laser fields is expected to achieve higher degrees of orientation, in the realms of both one-dimensional and three-dimensional all-optical molecular orientation techniques.

Conclusion

All-optical molecular orientation with a two-color laser field is a promising field of research. Although the proof-of-principle experiment has undoubtedly proved the validity of this approach [48, 50], realizing strong molecular orientation with this method was difficult [82, 83]. In this chapter, we summarize the core insights gained from this research about the cause of these problems and the solutions that we have applied to cope with them. Furthermore, some concrete suggestions based on the results obtained in this research have been detailed regarding the future advancement and application of this method.

5.1 Summary of results

We have theoretically and experimentally investigated the core issues regarding the realization of stronger molecular orientation with this technique. Experimentally, we have observed stronger degrees of molecular orientation and found that the process is inherently nonadiabatic in our experimental conditions. Furthermore, we have proposed a novel but simple all-optical technique to efficiently utilize the laser power for achieving higher degrees of orientation both in terms of one-dimensional and three-dimensional molecular orientation. These results are discussed in details in the following paragraphs. The core insights gained from this research are summarized as follows:

5.1.1 Observation of stronger all-optical molecular orientation

We have observed stronger molecular orientation by applying the following two strategies:

1. adjusting the relative delay between the fundamental pulse and the second harmonic pulse of a two-color laser field by introducing the Michelson-type delay line in the optical setup, and
2. selecting lower-lying rotational states with a home-built molecular deflector.

The observed degree of molecular orientation is $\langle\langle \cos \theta \rangle\rangle \sim \pm 0.3$, which is an order of magnitude stronger than the degree of orientation obtained in the proof-of-principle experiment [50]. Furthermore, this value is also the strongest molecular orientation directly observed with the Coulomb explosion imaging while appropriately keeping the probe polarization perpendicular to the detection plane.

5.1.2 Experimental evidence of nonadiabaticity in all-optical molecular orientation

Since the FWHM (~ 12 ns) of the applied laser field is a few orders of magnitude longer than the free rotational period of the sample asymmetric molecules (82.24 ps for OCS), molecular orientation dynamics was believed to be adiabatic. If the process is purely adiabatic, we can numerically show that the degree of orientation becomes a monotonically increasing function of the peak intensity of the laser field. However, in our experiments, we have observed that although the degree of orientation first gradually increases with the increase in the peak intensity of the laser pulse, it starts to decrease when the peak laser intensity is too high. Numerical simulations directly solving the time-dependent Schrödinger equation have revealed that this tendency is explained by the nonadiabatic nature of the all-optical molecular orientation technique with a two-color laser field.

5.1.3 All-optical molecular orientation with combined linearly polarized and elliptically polarized two-color laser fields

Since all-optical molecular orientation is an inherently nonadiabatic process with 12-ns laser pulses, merely increasing the peak intensity of the two-color laser field cannot realize stronger molecular orientation. As an alternative solution to this issue, we have proposed a novel all-optical technique for molecular orientation where a linearly polarized fundamental pulse together with an elliptically polarized second harmonic pulse is adopted as the two-color laser field. Due to the nonadiabatic nature of the all-optical molecular orientation method, it is possible to suppress the degree of alignment while increasing the degree of orientation by using an elliptically polarized second harmonic pulse. According to the numerical solution of the time-dependent Schrödinger equation, it is explained that the laser intensity along the minor axis of the elliptically polarized second harmonic pulse can be used to tune the enhancement of the degree of orientation. Furthermore, we have theoretically and numerically demonstrated that this method has the potential of realizing three-dimensional molecular orientation, corresponding to a general method of controlling all the rotational degrees of freedom of asymmetric top molecules.

5.2 Future research challenges

One of the obvious research directions is to experimentally observe all-optical one-dimensional molecular orientation with combined linearly polarized and elliptically polarized two-color laser fields. The experimental setup required to observe this phenomenon is very similar to that of the current method where a linearly polarized

two-color laser pulses are used. One additional necessary optical component is a combination of a half-wave plate and a quarter-wave plate required to create the elliptically polarized second harmonic laser pulse with the major axis of the ellipse parallel to the linearly polarized fundamental pulse.

All-optical molecular orientation technique works well when the peak intensity of the second harmonic pulse is higher than the peak intensity of the fundamental pulse [50, 83]. As the FWHM is generally shorter for the second harmonic pulse, this combination of relative intensity has the effect of alleviating the effect of a preceding rising part of the fundamental pulse. However, one should not forget that we have an additional component of the laser field along the minor axis of the elliptically polarized second harmonic. Although the optimal combination of the peak intensities of the two-wavelengths is unique to each situation such as the sample asymmetric molecules, FWHM of the laser pulses, initial rotational temperature of the gaseous molecules, etc., both the peak intensities along the major (vertical) and the minor (horizontal) axes of the elliptically polarized second harmonic pulse have to be larger than the peak intensity of the linearly polarized fundamental pulse as a rule of thumb. To realize such optimal relative intensities, wavelength selective mirrors or beam splitters may be used to intentionally reduce the otherwise stronger fundamental pulse power.

The same optical setup can be used to realize the three-dimensional orientation of asymmetric top molecules because the two-color laser field for both one-dimensional and three-dimensional molecular orientations is the same in this approach as defined in Eq. (4.1). On the other hand, one may want to take 2D projections of the three-dimensional orientation from two orthogonal directions. In that case, observation strategy with the Coulomb explosion imaging will be different for one-dimensional and three-dimensional molecular orientation methods, but the optical setup will remain the same for both the cases.

The conventional method of realizing three-dimensional molecular orientation is to deploy a two-color laser field where the polarization axes of the linearly polarized fundamental pulse and the second harmonic pulses are crossed [26, 69, 107]. We can perform numerical simulations to compare the effectiveness of this approach with the proposed method where a linearly polarized fundamental pulse and an elliptically polarized second harmonic laser pulse are used. Furthermore, we can estimate the optimal peak intensities of the laser pulses required to realize higher degrees of three-dimensional molecular orientation. To implement these calculations, we need to numerically solve the time-dependent Schrödinger equation where the matrix size is 39711×39711 for $J = 30$ and 91881×91881 for $J = 40$. Since all the quantum numbers J, K and M 's play a role in the dynamics, the matrix size increases with the order $\mathcal{O}(J^3)$. To numerically follow the temporal evolution of such a large

system is a daunting task. Nevertheless, provided that we have access to adequate computing resources, such simulations are not impossible.

Rapidly turning off the two-color laser field at its peak intensity with a plasma shutter technique has the potential of realizing completely field-free all-optical molecular orientation with nanosecond laser pulses [71, 73]. However, since this technique focuses a femtosecond laser pulse onto an ethylene glycol jet sheet to form plasma, the air surrounding the plasma shutter gets filled with vapor and small particles produced from ethylene glycol. They randomly change the refractive index of the optical path around the plasma shutter, resulting in an unstable phase difference between the fundamental pulse and the second harmonic pulse due to chromatic dispersion. One way to avoid this problem is to keep the plasma shutter inside a vacuum chamber and then constantly pump out the residual ions from the created plasma.

The prospects of future research activities related to the advancements and applications of the all-optical molecular orientation technique are limitless. Many interesting tasks lie ahead as open problems to be investigated theoretically and experimentally. We have simply outlined some of the most compelling questions and their possible solutions in details above.

Appendices

A.1 Free rotational period of linear molecules

A linear molecule follows the field-free Schrödinger equation,

$$i\hbar \frac{\partial}{\partial t} |\Psi(t)\rangle = B\mathbf{J}^2 |\Psi(t)\rangle. \quad (\text{A.1})$$

As $\hat{H}_0 = B\mathbf{J}^2$ is independent of time, the solution of Eq. (A.1) can be written analytically. By using spherical harmonics of Eq. (2.12) as basis functions,

$$|\Psi(t)\rangle = \sum_{JM} d_{JM}(t) |JM\rangle. \quad (\text{A.2})$$

Since spherical harmonics are the eigenstates of the squared angular momentum operator \mathbf{J}^2 , and form a complete orthonormal basis set of functions for the angles θ and ϕ [85, 86, 113, 117–119]. Eq. (A.1) can be written as the following system of linear differential equations:

$$\frac{i\hbar}{B} \frac{\partial}{\partial t} d_{JM}(t) = \sum_{J'M'} \langle JM | \mathbf{J}^2 | J'M' \rangle d_{J'M'}(t) = J(J+1) d_{JM}(t), \quad (\text{A.3})$$

which has the analytical solution, [86, 102, 103, 143, 227]:

$$d_{JM}(t) = d_{JM}(0) e^{-i\frac{B}{\hbar} J(J+1)t}. \quad (\text{A.4})$$

The term $e^{-i\frac{B}{\hbar} J(J+1)t}$ has a period of $T_J = \frac{2\pi\hbar}{BJ(J+1)}$, where B is expressed in joule (SI). The ground state has the value $J = 0$, but this state is isotropic under the field free condition. From $J = 1$, the spherical harmonics start to become anisotropic in terms of the angles θ and ϕ . For $J = 1$, the rotational period T_1 is called the free rotational period of the molecule:

$$\tau_{\text{rot}} = \frac{\pi\hbar}{B}. \quad (\text{A.5})$$

Since the factor $\frac{J(J+1)}{2}$ is always integer, the free rotational period τ_{rot} is always an integer multiple of any rotational period T_J . Hence, any linear combination of the states $|JM\rangle$, under the field free condition, will have the same phase factor at

t_1 and $t_2 = t_1 + \tau_{\text{rot}}$. This means that parameters such as $\langle \cos \theta \rangle$, which meet the criterion $f(\theta) = f(\theta + 2\pi)$, evolve with a period of τ_{rot} [76–78]. For some parameters such as $\langle \cos^2 \theta \rangle$ where $f(\theta) = f(\theta + \pi)$, the period of repetition is $\frac{\tau_{\text{rot}}}{2}$ [72, 73, 76, 77]. The rotational constants of OCS and FCN molecules are summarized in table 2.2. We can extend this argument for general planar molecules as well, but we have to be careful in this case because, as shown in Eq. (2.9), the Wigner D-matrices of Eq. (2.10) are not the eigenstates of the field-free Hamiltonian of an asymmetric top molecule.

A.2 Tunneling in a double-well potential

To explain the dynamics of molecular alignment and orientation dynamics, we can refer to the so-called double-well potential model. In figure A.1, a double-well potential is depicted where (a) the two wells are separated, and no transition passage is available; (b) the two potential wells are symmetric, and passage for tunneling is available; and (c) the double-well potential is asymmetric, and transition passage is present. In case (a), when the potential barrier between the two wells is infinitely high and impenetrable, the ground state in each well has the same eigenenergy. Let's assume that the ground state for the right potential well is given by the quasi-classical wave function $\Psi_0(\theta)$. The ground state wave functions localized in the right and left potential wells are denoted by $\Psi_r(\theta)$ and $\Psi_l(\theta)$, respectively. They can be expressed in terms of $\Psi_0(\theta)$ [102]:

$$\begin{aligned}\Psi_r(\theta) &= \Psi_0(\theta), \\ \Psi_l(\theta) &= \Psi_0(-\theta).\end{aligned}\tag{A.6}$$

We can now consider cases where the wells are connected and tunneling between the two wells become possible. Molecular alignment happens when the double-well potential is symmetric, and an asymmetry between the two wells created by electrostatic force or a two-color laser field is responsible for molecular orientation. In the following paragraphs, we discuss these cases in details.

A.2.1 Symmetric double-well potential

The dynamics of molecular alignment can be explained with the symmetric double-well potential model. When a passage for tunneling between two symmetric wells is created as shown in figure A.1 (b), the ground state energy is shifted from E_0 . As the double well potential is symmetric upon inversion along the θ -axis, the symmetric

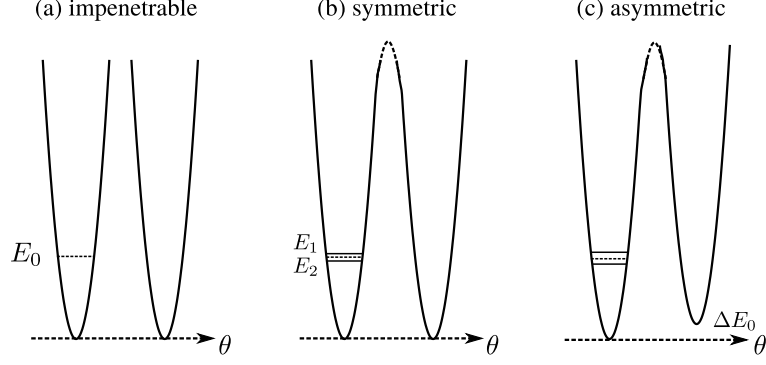


Fig. A.1: Tunneling in a double well potential: (a) impenetrable potential with infinite barrier, (b) symmetric potential with transition passage, (c) asymmetric potential with transition passage

and antisymmetric combinations of $\Psi_0(\theta)$ and $\Psi_0(-\theta)$ are the ground state and the first excited state of the total Hamiltonian, respectively [102]:

$$\begin{aligned}\Psi_1(\theta) &= \frac{1}{\sqrt{2}} [\Psi_0(\theta) + \Psi_0(-\theta)] = \frac{1}{\sqrt{2}} [\Psi_r(\theta) + \Psi_l(\theta)], \\ \Psi_2(\theta) &= \frac{1}{\sqrt{2}} [\Psi_0(\theta) - \Psi_0(-\theta)] = \frac{1}{\sqrt{2}} [\Psi_r(\theta) - \Psi_l(\theta)].\end{aligned}\quad (\text{A.7})$$

The wave functions $\Psi_1(\theta)$ and $\Psi_2(\theta)$ are the eigenstates of the parity operator $P : \theta \mapsto -\theta$ as well. The time evolution of these first two eigenstates can be written as the following:

$$\begin{aligned}\Psi_1(\theta, t) &= \Psi_1(\theta) e^{-i\frac{E_1}{\hbar}t}, \\ \Psi_2(\theta, t) &= \Psi_2(\theta) e^{-i\frac{E_2}{\hbar}t},\end{aligned}\quad (\text{A.8})$$

where the eigenenergies of the ground state and the first excited state are given by E_1 and E_2 , respectively. Let us now consider a state which is a linear combination of these two states:

$$\begin{aligned}\Phi(x, t) &= C_1 \Psi_1(\theta, t) + C_2 \Psi_2(\theta, t) \\ &= C_1 \Psi_1(\theta) e^{-i\frac{E_1}{\hbar}t} + C_2 \Psi_2(\theta) e^{-i\frac{E_2}{\hbar}t} \\ &= e^{-i\frac{E_1}{\hbar}t} \left[C_1 \Psi_1(\theta) + C_2 \Psi_2(\theta) e^{-i\frac{E_2-E_1}{\hbar}t} \right].\end{aligned}\quad (\text{A.9})$$

We can see that if the the particle in one of the eigenstates, then either $C_1 = 0$ or $C_2 = 0$, and the particle remains in that state forever. However, when the dynamics is nonadiabatic, the wave function does not remain an eigenstate of the total Hamiltonian. Rather, it is a linear combination of the eigenstates. The time

evolution of the probability density of such a combination of the eigenstates is given by,

$$\Phi^* \Phi = C_1^* C_1 \Psi_1^* \Psi_1 + C_2^* C_2 \Psi_2^* \Psi_2 + C_1 C_2^* \Psi_1 \Psi_2^* e^{i\left(\frac{E_2-E_1}{\hbar}\right)t} + C_1^* C_2 \Psi_1^* \Psi_2 e^{-i\left(\frac{E_2-E_1}{\hbar}\right)t}. \quad (\text{A.10})$$

The above probability density oscillates with a frequency $\omega = \frac{E_2-E_1}{\hbar}$. The period of this oscillation is a measure of the characteristic time $\tau_{\text{tun.}}$ for tunneling from one well to another:

$$\tau_{\text{tun.}} = \frac{2\pi\hbar}{|E_1 - E_2|}. \quad (\text{A.11})$$

For example, when $C_1 = \frac{1}{\sqrt{2}}$ and $C_2 = \frac{1}{\sqrt{2}}$, for $\frac{E_2-E_1}{\hbar} = 0, \pi$, $\Phi^* \Phi = |\Psi_1 + \Psi_2|^2 = \Psi_r^* \Psi_r$, and for $\frac{E_2-E_1}{\hbar} = \pm\pi$, $\Phi^* \Phi = |\Psi_1 - \Psi_2|^2 = \Psi_l^* \Psi_l$. Since the wave functions Ψ_r and Ψ_l are localized in the right and the left well, Φ oscillates between the two wells.

A.2.2 Asymmetric double-well potential

To describe the dynamics of molecular orientation, we need to consider an asymmetric double-well potential model. Since there is an asymmetry between the left and the right well as shown in figure A.1 (c), the potential is not invariant upon an inversion along the θ -axis. Hence, the wave functions given by the equations (A.7) are no longer the eigenstates of the asymmetric double well. To get an estimate of the characteristic tunneling time for this arrangement, let us assume that the base of the wells are slightly shifted and the barrier between them is impenetrable. The energy difference between the bases of the left and the right well is ΔV_0 . Since the wells are not connected yet, we can assume that the ground state in the right potential well will be:

$$\Psi_r(\theta, t) = \Psi_r(\theta) e^{-i\frac{E_0+\Delta V_0}{\hbar}t} = \Psi_0(\theta) e^{-i\frac{E_0+\Delta V_0}{\hbar}t}, \quad (\text{A.12})$$

provided that we express the ground state of the left well with the following wave function:

$$\Psi_l(\theta, t) = \Psi_l(\theta) e^{-i\frac{E_0}{\hbar}t} = \Psi_0(-\theta) e^{-i\frac{E_0}{\hbar}t}. \quad (\text{A.13})$$

When the asymmetric double-well potential is so deep that the barrier between them is nearly impenetrable: $E_0 \ll V_H$, where E_0 is the ground state energy and V_H is the height of the potential barrier, the energy difference between the first two eigenstates are governed by the asymmetry in the total potential denoted as ΔV_0 . In this situation, since the energy of $\Psi_r(\theta)$ is higher than that of $\Psi_l(\theta)$, we can expect the ground state and the first excited state after the potentials are connected to be

approximated by $\Psi_l(\theta)$ and $\Psi_r(\theta)$, respectively. Considering a linear combination of these two states given by,

$$\Phi(\theta, t) = C_r \Psi_r(\theta, t) + C_l \Psi_l(\theta, t), \quad (\text{A.14})$$

and repeating the arguments of equations (A.9) and (A.10), we can approximately derive the characteristic time required for tunneling:

$$\tau_{\text{tun.}} = \frac{2\pi\hbar}{|\Delta V_0|}. \quad (\text{A.15})$$

A.3 Expressing interaction Hamiltonian terms with spherical harmonics

The nonlinear interaction potential as given by Eq. (2.15) is expressed with trigonometric functions such as $\cos \theta$, $\cos^2 \theta$, $\cos^3 \theta$ etc. As we solve the Schrödinger equation using the spherical harmonics as the basis functions, these terms also need to be expressed in terms of the spherical harmonics:

$$\cos \theta = 2\sqrt{\frac{\pi}{3}} Y_{10}, \quad (\text{A.16})$$

$$\cos^2 \theta = \frac{1}{3} + \frac{4}{3}\sqrt{\frac{\pi}{5}} Y_{20}, \quad (\text{A.17})$$

$$\cos^3 \theta = \frac{4}{5}\sqrt{\frac{\pi}{7}} Y_{30} + \frac{6}{5}\sqrt{\frac{\pi}{3}} Y_{10}, \quad (\text{A.18})$$

$$\cos^2 \phi \sin^2 \theta = \frac{1}{3} - \frac{2}{3}\sqrt{\frac{\pi}{5}} Y_{20} + \sqrt{\frac{2\pi}{15}} Y_{22} + \sqrt{\frac{2\pi}{15}} Y_{2-2}. \quad (\text{A.19})$$

These expressions are then used in Eq. (2.19) to find out the appropriate matrix elements of the interaction potential.

In case of three-dimensional orientation of asymmetric top molecules such as iodobenzene, we need to use the symmetric top wave functions defined by Eq (2.10) as the basis functions. The terms in the interaction potential given by Eq. (4.8) are expressed with the Wigner D-matrices or the rotational matrices $D_{MK}^{J*}(\phi, \theta, \chi)$ in the following manner:

$$\cos \theta = D_{00}^1, \quad (\text{A.20})$$

$$\cos^2 \theta = \frac{1}{3} + \frac{2}{3} D_{00}^2, \quad (\text{A.21})$$

$$\cos^3 \theta = \frac{2}{5}D_{00}^3 + \frac{3}{5}D_{00}^1, \quad (\text{A.22})$$

$$\cos^2 \phi \sin^2 \theta = \frac{1}{3} - \frac{1}{3}D_{00}^2 + \frac{1}{\sqrt{6}}D_{20}^2 + \frac{1}{\sqrt{6}}D_{-20}^2, \quad (\text{A.23})$$

$$\cos^2 \chi \sin^2 \theta = \frac{1}{3} - \frac{1}{3}D_{00}^2 + \frac{1}{\sqrt{6}}D_{02}^2 + \frac{1}{\sqrt{6}}D_{0-2}^2, \quad (\text{A.24})$$

$$\begin{aligned} (\cos \phi \cos \theta \cos \chi - \sin \phi \sin \chi)^2 = & \frac{1}{3} + \frac{1}{6}D_{00}^2 & (\text{A.25}) \\ & + \frac{1}{4}D_{-2-2}^2 + \frac{1}{4}D_{22}^2 + \frac{1}{4}D_{2-2}^2 + \frac{1}{4}D_{-22}^2 \\ & - \frac{1}{8}D_{-20}^2 - \frac{1}{8}D_{0-2}^2 - \frac{1}{8}D_{20}^2 - \frac{1}{8}D_{02}^2, \end{aligned}$$

$$\sin^2 \theta \cos \theta \cos^2 \chi = \frac{1}{5}D_{00}^1 - \frac{1}{5}D_{00}^3 + \frac{1}{\sqrt{30}}D_{0-2}^3 + \frac{1}{\sqrt{30}}D_{02}^3, \quad (\text{A.26})$$

$$\sin^2 \theta \cos \theta \sin^2 \chi = \frac{1}{5}D_{00}^1 - \frac{1}{5}D_{00}^3 - \frac{1}{\sqrt{30}}D_{0-2}^3 - \frac{1}{\sqrt{30}}D_{02}^3. \quad (\text{A.27})$$

These relations are best derived by using the equations $\cos x = \frac{1}{2}(e^{ix} + e^{-ix})$ and $\sin x = \frac{1}{2i}(e^{ix} - e^{-ix})$ where $x = \phi, \theta$, or χ .

A.4 Electric field strength of a Gaussian beam

Let us assume that P watt is the power of a laser beam measured by a commercial power meter. P is the average energy per second. The number of pulse per second in the laser beam per second is defined as the repetition rate R . Hence, the average energy per pulse \bar{U} is given by the following expression:

$$\bar{U} = \frac{P}{R} \text{ [J]}. \quad (\text{A.28})$$

The intensity of a laser pulse at a position (x, y) and at time t is given as follows:

$$I(x, y, t) = I_0 e^{-\frac{2x^2}{a^2}} \times e^{-\frac{2y^2}{b^2}} \times e^{-\frac{4t^2 \ln 2}{\tau^2}} \text{ [W/m}^2\text{]}. \quad (\text{A.29})$$

Here, I_0 is the peak intensity and the (x, y) plane is a cross section profile of the Gaussian laser beam propagating toward the z axis. The parameter a, b are used to describe points $(x, y) = (a, b)$ where the intensity is decreased to $\frac{1}{e^2}$ times the maximum intensity. The parameter τ is called the Full Width Half Maximum (FWHM) because, at $t = \frac{\tau}{2}$, the intensity is reduced to half the maximum intensity.

If we integrate the profile in Eq. (A.29), we can find the the average energy per pulse, \bar{U} as follows [51]:

$$\begin{aligned}\bar{U} &= \int_{-\infty}^{\infty} \int_{-\infty}^{\infty} \int_{-\infty}^{\infty} I_0 e^{-\frac{2x^2}{a^2}} \times e^{-\frac{2y^2}{b^2}} \times e^{-\frac{4t^2 \ln 2}{\tau^2}} dx dy dt \\ &= I_0 \frac{\pi ab}{2} \frac{\sqrt{\pi}}{2\sqrt{\ln 2}} \tau \quad [\text{J}].\end{aligned}\quad (\text{A.30})$$

We can measure the spatial beam profile along the (x, y) plane with a beam profiler to estimate the parameters a and b . τ can be measured by observing the laser pulse with a fast photo diode. Since we have already known the average energy per pulse \bar{U} , we can now calculate the peak laser intensity I_0 in our experiments. Although this convention is widely used in measuring important parameters of a Gaussian laser beam, we should keep in mind that this is a rather simplified expression. Generally, there is a coupling between the space and time parameters [228, 229].

To simulate molecular orientation, we use the interaction of nonlinear induced polarization in sample molecules by an applied laser electric field. To find the peak electric field from the peak laser intensity, we use the idea of Poynting vector [230]. The average intensity of an electromagnetic wave is given by,

$$\bar{I} = \frac{1}{2} \text{Re} [\mathbf{E} \times \mathbf{H}^*] \quad [\text{W/m}^2], \quad (\text{A.31})$$

where \mathbf{E} is the electric field and \mathbf{H} is the magnetic field. If we assume planar waves such that $\mathbf{E} = E\hat{x}$ and $\mathbf{H} = H\hat{y}$, then the wave propagates along the \hat{z} axis. The time-averaged Poynting vector in this case is given by,

$$\bar{I} = \frac{E^2}{2|\eta|} \hat{z} = \frac{1}{2} c\epsilon E^2 \hat{z} \quad [\text{W/m}^2], \quad (\text{A.32})$$

where c and ϵ are the speed of light and the electric permittivity of the medium. In our calculation, we use the following equation to calculate the peak electric field E_0 due to the peak laser intensity I_0 :

$$I_0 = \frac{1}{2} c_0 \epsilon_0 E_0^2 \quad [\text{W/m}^2]. \quad (\text{A.33})$$

The interaction of samples molecule with the laser pulse takes place inside a vacuum chamber, hence we have used the values $c_0 = 299,792,458$ m/s and $\epsilon_0 = 8.854 \times 10^{-12}$ F/m. The peak intensity of the fundamental pulse (1064 nm) in our experiment is around 8×10^{11} W/cm². According to Eq. (A.33), this corresponds to an electric field of the strength 2.5×10^9 V/m.

A.5 Unit conversion table for molecular polarizability and hyperpolarizability

In the literature, molecular polarizability and hyperpolarizability anisotropies are reported in different units. The following conversion table is convenient for relating different unit systems.

Tab. A.1: Unit conversion table for molecular polarizability and hyper polarizability. Reproduced from [231]. [a.u.: atomic units, SI: international system units, esu: electrostatic units.]

parameter	esu	SI	a.u.
α	1 cm^3	$1.113 \times 10^{-16} \text{ C}^2\text{m}^2\text{J}^{-1}$	6.748×10^{24}
β	$1 \text{ cm}^5\text{statC}^{-1}$	$3.711 \times 10^{-21} \text{ C}^3\text{m}^3\text{J}^{-2}$	1.157×10^{32}
γ	$1 \text{ cm}^7\text{statC}^{-2}$	$1.238 \times 10^{-25} \text{ C}^4\text{m}^4\text{J}^{-3}$	1.985×10^{39}

Bibliography

- [1]J. Yang, V. Makhija, V. Kumarappan, and M. Centurion, “Reconstruction of three-dimensional molecular structure from diffraction of laser-aligned molecules,” *Structural Dynamics* **1**, 044101 (2014).
- [2]J. Glowonia, A Natan, J. Cryan, R Hartsock, M Kozina, M. Minitti, S Nelson, J Robinson, T Sato, T van Driel, et al., “Self-referenced coherent diffraction X-ray movie of Ångstrom-and femtosecond-scale atomic motion,” *Physical Review Letters* **117**, 153003 (2016).
- [3]J. Xu, C. I. Blaga, P. Agostini, and L. F. DiMauro, “Time-resolved molecular imaging,” *Journal of Physics B: Atomic, Molecular and Optical Physics* **49**, 112001 (2016).
- [4]K. Nakajima, T. Teramoto, H. Akagi, T. Fujikawa, T. Majima, S. Minemoto, K. Ogawa, H. Sakai, T. Togashi, K. Tono, et al., “Photoelectron diffraction from laser-aligned molecules with x-ray free-electron laser pulses,” *Scientific Reports* **5**, 14065 (2015).
- [5]S. Minemoto, T. Teramoto, H. Akagi, T. Fujikawa, T. Majima, K. Nakajima, K. Niki, S. Owada, H. Sakai, T. Togashi, et al., “Structure determination of molecules in an alignment laser field by femtosecond photoelectron diffraction using an X-ray free-electron laser,” *Scientific Reports* **6**, 38654 (2016).
- [6]S. Tsuru, T. Sako, T. Fujikawa, and A. Yagishita, “Theory of time-resolved x-ray photoelectron diffraction from transient conformational molecules,” *Phys. Rev. A* **95**, 043404 (2017).
- [7]S. Tsuru, T. Fujikawa, M. Stener, P. Decleva, and A. Yagishita, “Theoretical study of ultrafast x-ray photoelectron diffraction from molecules undergoing photodissociation,” *The Journal of Chemical Physics* **148**, 124101 (2018).
- [8]J. Itatani, J. Levesque, D. Zeidler, H. Niikura, H. Pépin, J.-C. Kieffer, P. B. Corkum, and D. M. Villeneuve, “Tomographic imaging of molecular orbitals,” *Nature (London)* **432**, 867 (2004).
- [9]T. Kanai, S. Minemoto, and H. Sakai, “Quantum interference during high-order harmonic generation from aligned molecules,” *Nature (London)* **435**, 470 (2005).

- [10]J. P. Marangos, “Ultrafast science: molecular structure in an instant,” *Nature (London)* **435**, 435 (2005).
- [11]T. Suzuki, S. Minemoto, T. Kanai, and H. Sakai, “Optimal control of multiphoton ionization processes in aligned I_2 molecules with time-dependent polarization pulses,” *Physical Review Letters* **92**, 133005 (2004).
- [12]Y. Silberberg, “Ultrafast physics: quantum control with a twist,” *Nature (London)* **430**, 624 (2004).
- [13]S. Minemoto and H. Sakai, “Measuring polarizability anisotropies of rare gas diatomic molecules by laser-induced molecular alignment technique,” *The Journal of Chemical Physics* **134**, 214305 (2011).
- [14]M. G. Reuter, M. A. Ratner, and T. Seideman, “Laser alignment as a route to ultrafast control of electron transport through junctions,” *Physical Review A* **86**, 013426 (2012).
- [15]I. Tutunnikov, E. Gershnel, S. Gold, and I. S. Averbukh, “Selective Orientation of Chiral Molecules by Laser Fields with Twisted Polarization,” *The journal of physical chemistry letters* **9**, 1105 (2018).
- [16]R. Kafri, O. Markovitch, and D. Lancet, “Spontaneous chiral symmetry breaking in early molecular networks,” *Biology Direct* **5**, 38 (2010).
- [17]B. Friedrich and D. R. Herschbach, “Spatial orientation of molecules in strong electric fields and evidence for pendular states,” *Nature (London)* **353**, 412 (1991).
- [18]C. Qin, Y. Liu, X. Zhang, and T. Gerber, “Phase-dependent field-free molecular alignment and orientation,” *Phys. Rev. A* **90**, 053429 (2014).
- [19]C. Qin, Y. Liu, X. Zhang, and Y. Liu, “The physical mechanism of molecular alignment and orientation by a femtosecond two-color laser pulse,” *The European Physical Journal D* **68**, 108 (2014).
- [20]B. Friedrich and D. Herschbach, “Alignment and trapping of molecules in intense laser fields,” *Physical Review Letters* **74**, 4623 (1995).
- [21]B. Friedrich and D. Herschbach, “Polarization of molecules induced by intense nonresonant laser fields,” *The Journal of Physical Chemistry* **99**, 15686 (1995).
- [22]J. Ortigoso, M. Rodriguez, M. Gupta, and B. Friedrich, “Time evolution of pendular states created by the interaction of molecular polarizability with a pulsed nonresonant laser field,” *The Journal of Chemical Physics* **110**, 3870 (1999).
- [23]J. J. Larsen, H. Sakai, C. P. Safvan, I. Wendt-Larsen, and H. Stapelfeldt, “Aligning molecules with intense nonresonant laser fields,” *The Journal of Chemical Physics* **111**, 7774 (1999).

- [24]H. Stapelfeldt, E. Constant, H. Sakai, and P. B. Corkum, “Time-resolved Coulomb explosion imaging: A method to measure structure and dynamics of molecular nuclear wave packets,” *Phys. Rev. A* **58**, 426 (1998).
- [25]S. Luo, R. Zhu, L. He, W. Hu, X. Li, P. Ma, C. Wang, F. Liu, W. G. Roeterdink, S. Stolte, and D. Ding, “Nonadiabatic laser-induced orientation and alignment of rotational-state-selected CH₃Br molecules,” *Phys. Rev. A* **91**, 053408 (2015).
- [26]K. F. Lee, I. V. Litvinyuk, P. W. Dooley, M. Spanner, D. M. Villeneuve, and P. B. Corkum, “Two-pulse alignment of molecules,” *Journal of Physics B: Atomic, Molecular and Optical Physics* **37**, L43 (2004).
- [27]M. Z. Hoque, M. Lapert, E. Hertz, F. Billard, D. Sugny, B. Lavorel, and O. Faucher, “Observation of laser-induced field-free permanent planar alignment of molecules,” *Phys. Rev. A* **84**, 013409 (2011).
- [28]J. Larsen, “Laser induced alignment of neutral molecules,” PhD thesis (Aarhus University, 2000).
- [29]J. J. Larsen, K. Hald, N. Bjerre, H. Stapelfeldt, and T. Seideman, “Three dimensional alignment of molecules using elliptically polarized laser fields,” *Physical Review Letters* **85**, 2470 (2000).
- [30]H. Stapelfeldt and T. Seideman, “Colloquium: Aligning molecules with strong laser pulses,” *Rev. Mod. Phys.* **75**, 543 (2003).
- [31]K. F. Lee, D. M. Villeneuve, P. B. Corkum, A. Stolow, and J. G. Underwood, “Field-Free Three-Dimensional Alignment of Polyatomic Molecules,” *Phys. Rev. Lett.* **97**, 173001 (2006).
- [32]M. Artamonov and T. Seideman, “Theory of three-dimensional alignment by intense laser pulses,” *The Journal of Chemical Physics* **128**, 154313 (2008).
- [33]S. S. Viftrup, V. Kumarappan, L. Holmegaard, C. Z. Bisgaard, H. Stapelfeldt, M. Artamonov, E. Hamilton, and T. Seideman, “Controlling the rotation of asymmetric top molecules by the combination of a long and a short laser pulse,” *Physical Review A* **79**, 023404 (2009).
- [34]M. Artamonov and T. Seideman, “Three-dimensional laser alignment of polyatomic molecular ensembles,” *Molecular Physics* **110**, 885 (2012).
- [35]B. Friedrich and D. Herschbach, “Enhanced orientation of polar molecules by combined electrostatic and nonresonant induced dipole forces,” *The Journal of Chemical Physics* **111**, 6157 (1999).
- [36]B. Friedrich, D. P. Pullman, and D. R. Herschbach, “Alignment and orientation of rotationally cool molecules,” *The Journal of Physical Chemistry* **95**, 8118 (1991).
- [37]B. Friedrich and Herschbach, “Manipulating Molecules via Combined Static and Laser Fields,” *The Journal of Physical Chemistry A* **103**, 10280 (1999).

- [38]L. Cai, J. Marango, and B. Friedrich, “Time-Dependent Alignment and Orientation of Molecules in Combined Electrostatic and Pulsed Nonresonant Laser Fields,” *Phys. Rev. Lett.* **86**, 775 (2001).
- [39]E. Gershnel, I. S. Averbukh, and R. J. Gordon, “Enhanced molecular orientation induced by molecular antialignment,” *Physical Review A* **74**, 053414 (2006).
- [40]S. Luo, W. Hu, J. Yu, R. Zhu, L. He, X. Li, P. Ma, C. Wang, F. Liu, W. G. Roeterdink, S. Stolte, and D. Ding, “Rotational Dynamics of Quantum State-Selected Symmetric-Top Molecules in Nonresonant Femtosecond Laser Fields,” *The Journal of Physical Chemistry A* **121**, 777 (2017).
- [41]S. Minemoto, H. Nanjo, H. Tanji, T. Suzuki, and H. Sakai, “Observation of molecular orientation by the combination of electrostatic and nonresonant, pulsed laser fields,” *The Journal of Chemical Physics* **118**, 4052 (2003).
- [42]H. Sakai, S. Minemoto, H. Nanjo, H. Tanji, and T. Suzuki, “Controlling the Orientation of Polar Molecules with Combined Electrostatic and Pulsed, Nonresonant Laser Fields,” *Phys. Rev. Lett.* **90**, 083001 (2003).
- [43]H. Tanji, S. Minemoto, and H. Sakai, “Three-dimensional molecular orientation with combined electrostatic and elliptically polarized laser fields,” *Phys. Rev. A* **72**, 063401 (2005).
- [44]O. Ghafur, A. Rouzée, A. Gijsbertsen, W. K. Siu, S. Stolte, and M. J. Vrakking, “Impulsive orientation and alignment of quantum-state-selected NO molecules,” *Nature Physics* **5**, 289 (2009).
- [45]J. J. Omiste and R. González-Férez, “Theoretical description of the mixed-field orientation of asymmetric-top molecules: A time-dependent study,” *Phys. Rev. A* **94**, 063408 (2016).
- [46]L. V. Thesing, J. Küpper, and R. González-Férez, “Time-dependent analysis of the mixed-field orientation of molecules without rotational symmetry,” *The Journal of Chemical Physics* **146**, 244304 (2017).
- [47]M. J. Vrakking and S. Stolte, “Coherent control of molecular orientation,” *Chemical Physics Letters* **271**, 209 (1997).
- [48]T. Kanai and H. Sakai, “Numerical simulations of molecular orientation using strong, nonresonant, two-color laser fields,” *The Journal of Chemical Physics* **115**, 5492 (2001).
- [49]T. Kanai, “Ultrafast Tomography of Molecular Orbitals with High-Order Harmonic Generation,” PhD thesis (The University of Tokyo, Mar. 2005).
- [50]K. Oda, M. Hita, S. Minemoto, and H. Sakai, “All-optical molecular orientation,” *Phys. Rev. Lett.* **104**, 213901 (2010).
- [51]小田啓太, “2波長レーザー電場を用いた気体分子の配向制御,” MA thesis (The University of Tokyo, Mar. 2009).

- [52]H. Ohmura and T. Nakanaga, “Quantum control of molecular orientation by two-color laser fields,” *The Journal of Chemical Physics* **120**, 5176 (2004).
- [53]K. Kitano, H. Hasegawa, and Y. Ohshima, “Ultrafast angular momentum orientation by linearly polarized laser fields,” *Physical Review Letters* **103**, 223002 (2009).
- [54]S. De, I. Znakovskaya, D. Ray, F. Anis, N. G. Johnson, I. A. Bocharova, M. Magrakvelidze, B. D. Esry, C. L. Cocks, I. V. Litvinyuk, and M. F. Kling, “Field-Free Orientation of CO Molecules by Femtosecond Two-Color Laser Fields,” *Phys. Rev. Lett.* **103**, 153002 (2009).
- [55]S. Zhang, C. Lu, T. Jia, Z. Wang, and Z. Sun, “Controlling field-free molecular orientation with combined single- and dual-color laser pulses,” *Phys. Rev. A* **83**, 043410 (2011).
- [56]R. Tehini, M. Z. Hoque, O. Faucher, and D. Sugny, *Phys. Rev. A* **85**, 043423 (2012).
- [57]A. Tyagi, A. Maan, D. S. Ahlawat, and V. Prasad, “Effect of aligning pulse train on the orientation and alignment of a molecule in presence of orienting pulse,” *Spectrochimica Acta Part A: Molecular and Biomolecular Spectroscopy* **173**, 13 (2017).
- [58]P. M. Kraus, D. Baykusheva, and H. J. Wörner, “Two-Pulse Field-Free Orientation Reveals Anisotropy of Molecular Shape Resonance,” *Phys. Rev. Lett.* **113**, 023001 (2014).
- [59]P. M. Kraus, D. Baykusheva, and H. J. Wörner, “Two-pulse orientation dynamics and high-harmonic spectroscopy of strongly-oriented molecules,” *Journal of Physics B: Atomic, Molecular and Optical Physics* **47**, 124030 (2014).
- [60]X. Ren, V. Makhija, H. Li, M. F. Kling, and V. Kumarappan, “Alignment-assisted field-free orientation of rotationally cold CO molecules,” *Phys. Rev. A* **90**, 013419 (2014).
- [61]A. T.J. B. Eppink and D. H. Parker, “Velocity map imaging of ions and electrons using electrostatic lenses: application in photoelectron and photofragment ion imaging of molecular oxygen,” *Review of Scientific Instruments* **68**, 3477 (1997).
- [62]D. H. Parker and A. T.J. B. Eppink, “Photoelectron and photofragment velocity map imaging of state-selected molecular oxygen dissociation/ionization dynamics,” *The Journal of Chemical Physics* **107**, 2357 (1997).
- [63]H. Li, W. Li, Y. Feng, H. Pan, and H. Zeng, “Field-free molecular orientation by femtosecond dual-color and single-cycle thz fields,” *Phys. Rev. A* **88**, 013424 (2013).

- [64]H.-P. Dang, S. Wang, W.-S. Zhan, X. Han, and J.-B. Zai, “Field-free molecular orientation by two-color femtosecond laser pulse and time-delayed THz laser pulse,” *Laser Physics* **25**, 075301 (2015).
- [65]Zhi-Yuan Huang and Ding Wang and Zheng Lang and Wen-Kai Li and Rui-Rui Zhao and Yu-Xin Leng, “Field-free molecular orientation enhanced by tuning the intensity ratio of a three-color laser field,” *Chinese Physics B* **26**, 054209 (2017).
- [66]Y.-Y. Liao, “Enhancement and suppression of field-free molecular orientation with two ultrashort pulses,” *The European Physical Journal D* **70**, 142 (2016).
- [67]L. Ma, S. Chai, X.-M. Zhang, J. Yu, and S.-L. Cong, “Molecular orientation controlled by few-cycle phase-jump pulses,” *Laser Physics Letters* **15**, 016002 (2018).
- [68]U. Arya and V. Prasad, “Field-free molecular orientation control due to ramped pulses,” *Phys. Rev. A* **87**, 035402 (2013).
- [69]N. Takemoto and K. Yamanouchi, “Fixing chiral molecules in space by intense two-color phase-locked laser fields,” *Chemical Physics Letters* **451**, 1 (2008).
- [70]K. Lin, I. Tutunnikov, J. Qiang, J. Ma, Q. Song, Q. Ji, W. Zhang, H. Li, F. Sun, X. Gong, H. Li, P. Lu, H. Zeng, Y. Prior, I. S. Averbukh, and J. Wu, “All-optical field-free three-dimensional orientation of asymmetric-top molecules,” *Nature Communications* **9**, 5134 (2018).
- [71]B. J. Sussman, J. G. Underwood, R. Lausten, M. Y. Ivanov, and A. Stolow, “Quantum control via the dynamic Stark effect: Application to switched rotational wave packets and molecular axis alignment,” *Phys. Rev. A* **73**, 053403 (2006).
- [72]A. Goban, “Laser-Field-Free Molecular Orientation,” MA thesis (The University of Tokyo, Mar. 2009).
- [73]A. Goban, S. Minemoto, and H. Sakai, “Laser-Field-Free Molecular Orientation,” *Phys. Rev. Lett.* **101**, 013001 (2008).
- [74]武井大祐, “回転量子状態を選別した分子のレーザー電場のない条件下での3次元配向制御,” MA thesis (The University of Tokyo, Mar. 2014).
- [75]D. Takei, J. H. Mun, S. Minemoto, and H. Sakai, “Laser-field-free three-dimensional molecular orientation,” *Phys. Rev. A* **94**, 013401 (2016).
- [76]Y. Sugawara, A. Goban, S. Minemoto, and H. Sakai, “Laser-field-free molecular orientation with combined electrostatic and rapidly-turned-off laser fields,” *Physical Review A* **77**, 031403 (2008).
- [77]M. Muramatsu, M. Hita, S. Minemoto, and H. Sakai, “Field-free molecular orientation by an intense nonresonant two-color laser field with a slow turn on and rapid turn off,” *Physical Review A* **79**, 011403 (2009).

- [78]菅原悠, “パルス整形技術を用いた分子の配列および配向制御,” MA thesis (The University of Tokyo, Mar. 2007).
- [79]村松雅弘, “整形した 2 波長レーザー電場を用いた分子の配列と配向の制御,” MA thesis (The University of Tokyo, Mar. 2008).
- [80]S. Trippel, T. Mullins, N. L. M. Müller, J. S. Kienitz, R. González-Férez, and J. Küpper, “Two-State Wave Packet for Strong Field-Free Molecular Orientation,” *Phys. Rev. Lett.* **114**, 103003 (2015).
- [81]A. S. Chatterley, E. T. Karamatskos, C. Schouder, L. Christiansen, A. V. Jørgensen, T. Mullins, J. Küpper, and H. Stapelfeldt, “Communication: Switched wave packets with spectrally truncated chirped pulses,” *The Journal of Chemical Physics* **148**, 221105 (2018).
- [82]J. H. Mun, “Laser-field-free and field-free orientation of state-selected molecules,” PhD thesis (The University of Tokyo, Mar. 2015).
- [83]J. H. Mun and H. Sakai, “Improving molecular orientation by optimizing relative delay and intensities of two-color laser pulses,” *Physical Review A* **98**, 013404 (2018).
- [84]V. Devanathan, *Angular Momentum Techniques in Quantum Mechanics*, Fundamental Theories of Physics (Springer Netherlands, 2006).
- [85]R. N. Zare, *Angular momentum : understanding spatial aspects in chemistry and physics* (Wiley, 1988), p. 349.
- [86]幸田清一郎、小谷正博、染田清彦、阿波賀邦夫 編, 量子化学と分子分光學, 第 2 版, 大学院講義物理化学 1 (東京化学同人, 2013).
- [87]A. Edmonds, *Angular Momentum in Quantum Mechanics*, Investigations in physics (Princeton University Press, 1974).
- [88]N. Matsuzawa and D. A. Dixon, “Density functional theory predictions of polarizabilities and first- and second-order hyperpolarizabilities for molecular systems,” *The Journal of Physical Chemistry* **98**, 2545 (1994).
- [89]J. L. Neill, S. T. Shipman, L. Alvarez-Valtierra, A. Lesarri, Z. Kisiel, and B. H. Pate, “Rotational spectroscopy of iodobenzene and iodobenzene–neon with a direct digital 2–8 GHz chirped-pulse Fourier transform microwave spectrometer,” *Journal of Molecular Spectroscopy* **269**, 21 (2011).
- [90]G. Maroulis and M. Menadakis, “Polarizability and hyperpolarizability of COS and NNO,” *Chemical Physics Letters* **494**, 144 (2010).
- [91]P. Bündgen, F. Grein, and A. J. Thakkar, “Dipole and quadrupole moments of small molecules. An ab initio study using perturbatively corrected, multi-reference, configuration interaction wave functions,” *Journal of Molecular Structure: THEOCHEM* **334**, 7 (1995).

- [92]G. Maroulis and C. Pouchan, “Dipole polarizability and hyperpolarizability of FCN, ClCN, BrCN and ICN,” *Chemical Physics* **215**, 67 (1997).
- [93]H. Casimir, *Rotation of a rigid body in quantum mechanics* (J. B. Wolter, 1931).
- [94]P. Atkins and R. Friedman, *Molecular Quantum Mechanics* (OUP Oxford, 2011).
- [95]C. Dion, A. Keller, and O. Atabek, “Orienting molecules using half-cycle pulses,” *The European Physical Journal D - Atomic, Molecular, Optical and Plasma Physics* **14**, 249 (2001).
- [96]R. Loudon, *The Quantum Theory of Light* (OUP Oxford, 2000).
- [97]O. V. Tikhonova and M. S. Molodenskii, “Dynamics of localized wave packets of rotational states of a molecule in a strong laser field,” *Journal of Experimental and Theoretical Physics* **98**, 1087 (2004).
- [98]R. Tehini and D. Sugny, “Field-free molecular orientation by nonresonant and quasi-resonant two-color laser pulses,” *Physical Review A* **77**, 023407 (2008).
- [99]M. Lemeshko, R. V. Krems, J. M. Doyle, and S. Kais, “Manipulation of molecules with electromagnetic fields,” *Molecular Physics* **111**, 1648 (2013).
- [100]K. Yamanouchi, *Quantum Mechanics of Molecular Structures*, SpringerLink : Bücher (Springer Berlin Heidelberg, 2013).
- [101]A. Messiah, *Quantum Mechanics* (John Wiley & Sons Canada, Limited, 1961).
- [102]L. Landau and E. Lifshitz, *Quantum Mechanics: Non-Relativistic Theory*, Course of Theoretical Physics (Elsevier Science, 1981).
- [103]L. Kirkby, *Physics: A Student Companion* (Scion Publishing, 2011).
- [104]K. Igi and H. Kawai, *Ryōshi rikigaku. 001*. (Kōdansha, 1994).
- [105]K. Katou, “Observation of the phase differences of near-threshold high-order harmonics generated in atoms and molecules,” PhD thesis (The University of Tokyo, Sept. 2014).
- [106]Y. Sakemi, “Studies on interactions of molecules with intense femtosecond laser pulses,” PhD thesis (The University of Tokyo, Mar. 2015).
- [107]L. Ma, S. Chai, X.-M. Zhang, J. Yu, and S.-L. Cong, “Molecular orientation controlled by few-cycle phase-jump pulses,” *Laser Physics Letters* **15**, 016002 (2018).
- [108]E. P. Wigner and J. J. Griffin, *Group theory and its application to the quantum mechanics of atomic spectra*, v. 5 (Academic Press, 1959).
- [109]物理のためのリー群とリー代数, SGC ライブラリ (サイエンス社, 2008).
- [110]F. Peter and H. Weyl, “Die Vollständigkeit der primitiven Darstellungen einer geschlossenen kontinuierlichen Gruppe,” *Mathematische Annalen* **97**, 737 (1927).

- [111]U. Fano and G. Racah, *Irreducible tensorial sets*, Pure and applied physics (Academic Press, 1959).
- [112]G. Burns, *Introduction to group theory with applications*, Materials science and technology (Academic Press, 1977).
- [113]J. Normand, *A Lie Group, Rotations in Quantum Mechanics* (North-Holland Publishing Company, 1980).
- [114]P. Bunker and P. Jensen, *Molecular symmetry and spectroscopy*, Monographs - Physical Sciences (NRC Research Press National Research Council of Canada, 1998).
- [115]小野寺嘉孝, 物性物理/物性化学のための群論入門 (裳華房, 1996).
- [116]K. Riley, M. Hobson, and S. Bence, *Mathematical Methods for Physics and Engineering: A Comprehensive Guide* (Cambridge University Press, 2002).
- [117]G. Arfken, H. Weber, and F. Harris, *Mathematical Methods for Physicists: A Comprehensive Guide* (Elsevier Science, 2013).
- [118]T. MacRobert and I. Sneddon, *Spherical Harmonics: An Elementary Treatise on Harmonic Functions, with Applications*, International series of monographs in pure and applied mathematics (Pergamon Press, 1967).
- [119]W. Byerly, *An Elementary Treatise on Fourier's Series: and Spherical, Cylindrical, and Ellipsoidal Harmonics, with Applications to Problems in Mathematical Physics*, Dover Books on Mathematics (Dover Publications, 2014).
- [120]H. Sakai, A. Tarasevitch, J. Danilov, H. Stapelfeldt, R. W. Yip, C. Ellert, E. Constant, and P. B. Corkum, "Optical deflection of molecules," *Phys. Rev. A* **57**, 2794 (1998).
- [121]A. Keller, C. M. Dion, and O. Atabek, "Laser-induced molecular rotational dynamics: A high-frequency Floquet approach," *Phys. Rev. A* **61**, 023409 (2000).
- [122]M. Spanner, S. Patchkovskii, E. Frumker, and P. Corkum, "Mechanisms of Two-Color Laser-Induced Field-Free Molecular Orientation," *Phys. Rev. Lett.* **109**, 113001 (2012).
- [123]K. Sonoda, A. Iwasaki, K. Yamanouchi, and H. Hasegawa, "Field-free molecular orientation of nonadiabatically aligned OCS," *Chemical Physics Letters* **693**, 114 (2018).
- [124]P. Ehrenfest, "P. Ehrenfest, *Ann. Phys.(Berlin)* 51, 327 (1916).," *Ann. Phys.(Berlin)* **51**, 327 (1916).
- [125]M. Born and V. Fock, "Beweis des Adiabatenatzes," *Zeitschrift für Physik* **51**, 165 (1928).
- [126]T. Kato, "On the Adiabatic Theorem of Quantum Mechanics," *Journal of the Physical Society of Japan* **5**, 435 (1950).

- [127]G Nenciu, “On the adiabatic theorem of quantum mechanics,” *Journal of Physics A: Mathematical and General* **13**, L15 (1980).
- [128]B. Bransden and C. Joachain, *Quantum Mechanics* (Prentice Hall, 2000).
- [129]D. Griffiths and D. Schroeter, *Introduction to Quantum Mechanics* (Cambridge University Press, 2018).
- [130]A. C. Aguiar Pinto, M. C. Nemes, J. G. Peixoto de Faria, and M. T. Thomaz, “Comment on the adiabatic condition,” *American Journal of Physics* **68**, 955 (2000).
- [131]D. M. Tong, K. Singh, L. C. Kwek, and C. H. Oh, “Quantitative Conditions Do Not Guarantee the Validity of the Adiabatic Approximation,” *Phys. Rev. Lett.* **95**, 110407 (2005).
- [132]J. Ortigoso, “Quantum adiabatic theorem in light of the Marzlin-Sanders inconsistency,” *Phys. Rev. A* **86**, 032121 (2012).
- [133]D. A. Varshalovich, A. N. Moskalev, and V. K. Khersonskii, *Quantum Theory of Angular Momentum* (WORLD SCIENTIFIC, 1988).
- [134]A. Meurer, C. P. Smith, M. Paprocki, O. Čertík, S. B. Kirpichev, M. Rocklin, A. Kumar, S. Ivanov, J. K. Moore, S. Singh, T. Rathnayake, S. Vig, B. E. Granger, R. P. Muller, F. Bonazzi, H. Gupta, S. Vats, F. Johansson, F. Pedregosa, M. J. Curry, A. R. Terrel, v. Roučka, A. Saboo, I. Fernando, S. Kulal, R. Cimrman, and A. Scopatz, “SymPy: symbolic computing in Python,” *PeerJ Computer Science* **3**, e103 (2017).
- [135]B. Shore, *Manipulating Quantum Structures Using Laser Pulses* (Cambridge University Press, 2011).
- [136]C. W. Gear, *Numerical Initial Value Problems in Ordinary Differential Equations* (Prentice-Hall, Englewood-Cliffs, NJ, 1971).
- [137]桜井捷海, 数値計算による量子力学 (裳華房, 1994).
- [138]W. Press, S. Teukolsky, W. Vetterling, and B. Flannery, *Numerical Recipes 3rd Edition: The Art of Scientific Computing* (Cambridge University Press, 2007).
- [139]S. Širca and M. Horvat, *Computational Methods in Physics: Compendium for Students*, Graduate Texts in Physics (Springer International Publishing, 2018).
- [140]K. Gustafsson, “Control theoretic techniques for stepsize selection in explicit runge-kutta methods,” *ACM Trans. Math. Softw.* **17**, 533 (1991).
- [141]J. Dormand and P. Prince, “A family of embedded Runge-Kutta formulae,” *Journal of Computational and Applied Mathematics* **6**, 19 (1980).
- [142]J. Stoer, R. Bartels, W. Gautschi, R. Bulirsch, and C. Witzgall, *Introduction to Numerical Analysis*, Texts in Applied Mathematics (Springer New York, 2013).

- [143]桜井捷海, コンピュータで学ぶ量子力学基礎編: 数値計算による量子力学 (フロッピーディスク付) (裳華房, 1992).
- [144]J. Geiser, G. Tanoğlu, and N. Gücüyenen, “Higher order operator splitting methods via Zassenhaus product formula: Theory and applications,” *Computers & Mathematics with Applications* **62**, 1994 (2011).
- [145]J. Izaac and J. Wang, *Computational Quantum Mechanics*, Undergraduate Lecture Notes in Physics (Springer International Publishing, 2019).
- [146]H. F. Trotter, “On the Product of Semi-Groups of Operators,” *Proceedings of the American Mathematical Society* **10**, 545 (1959).
- [147]M. Suzuki, “Decomposition formulas of exponential operators and lie exponentials with some applications to quantum mechanics and statistical physics,” *Journal of Mathematical Physics* **26**, 601 (1985).
- [148]M. Suzuki, “Fractal decomposition of exponential operators with applications to many-body theories and Monte Carlo simulations,” *Physics Letters A* **146**, 319 (1990).
- [149]I. Dhand and B. C. Sanders, “Stability of the Trotter–Suzuki decomposition,” *Journal of Physics A: Mathematical and Theoretical* **47**, 265206 (2014).
- [150]N. Wiebe, D. Berry, P. Høyer, and B. C. Sanders, “Higher order decompositions of ordered operator exponentials,” *Journal of Physics A: Mathematical and Theoretical* **43**, 065203 (2010).
- [151]C. S. Bederián and A. D. Dente, “Boosting quantum evolutions using Trotter–Suzuki algorithms on GPUs,” in *Proceedings of HPCLatAm-11, 4th High-Performance Computing Symposium*, Córdoba, Argentina (Citeseer, 2011).
- [152]P. Wittek and F. M. Cucchietti, “A second-order distributed Trotter–Suzuki solver with a hybrid CPU–GPU kernel,” *Computer Physics Communications* **184**, 1165 (2013).
- [153]P. Wittek and L. Calderaro, “Extended Computational Kernels in a Massively Parallel Implementation of the Trotter–Suzuki Approximation,” *Computer Physics Communications* **197** (2015).
- [154]J. Crank and P. Nicolson, “A practical method for numerical evaluation of solutions of partial differential equations of the heat-conduction type,” *Advances in Computational Mathematics* **6**, 207 (1996).
- [155]E. J. Davison, “A High-Order Crank–Nicolson Technique for Solving Differential Equations,” *The Computer Journal* **10**, 195 (1967).
- [156]E. Anderson, Z. Bai, C. Bischof, S. Blackford, J. Demmel, J. Dongarra, J. Du Croz, A. Greenbaum, S. Hammarling, A. McKenney, and D. Sorensen, *LAPACK Users’ Guide*, Third edition (Society for Industrial and Applied Mathematics, Philadelphia, PA, 1999).

- [157]L. S. Blackford, A. Petitet, R. Pozo, K. Remington, R. C. Whaley, J. Demmel, J. Dongarra, I. Duff, S. Hammarling, G. Henry, et al., “An updated set of basic linear algebra subprograms (BLAS),” *ACM Transactions on Mathematical Software* **28**, 135 (2002).
- [158]J. Dongarra, “Basic linear algebra subprograms technical forum standard,” *High Performance Applications and Supercomputing* **16**, 1 (2002).
- [159]塙敏博、中島研吾、大島聡史、伊田明弘、星野哲也、田浦健次朗, データ解析・シミュレーション融合スーパーコンピュータシステム *Reedbush-U* の性能評価, tech. rep. 10 (東京大学情報基盤センター, 東京大学情報基盤センター, 東京大学情報基盤センター, 東京大学情報基盤センター, 東京大学情報基盤センター, 東京大学情報基盤センター, Sept. 2016).
- [160]塙敏博、星野哲也、中島研吾、大島聡史、伊田明弘, *GPU* 搭載スーパーコンピュータ *Reedbush-H* の性能評価, tech. rep. 9 (東京大学情報基盤センター, 東京大学情報基盤センター, 東京大学情報基盤センター, 東京大学情報基盤センター, 東京大学情報基盤センター, Apr. 2017).
- [161]G. Rossum, *Python Reference Manual*, tech. rep. (Amsterdam, The Netherlands, The Netherlands, 1995).
- [162]E. Jones, T. Oliphant, P. Peterson, et al., *SciPy: open source scientific tools for Python*, [Online: <http://www.scipy.org/>], 2001.
- [163]T. E. Oliphant, “Python for Scientific Computing,” *Computing in Science & Engineering* **9**, 10 (2007).
- [164]K. J. Millman and M. Aivazis, “Python for Scientists and Engineers,” *Computing in Science & Engineering* **13**, 9 (2011).
- [165]T. E. Oliphant, *A guide to NumPy*, Vol. 1 (USA: Trelgol Publishing, 2006).
- [166]C. Fuhrer, J. Solem, and O. Verdier, *Scientific Computing with Python 3* (Packt Publishing, 2016).
- [167]K. Ayyadevara, L. Martins, R. Ramos, T. Oliva, and K. Wu, *SciPy Recipes: A cookbook with over 110 proven recipes for performing mathematical and scientific computations* (Packt Publishing, 2017).
- [168]J. Nunez-Iglesias, S. van der Walt, and H. Dashnow, *Elegant SciPy: The Art of Scientific Python*, 1st (O’Reilly Media, Inc., 2017).
- [169]*Intel Math Kernel Library*, <http://software.intel.com/en-us/articles/intel-mkl/>.
- [170]Oleksandr Pavlyk, Denis Nagorny, Andres Guzman Ballen, Anton Malakhov, Hai Liu, Ehsan Toton, Todd A. Anderson, and Sergey Maidanov, “Accelerating Scientific Python with Intel Optimizations,” in *Proceedings of the 16th Python in Science Conference*, edited by Katy Huff, David Lippa, Dillon Niederhut, and M. Pacer (2017), pp. 106–112.

- [171]L. D. Dalcin, R. R. Paz, P. A. Kler, and A. Cosimo, “Parallel Distributed Computing using Python,” *Advances in Water Resources* **34**, 1124 (2011).
- [172]R. Smith, “Performance of MPI Codes Written in Python with NumPy and Mpi4Py,” in *Proceedings of the 6th workshop on python for high-performance and scientific computing, PyHPC ’16* (2016), pp. 45–51.
- [173]W. McKinney, “Data Structures for Statistical Computing in Python,” in *Proceedings of the 9th Python in Science Conference*, edited by S. van der Walt and J. Millman (2010), pp. 51–56.
- [174]J. D. Hunter, “Matplotlib: A 2D Graphics Environment,” *Computing in Science & Engineering* **9**, 90 (2007).
- [175]A. George and J. Liu, *Computer solution of large sparse positive definite systems*, Prentice-Hall series in computational mathematics (Prentice-Hall, 1981).
- [176]J. R. Gilbert, C. Moler, and R. Schreiber, “Sparse Matrices in MATLAB: Design And Implementation,” *SIAM J. Matrix Anal. Appl* **13**, 333 (1992).
- [177]T. A. Davis and Y. Hu, “The University of Florida Sparse Matrix Collection,” *ACM Trans. Math. Softw.* **38**, 1:1 (2011).
- [178]F. Bauer, A. Householder, J. Wilkinson, and C. Reinsch, *Handbook for Automatic Computation: Volume II: Linear Algebra*, Grundlehren der mathematischen Wissenschaften (Springer Berlin Heidelberg, 2012).
- [179]S. J. Rojas G., E. Christensen, and F. Blanco-Silva, *Learning SciPy for Numerical and Scientific Computing - Second Edition*, Community experience distilled (Packt Publishing, 2015).
- [180]I. Duff, A. Erisman, and J. Reid, *Direct Methods for Sparse Matrices*, Numerical Mathematics and Scientific Computation (OUP Oxford, 2017).
- [181]M. Pitzer, M. Kunitski, A. S. Johnson, T. Jahnke, H. Sann, F. Sturm, L. P. H. Schmidt, H. Schmidt-Böcking, R. Dörner, J. Stohner, J. Kiedrowski, M. Reggelin, S. Marquardt, A. Schießer, R. Berger, and M. S. Schöffler, “Direct Determination of Absolute Molecular Stereochemistry in Gas Phase by Coulomb Explosion Imaging,” *Science* **341**, 1096 (2013).
- [182]U. Even, J. Jortner, D. Noy, N. Lavie, and C. Cossart-Magos, “Cooling of large molecules below 1 K and He clusters formation,” *The Journal of Chemical Physics* **112**, 8068 (2000).
- [183]星野哲朗, “分子配向制御のための分子偏向器の開発,” MA thesis (The University of Tokyo, Mar. 2011).
- [184]A Amirav, U Even, and J Jortner, “Cooling of large and heavy molecules in seeded supersonic beams,” *Chemical Physics* **51**, 31 (1980).

- [185]D. L. Snavely, S. D. Colson, and K. B. Wiberg, "Rotational cooling in a supersonic expansion of ammonia," *The Journal of Chemical Physics* **74**, 6975 (1981).
- [186]M. P. Sinha, A. Schultz, and R. N. Zare, "Internal state distribution of alkali dimers in supersonic nozzle beams," *The Journal of Chemical Physics* **58**, 549 (1973).
- [187]D. H. Levy, L. Wharton, and R. E. Smalley, in *Chemical and Biochemical Applications of Lasers*, edited by C. B. MOORE (Academic Press, 1977), pp. 1–41.
- [188]D. H. Levy, "The spectroscopy of very cold gases," *Science*, 263 (1981).
- [189]W. C. Wiley and I. H. McLaren, "Time-of-Flight Mass Spectrometer with Improved Resolution," *Review of Scientific Instruments* **26**, 1150 (1955).
- [190]C. R. Gebhardt, T. P. Rakitzis, P. C. Samartzis, V. Ladopoulos, and T. N. Kitsopoulos, "Slice imaging: A new approach to ion imaging and velocity mapping," *Review of Scientific Instruments* **72**, 3848 (2001).
- [191]D. Townsend, M. P. Minitti, and A. G. Suits, "Direct current slice imaging," *Review of Scientific Instruments* **74**, 2530 (2003).
- [192]G. Wu, W. Zhang, H. Pan, Q. Shuai, B. Jiang, D. Dai, and X. Yang, "A new crossed molecular beam apparatus using time-sliced ion velocity imaging technique," *Review of Scientific Instruments* **79**, 094104 (2008).
- [193]B. J. Whitaker, *Imaging in Molecular Dynamics: Technology and Applications* (Cambridge university press, 2003).
- [194]B. Mamyrin, "Laser assisted reflectron time-of-flight mass spectrometry," *International Journal of Mass Spectrometry and Ion Processes* **131**, 1 (1994).
- [195]D. Ioanoviciu, in *Time-of-flight mass spectrometry and its applications*, edited by E. Schlag (Elsevier, Amsterdam, 1994), pp. 43–65.
- [196]D. Ioanoviciu, "Ion-Optical solutions in time-of-flight mass spectrometry," *Rapid Communications in Mass Spectrometry* **9**, 985.
- [197]L. J. Frasinski, K. Codling, and P. A. Hatherly, "Covariance Mapping: A Correlation Method Applied to Multiphoton Multiple Ionization," *Science* **246**, 1029 (1989).
- [198]K Codling and L. J. Frasinski, "Dissociative ionization of small molecules in intense laser fields," *Journal of Physics B: Atomic, Molecular and Optical Physics* **26**, 783 (1993).
- [199]I. Noda and Y. Ozaki, *Two-Dimensional Correlation Spectroscopy: Applications in Vibrational and Optical Spectroscopy* (Wiley, 2005).
- [200]W. Gordy and R. Cook, *Microwave molecular spectra*, Techniques of chemistry (Wiley, 1984).

- [201]A. Rouzée, A. Gijsbertsen, O. Ghafur, O. M. Shir, T. Bäck, S. Stolte, and M. J. J. Vrakking, “Optimization of laser field-free orientation of a state-selected NO molecular sample,” *New Journal of Physics* **11**, 105040 (2009).
- [202]J. Küpper, F. Filsinger, and G. Meijer, “Manipulating the motion of large neutral molecules,” *Faraday Discuss.* **142**, 155 (2009).
- [203]L. Holmegaard, J. H. Nielsen, I. Nevo, H. Stapelfeldt, F. Filsinger, J. Küpper, and G. Meijer, “Laser-Induced Alignment and Orientation of Quantum-State-Selected Large Molecules,” *Phys. Rev. Lett.* **102**, 023001 (2009).
- [204]J. H. Nielsen, “Laser-Induced Alignment and Orientation of Quantum-State Selected Molecules and Molecules in Liquid Helium Droplets,” PhD thesis (Aarhus University, Feb. 2012).
- [205]F. Filsinger, J. Küpper, G. Meijer, L. Holmegaard, J. H. Nielsen, I. Nevo, J. L. Hansen, and H. Stapelfeldt, “Quantum-state selection, alignment, and orientation of large molecules using static electric and laser fields,” *The Journal of Chemical Physics* **131**, 064309 (2009).
- [206]Y.-P. Chang, F. Filsinger, B. G. Sartakov, and J. Küpper, “CMIstark: Python package for the Stark-effect calculation and symmetry classification of linear, symmetric and asymmetric top wavefunctions in dc electric fields,” *Computer Physics Communications* **185**, 339 (2014).
- [207]Y.-P. Chang, D. A. Horke, S. Trippel, and J. Küpper, “Spatially-controlled complex molecules and their applications,” *International Reviews in Physical Chemistry* **34**, 557 (2015).
- [208]L. He, J. Bulthuis, S. Luo, J. Wang, C. Lu, S. Stolte, D. Ding, and W. G. Roeterdink, “Laser induced alignment of state-selected CH₃I,” *Phys. Chem. Chem. Phys.* **17**, 24121 (2015).
- [209]H. L. Bethlem, M. R. Tarbutt, J. Kupper, D. Carty, K. Wohlfart, E. A. Hinds, and G. Meijer, “Alternating gradient focusing and deceleration of polar molecules,” *Journal of Physics B : Atomic, Molecular and Optical Physics.* **39**, R263 (2006).
- [210]I. Nevo, L. Holmegaard, J. H. Nielsen, J. L. Hansen, H. Stapelfeldt, F. Filsinger, G. Meijer, and J. Küpper, “Laser-induced 3D alignment and orientation of quantum state-selected molecules,” *Physical Chemistry Chemical Physics* **11**, 9912 (2009).
- [211]N. Ramsey and O. U. Press, *Molecular Beams*, International series of monographs on physics (OUP Oxford, 1956).
- [212]P. J. de Groot, “Vibration in phase-shifting interferometry,” *J. Opt. Soc. Am. A* **12**, 354 (1995).
- [213]L. L. Deck, “Suppressing phase errors from vibration in phase-shifting interferometry,” *Appl. Opt.* **48**, 3948 (2009).

- [214]G. W. Li, S. J. Huang, H. S. Wu, S. Fang, D. S. Hong, T. Mohamed, and D. J. Han, “A Michelson Interferometer for Relative Phase Locking of Optical Beams,” *Journal of the Physical Society of Japan* **77**, 024301 (2008).
- [215]H. Mashiko, S. Gilbertson, C. Li, S. D. Khan, M. M. Shakya, E. Moon, and Z. Chang, “Double Optical Gating of High-Order Harmonic Generation with Carrier-Envelope Phase Stabilized Lasers,” *Phys. Rev. Lett.* **100**, 103906 (2008).
- [216]M. Chini, H. Mashiko, H. Wang, S. Chen, C. Yun, S. Scott, S. Gilbertson, and Z. Chang, “Delay control in attosecond pump-probe experiments,” *Opt. Express* **17**, 21459 (2009).
- [217]N. P. Barnes and I. A. Crabbe, “Coherence length of a Q-switched Nd:YAG laser,” *Journal of Applied Physics* **46**, 4093 (1975).
- [218]Q. Chao-Chao, J. Guang-Rui, Z. Xian-Zhou, L. Yu-Fang, L. Jin-You, and Z. Bing, “Field-free molecular orientation induced by combined femtosecond single- and dual-color laser pulses: The role of delay time and quantum interference,” *Chinese Physics B* **23**, 013302 (2014).
- [219]T. Seideman and E. Hamilton, in , Vol. 52, edited by P. Berman and C. Lin, *Advances in Atomic, Molecular, and Optical Physics* (Academic Press, 2005), pp. 289 –329.
- [220]A. S. Chatterley, B. Shepperson, and H. Stapelfeldt, “Three-Dimensional Molecular Alignment Inside Helium Nanodroplets,” *Phys. Rev. Lett.* **119**, 073202 (2017).
- [221]J. L. Hansen, L. Holmegaard, L. Kalhøj, S. L. Kragh, H. Stapelfeldt, F. Filsinger, G. Meijer, J. Küpper, D. Dimitrovski, M. Abu-samha, C. P. J. Martiny, and L. B. Madsen, “Ionization of one- and three-dimensionally-oriented asymmetric-top molecules by intense circularly polarized femtosecond laser pulses,” *Phys. Rev. A* **83**, 023406 (2011).
- [222]J. J. Omiste, M. Gärttner, P. Schmelcher, R. González-Férez, L. Holmegaard, J. H. Nielsen, H. Stapelfeldt, and J. Küpper, “Theoretical description of adiabatic laser alignment and mixed-field orientation: the need for a non-adiabatic model,” *Physical Chemistry Chemical Physics* **13**, 18815 (2011).
- [223]X. Ren, V. Makhija, and V. Kumarappan, “Multipulse Three-Dimensional Alignment of Asymmetric Top Molecules,” *Phys. Rev. Lett.* **112**, 173602 (2014).
- [224]V. Makhija, X. Ren, and V. Kumarappan, “Metric for three-dimensional alignment of molecules,” *Phys. Rev. A* **85**, 033425 (2012).
- [225]G. Graner, E. Hirota, T. Iijima, K. Kuchitsu, D. A. Ramsay, J. Vogt, and N. Vogt, *C₆H₅I, Iodobenzene: Datasheet from Landolt-Börnstein - Group II Molecules and Radicals · Volume 25D: “Molecules Containing Five or More Carbon Atoms” in Springer Materials*, edited by K. Kuchitsu, Copyright 2003 Springer-Verlag Berlin Heidelberg.

- [226]O. Dorosh, E. Białkowska-Jaworska, Z. Kisiel, and L. Pszczółkowski, “New measurements and global analysis of rotational spectra of Cl-, Br-, and I-benzene: Spectroscopic constants and electric dipole moments,” *Journal of Molecular Spectroscopy* **246**, 228 (2007).
- [227]L. Marchildon, *Quantum Mechanics: From Basic Principles to Numerical Methods and Applications*, Advanced Texts in Physics (Springer Berlin Heidelberg, 2013).
- [228]A. Yariv, *Quantum electronics* (Wiley, 1989), p. 676.
- [229]Z. Wang, Z. Zhang, Z. Xu, and Q. Lin, “Space-time profiles of an ultrashort pulsed Gaussian beam,” *IEEE Journal of Quantum Electronics* **33**, 566 (1997).
- [230]D. Cheng, *Field and wave electromagnetics*, The Addison-Wesley series in electrical engineering (Addison-Wesley Publishing Company, 1989).
- [231]J. D. Cox and F. J. G. De Abajo, “Electrically tunable nonlinear plasmonics in graphene nanoislands,” *Nature Communications* **5**, 5725 (2014).

